The Role of PDE2A as a regulator of the cAMP-to-cGMP cross-talk in T cell responses after myocardial infarction

Doctoral thesis

University of Hamburg
Faculty of Mathematics, Informatics and Natural Sciences
Department of Chemistry

Submitted by
Marie Bielenberg

Hamburg, July 2026

1. Reviewer: Prof. Dr. Viacheslav O. Nikolaev
2. Reviewer: Prof. Dr. Elke Oetjen

Disputation Committee Members:
Prof. Dr. Chris Meier
Prof. Dr. Viacheslav Nikolaev
Prof. Dr. Christian Lohr

Date of disputation: 09.10.2026

Die vorliegende Arbeit “The Role of PDE2A as a regulator of the cAMP-to-cGMP cross-talk in T-cell responses after myocardial infarction” wurde am Institut für Experimentelle Herz-Kreislaufforschung des Universitätsklinikums Hamburg-Eppendorf im Zeitraum vom 01.01.2023 – 31.05.2026 angefertigt.

List of publications

Bielenberg M, Kurelic R, Frantz S, Nikolaev VO. A mini-review: phosphodiesterases in charge to balance intracellular cAMP during T-cell activation. Front Immunol. 2024 Mar 8;15:1365484. doi: 10.3389/fimmu.2024.1365484. PMID: 38524120; PMCID: PMC10957532.

Kurelić R, **Bielenberg M**, Nikolaev VO. Monitoring Dynamic of cAMP Signaling in Primary Murine CD4+ T Cells via Live-Cell Imaging. Methods Mol Biol. 2025;2904:115-124. doi: 10.1007/978-1-0716-4414-0_8. PMID: 40220229.

Siegel J, Beer D, Janjatovic S, Auer A, Zipp L.-S, Kozuch E, Krammer T, **Bielenberg M**, Saliba A.-E, Cochain C, Störk S, Heuschmann P, Morbach C, Beyersdorf N, Nahrendorf M, Nikolaev VO, Hofmann U, Frantz S, Wardemann H, Heinrichs M, Heinze KG, Streckfuss-Bömeke K, Ashour D, Ramos GC. Dissecting antibody responses to cardiac receptors in patients with myocardial infarction. medRxiv, 2025.11.03.25339371.

Contents

Contents **1**

List of Figures **5**

List of Tables **7**

List of Abbreviations **8**

1 Zusammenfassung **12**

2 Abstract **14**

3 Introduction **16**

3.1 Cardiovascular diseases 16

3.1.1 Heart failure 16

3.1.2 Myocardial infarction 17

3.2 Immune system 18

3.2.1 T cells 19

3.2.2 T cells after Myocardial Infarction 21

3.3 cAMP signaling in T cells 23

3.3.1 cAMP regulates T cell function 24

3.3.2 G protein-coupled receptors in T cells 25

3.3.2.1 Adrenergic receptors 26

3.3.2.2 Adenosine receptors 26

3.3.3 Phosphodiesterases in T cells 26

3.3.3.1 PDE1 27

3.3.3.2 PDE2A 27

3.3.3.3 PDE3B 27

3.3.3.4 PDE4 28

3.3.3.5 PDE7 28

3.3.3.6 PDE8 29

3.4 Detection of cAMP via Förster Resonance Energy transfer (FRET) live-cell imaging 29

4 Aim of this work **33**

4.1.1 Visualization of cAMP signaling and the regulation of intracellular cAMP mediated by PDE in T cell responses after MI 33
4.1.2 Elucidating the role of PDE2A as a regulator of the cAMP-to-cGMP cross-talk in T cell responses after MI 33

5 Material and Methods 34

5.1 Material 34
5.1.1 Animals 34
5.1.2 DNA oligonucleotides 34
5.1.3 Antibodies 34
5.1.4 Chemicals 35
5.1.5 Cell culture 37
5.1.6 Kits 38
5.1.7 Consumables 39
5.1.8 Devices and instruments 40
5.1.9 Software 42
5.1.10 Buffers 42
5.1.10.1 Buffers used for histological analysis 42
5.1.10.2 Buffers used for Cell culture methods 43
5.1.10.3 Buffers used for microscopical methods 44
5.1.10.4 Buffers used for protein biochemistry methods 44

5.2 Methods 46
5.2.1 *In vivo* experiments 46
5.2.1.1 Animals 46
5.2.1.2 cAMPFIRE-M biosensor mice 46
5.2.1.3 Generation of a PDE2A conditional Knock-Out (cKO) 46
5.2.1.4 LAD Ligation 46
5.2.1.5 Echocardiography 47
5.2.1.6 Tissue collection 47
5.2.2 Nucleotide methods 47
5.2.2.1 DNA Extraction 47
5.2.2.2 Polymerase Chain Reaction (PCR) 47
5.2.2.3 RNA Isolation 48
5.2.2.4 cDNA synthesis 49

5.2.2.5 qRT-PCR 50
5.2.3 Histological analysis 51
5.2.3.1 Tissue preparation for histological analysis 51
5.2.3.2 Immunohistochemistry of CD4 and Foxp3 positive cells 51
5.2.3.3 Interstitial fibrosis 51
5.2.3.4 Wheat germ agglutinin staining 52
5.2.3.5 Quantification of cardiomyocyte cross-sectional area 53
5.2.4 Cell Culture 54
5.2.4.1 Isolation of CD4+ cells 54
5.2.4.2 Isolation of primary cardiomyocytes 55
5.2.5 Microscopical methods 55
5.2.5.1 Förster Resonance Energy Transfer (FRET) Live-cell imaging 55
5.2.6 Protein biochemistry methods 56
5.2.6.1 Sample preparation for immunoblotting 56
5.2.6.2 Sodium dodecyl sulfate polyacrylamide electrophoresis (SDS-PAGE) 56
5.2.6.3 Immunoblotting and immunodetection 57
5.2.6.4 IFN-γ ELISA 58
5.2.7 Statistics 58
6 Results 59
6.1 Visualization of cAMP signaling and the regulation of intracellular cAMP mediated by PDE in T cell responses after MI 59
6.1.1 ß-adrenergic receptor (ß-AR) signaling 59
6.1.2 $A_{2A}R$ signaling 63
6.1.3 Phosphodiesterases are in charge of balance intracellular cAMP 65
6.1.3.1 PDE2 in T cells after MI 66
6.1.3.2 PDE3 in T cells after MI 68
6.1.3.3 PDE4 in T cells after MI 69
6.1.3.4 PDE8 in T cells after MI 71
6.1.4 Summary 73
6.2 The role of PDE2A as a regulator of the cAMP-to-cGMP cross-talk in T cell responses after MI 74
6.2.1 Myocardial infarction mouse model 74

6.2.2 Cardiac hypertrophy 78
6.2.3 Fibrosis 80
6.2.4 T cell infiltration into the infarcted myocardium....81
6.2.5 medLN tissue....83
6.2.6 Cytokine release....85
6.2.7 PDE expression in T cells....86
6.2.8 Summary 91
7 Discussion....92
7.1 β-AR desensitize in local T cells early after MI 92
7.2 PDE4 and PDE8 are differentially active during disease development 94
7.3 Elucidating the role of PDE2A as a regulator of the cAMP-to-cGMP cross-talk in T cell responses post MI 96
8 Summary and conclusion 100
9 References....101
10 Appendix....115
11 Acknowledgments....120
12 Affidavit....122

List of Figures

Figure 1: Immune cells infiltrate the myocardium after myocardial infarction. 18
Figure 2: Differentiation of different T cell subsets. 21
Figure 3: Treg mediate the cardiac repair via immune-suppression, cardio protection, the regulation of the systemic response and promoting the scar formation. 23
Figure 4: Principle of Förster Resonance Energy Transfer (FRET). 30
Figure 5: FRET measurements with cAMPFIRE-M biosensor. 32
Figure 6: Automatic analysis of fibrotic area in heart cross-sectional areas. 52
Figure 7: Determination of CM cross-sectional area in heart sections. 54
Figure 8: Verification of the Myocardial Infarction model of cAMPFIRE-M biosensor mice at day 3 (d3), day 7 (d7) and 8 weeks (8w) post MI. 59
Figure 9: Stimulation of ß-AR in non-activated T cells after MI. 61
Figure 10: ß-AR stimulation in *in vitro* activated CD4+ T cells after MI. 62
Figure 11: Real-time measurements of FRET responses in cardiomyocytes after MI upon isoproterenol (ISO) treatment. 63
Figure 12: $A_{2A}R$ stimulation in non-activated and *in vitro* activated T cells after MI. ..65
Figure 13: FRET measurements in CD4+ T cells expressing cAMPFIRE-M upon PDE2A inhibition. 67
Figure 14: PDE3 inhibition during FRET live-cell measurements in CD4+ T cells. 69
Figure 15: PDE4 inhibition in CD4+ T cells expressing cAMPFIRE-M biosensor. 70
Figure 16: MI affects PDE8 response in T cells at the early stage of T cell infiltration. 72
Figure 17: Infarct size, LV mass and lung weight in Ctrl and PDE2A cKO mice 8 weeks post MI. 75
Figure 18: Cardiac function of PDE2A cKO and Ctrl mice. 77
Figure 19: Determination of left ventricular anterior and posterior wall thickness (LVAW/LVPW) in PDE2A cKO and Ctrl mice. 78
Figure 20: Histological analysis of the impact of the PDE2A dependent loss on hypertrophy development after MI. 79
Figure 21: Interstitial fibrosis in cross-sections of PDE2A cKO and Ctrl mice hearts 8 weeks post MI. 80

Figure 22: CD4+ T cell infiltration into the myocardium of Ctrl and PDE2A cKO mice on day 3 and day 7 post MI. 82
Figure 23: pPKA substrates and Tyrosine Hydroxylase (TH) expression in mediastinal lymph nodes (medLN) from Ctrl and PDE2A cKO mice on day 3 post MI/Sham surgery. 84
Figure 24: PDE expression in mediastinal lymph node (medLN) tissue from Ctrl and PDE2A cKO mice on day 3 post MI/Sham surgery. 85
Figure 25: IFN-γ secretion T cells isolated from PDE2A cKO and Ctrl mice on day 7 post MI. 86
Figure 26: PDE3B, PDE4B/D expression in Ctrl and PDE2A cKO CD4+ T cells on d3 post MI/Sham surgery. 87
Figure 27: PDE3 and PDE4 expression in T cells on day 7 post MI. 88
Figure 28: PDE2A, PDE3 and PDE4 expression 8 weeks post MI. 90
Figure 29: Hazard Pictograms according to GHS. 119

List of Tables

Table 1: Mouse lines. 34
Table 2: DNA Oligonucleotides for PCR. 34
Table 3: Primary antibodies. 35
Table 4: Secondary antibodies. 35
Table 5: Chemicals. 35
Table 6: Cell Culture reagents. 37
Table 7: Kits. 38
Table 8: Consumables. 39
Table 9: Devices and instruments. 40
Table 10: Software. 42
Table 11: Buffers used for histological analysis. 42
Table 12: Buffers used for CD4+ T cell isolation and culture 43
Table 13: Buffers used for cardiomyocyte isolation. 43
Table 14: Buffers used for FRET live-cell measurements. 44
Table 15: Buffers used for sample preparation 45
Table 16: Buffers used for SDS-PAGE and immunoblotting 45
Table 17: Master Mix for Genotyping. 48
Table 18: PCR program for PDE2A and Cre genotyping. 48
Table 19: Reaction mix for cDNA synthesis. 49
Table 20: Program for cDNA synthesis. 50
Table 21: qRT-PCR mix. 50
Table 22: Program for qRT-PCR. 50
Table 23: Tissue preparation for WGA staining. 52
Table 24: Volume of each compound in Stacking and Separating gel. 57
Table 25: Chemicals categorized to GHS. 115

List of Abbreviations

8w	8 weeks post MI/Sham
A	Activated
$A_{2A}R$	Adenosine 2A receptor
AAD	ovalbumin-induced allergic airway disease
AC	Adenylyl cyclase
ACE	Angiotensin-converting enzyme
ADO	Adenosine
ADP	Adenosine diphosphate
AKAP	A-kinase anchoring protein
AMP	Adenosine monophosphate
ANOVA	Analysis of variance
ANP	Atrial natriuretic peptide
AP-1	Activator protein-1
APC	Antigen presenting cell
APS	Ammonium persulfate
ATP	Adenosine triphosphate
BAY	BAY 60-7550
BNP	Brain natriuretic peptide
Bp	Base pair
BSA	Bovine serum albumin
Ca^{2+}	Calcium
cAMP	3', 5' - cyclic adenosine monophosphate
cAMPFIRE	cAMP Fluorescence Imaging Reporters based on Epac
CD	Cluster of differentiation
CFP	Cyan fluorescent protein
cGMP	3', 5' - cyclic guanosine monophosphate
CILO	Cilostamide
cKO	Conditional Knock-Out
CNBD	Cyclic nucleotide binding domain
CNG	Cyclic nucleotide-gated ion channel
CNP	C-natriuretic peptide
CO_2	Carbon dioxide

CREB	cAMP responsive element binding protein
CTLA-4	Cytotoxic T lymphocyte antigen 4
Ctrl	Control
CVD	Cardiovascular disease
d3	Three days post MI/Sham
d3/d7	day 3/day 7 post MI
d7	Seven days post MI/Sham
DAMP	Damage-associated molecular pattern
ddH_2O	Double-destilled water
DMEM	Dulbecco's Modified Eagle's Medium
DN	Double negative
DNA	Desribonucleic acid
DP	Double positive
E	Efficiency
EAE	Experimental autoimmune encephalomyelitis
ECM	Extracellular matrix
EF	Ejection Fraction
ELISA	Ezyme-linked immunosorbent assay
EPAC	Exchange protein directly activated by EPAC
FCS	Fetal calf serum
FoxP3	Forkhead transcription factor family
FRET	Förster Resonance energy transfer
FS	Fractional shortening
FSK	Forskolin
FSK	Forskolin
GPCR	G-protein coupled receptor
GRK2	β-adrenergic receptor kinase
h	Hour
HF	Heart failure
HMGB1	high mobility group box-1
IBMX	3-Isobutyl-1-Methylxanthine
ICER	Inducible cAMP early repressor
IFN-γ	Interferon-gamma
IL	Interleukin

IPEX	Immune dysregulation, polyendocrinopathy, enteropathy, with X-linked inheritance
ISO	Isoproterenol
Jak3	Janus kinase 3
K_m	Michaelis Menten constant
KO	Knock-out
LAD	left anterior descending
Lck	lymphocyte-specific cytoplasmic kinase
LN	Lymph nodes
LV	Left ventricle
LVAW	left ventricular anterior wall
LVID	left ventricular internal diameter
LVPW	left ventricular posterior wall
MACS	Magnetic associated cell sorting
Med	mediastinal
MHC	Major histocompatibility complex
MI	Myocardial Infarction
Min	Minute
miRNA	Micro RNA
MMP-3	matrix metalloprotease 3
Ms	mouse
mTurq	mTurquoise
MYHCA	myosin heavy chain α
NA	Non-activated
NECA	5'-Ethylcarboxamidodenosine
NF-kB	Nuclear factor k-light chain enhancer of activated B cells
NFAT	Nuclear factor of activated T cells
Norm	Normalized
NP	Natriuretic peptide
Ns	Not significant
On	Overnight
PAGE	Polyacrylamid gel electrophoresis
PAMP	pathogen-associated molecular patterns
PBS	Phosphate buffered saline

PCR	Polymerase chain reaction
PDE	Phosphodiesterase
PFA	Paraformaldehyde
PKA	Protein kinase A
PRR	pattern recognition receptors
PSR	Picrosirius red
qRT-PCR	Quantitative real-time PCR
RAG	Recombination activating gene
RNA	Ribonucleic acid
ROLI	Rolipram
rpm	Rotations per minute
RT	Room temperature
S	Second
S_0	Ground state
S_1	Excited state
SDS	Sodium dodecyl sulfate
SEM	Standard error of the mean
SPARC	secreted protein, acidic and rich in cysteine
Stat5	signal transducer and activator of transcription 5
TAE buffer	Tris-acetate-EDTA buffer
Tcon	Conventional T cell
TCR	T cell receptor
Td-cpVenus	Tandem dimer- circularly permutated Venus
TH	Tyrosine hydroxylase
T_H	T helper cell
TNF-α	Tumor necrosis factor alpha
Treg	Regulatory T cell
Tris	Tris-(hydroxymethyl)-aminomethan
WGA	Wheat germ agglutinin
WT	Wildtype
YFP	Yellow fluorescent protein
β-AR	Beta-adrenergic receptor

1 Zusammenfassung

Der Myokardinfarkt ist die häufigste Ursache für die Entstehung einer Herzinsuffizienz, die die Mortalitätsrate um das Dreifache erhöht. Kardiale Antigene und Gefahr-Moleküle werden von den absterbenden Kardiomyozyten sekretiert, um Immunzellen aus den mediastinalen Lymphknoten zu rekrutieren. CD4 positive T Zellen infiltrieren das Myokard und kontrollieren die Immunantwort, indem sie mit anderen Immunzellen interagieren, und tragen zur Gewebeerneuerung bei. Jedoch sind die Mechanismen, wie die T Zellantwort reguliert wird, kaum untersucht worden. 3‘5‘-zyklisches Adenosinmonophosphat (cAMP) ist ein ubiquitär exprimierter sekundärer Botenstoff, der T Zellfunktionen wie die Aktivierung oder die Proliferation kontrolliert und in verschiedenen pathophysiologischen Erkrankungen eine Rolle spielt. Deshalb wird in dieser Arbeit angestrebt, den cAMP Signalweg besser zu verstehen und die Rolle von cAMP-abbauenden Phosphodiesterasen in T Zellen nach Myokardinfarkt zu untersuchen.

Dafür wurde FRET-Mikroskopie von primären T Zellen aus Mäusen mit Myokardinfarkt verwendet, um den β-adrenergen Rezeptor Signalweg und die intrazelluläre cAMP-Dynamik zu beobachten. Der cAMPFIRE-M Biosensor ermöglicht eine einzigartige Möglichkeit, den cAMP Signalweg in Echtzeit zu analysieren. β-adrenerge Rezeptoren de-sensibilisieren in T Zellen aus den mediastinalen Lymphknoten in der frühen Phase nach Infarkt auf Grund von der Freisetzung einer hohen Konzentration Katecholamine. Interessanterweise sind T Zellen aus der Milz unverändert. Phosphodiesterasen hydrolysieren cAMP, um die intrazelluläre Balance zu erhalten. Die Inhibition von den am häufigsten vorkommenden Proteinen zeigte, dass PDE4 (8 Wochen nach Infarkt) und PDE8 (3 Tage nach Infarkt), aber nicht PDE2 und PDE3, in die Regulierung von cAMP in T Zellen nach Myokardinfarkt involviert sind. Des Weiteren wurde der Einfluss auf PDE2A in die Entwicklung der Herzinsuffizienz nach Myokardinfarkt mit Hilfe einer Mauslinie untersucht, die kein PDE2A in CD4 positiven T Zellen exprimiert (PDE2A cKO). Die links-ventrikuläre Masse war nach Infarkt sowohl in den Kontrolltieren als auch in den PDE2A-defizienten Mäusen erhöht, wobei das Lungengewicht nur in den PDE2A cKO erhöht war. Echokardiographie Messungen ermöglichten die Überwachung der Herzfunktion über einen Zeitraum von acht Wochen nach Myokardinfarkt. Die Ejektionsfraktion war nach Myokardinfarkt in beiden untersuchten Gruppen reduziert, jedoch zeigte nur die PDE2A cKO Mauslinie einen vergrößerten

links-ventrikulären internen Durchmesser, was auf eine stärkere Herzinsuffizienz hinweist. Histologische Untersuchung der Herzen bestand aus der Größenbestimmung der Kardiomyozyten, ein Marker für Hypertrophie, die Bestimmung der interstitiellen Fibrose und dem immunhistochemischen Nachweis von infiltrierenden T Zellen. Jedoch ergab die histologische Analyse keinen signifikanten Unterschied zwischen den Mäusen mit und ohne PDE2A in T Zellen, der die stärker ausgeprägte Herzinsuffizienz erklärt. Zusammengefasst bietet diese Arbeit erste Erkenntnisse, wie der cAMP Signalweg in die T Zellantwort involviert ist, die an die Umgebung nach Myokardinfarkt adaptieren.

2 Abstract

Myocardial infarction (MI) is the most common cause of heart failure which increases the mortality rate by three-fold. Despite therapeutic strategies like reperfusion therapy, clinical studies emphasis the impact of the inflammatory response post MI on heart failure development. Cardiac antigens like myosin heavy chain α (MYHCA) and danger-molecules such as the high mobility group box-1 (HMGB1) released from dying cardiomyocytes after myocardial infarction (MI) recruit immune cells from mediastinal lymph nodes (medLN). CD4+ T cells infiltrating the myocardium control the immune response by interacting with other immune cells and contribute to tissue repair. However, mechanisms that control the T cell response are poorly understood. 3'5'-cyclic adenosine monophosphate (cAMP) is a ubiquitous second messenger that controls T cell function including T cell activation and proliferation and it is directly linked to different pathophysiological conditions. Therefore, this work aims to understand cAMP signaling and investigate the role of cAMP-hydrolyzing phosphodiesterases in T cells after MI. For this purpose, FRET live-cell imaging of CD4+ T cells from mice after MI was performed to monitor the β-adrenergic receptor signaling and intracellular cAMP dynamics. The cAMP Fluorescence Imaging Reporters based on Epac (cAMPFIRE-M) biosensor provided a unique opportunity to analyze real-time dynamics of the cAMP signaling pathway beyond measuring protein expression. β-AR desensitization occurred in T cells derived from medLN early post MI due to the release of high levels of catecholamines. Interestingly, splenic T cells were unaffected. Intracellular cAMP levels are balanced by phosphodiesterase-mediated degradation. The inhibition of the most abundant phosphodiesterases revealed that PDE4 (8w post MI) and PDE8 (d3 post MI), but not PDE2 and PDE3, are involved in the regulation of cAMP homeostasis in T cells post MI. Additionally, the impact of PDE2A in T cells on the development of heart failure was investigated by a CD4-specific PDE2A cKO mouse model. The left ventricular mass (LV) of the hearts increased due to MI, but only PDE2A cKO mice showed an increased lung weight after MI. In echocardiography measurements, the cardiac function was monitored up to 8 weeks post MI. The ejection fraction (EF) decreased over time due to MI in both groups, whereas the diastolic left ventricular internal diameter increased only in PDE2A cKO mice indicating a more pronounced heart failure. Histological analysis of the hearts further investigated the size of the cardiomyocytes, a marker for hypertrophy,

the content of interstitial fibrosis and the immunohistochemistry staining of infiltrating CD4+ T cells. Taken together, the results revealed no significant alterations due to the loss of PDE2A in T cells. Collectively, this study revealed first insights into how cAMP signaling is involved in T cells that adapt to the post-MI environment.

3 Introduction

3.1 Cardiovascular diseases

Cardiovascular diseases (CVD) are the most common cause of death worldwide with increasing burden since 1990. Over 626 million cases of CVD were detected globally in 2023. Myocardial infarction (MI) has a central position in the CVD-related mortality often leading to heart failure (HF) development (Global Burden of Cardiovascular and Risks 2025).

3.1.1 Heart failure

HF describes the dysfunction of the heart to pump the required amount of blood with oxygen to the peripheral tissue. The risk of developing HF in life is one in five for a 40-year-old man in the western world and increases with lifetime. Risk factors for developing HF encompassing previous diseases like coronary heart disease, diabetes mellitus, hypertension but also smoking, obesity and alcohol abuse (Schwinger 2021). Clinically, Heart failure is a systemic disease manifesting with symptoms like dyspnea, fatigue and peripheral oedema and is classified into three subtypes based on the left ventricular ejection fraction (EF): HF with preserved EF (HFpEF; EF over 50 %), HF with mildly reduced EF (HFmrEF; EF between 40 and 49 %), HF with reduced EF (HFrEF; EF under 40 %) (Ponikowski et al. 2016). At the structural level, the progression towards HF is driven by adverse LV remodeling characterized by cardiomyocyte hypertrophy, myocyte apoptosis and interstitial fibrosis. Compensatory, concentric hypertrophy maintains cardiac output, but transitions to ventricular dilatation, LV stiffness, wall thinning and progressive contractile dysfunction over time. To investigate the underlying mechanisms of HF in experimental settings, murine models are widely employed. However, mice do not spontaneously develop HF and HF must be experimentally induced. Two established methods are left anterior descending (LAD) artery ligation and transverse aortic constriction (TAC). LAD ligation induces an acute MI through a permanent occlusion of the LAD coronary artery (Muthuramu et al. 2014). TAC imposes chronic pressure overload through aortic constriction that results in hypertrophy and progressive HF (Bosch et al. 2021). Among the leading causes of HFrEF, MI occupies a central position as cardiomyocyte death

during the ischemic event triggers adverse ventricular remodeling and subsequent HF progression (Jenca et al. 2021).

3.1.2 Myocardial infarction

MI occurs when a coronary artery becomes occluded by a rupture or an erosion of an atherosclerotic plaque leading to ischemia and necrosis of the myocardial tissue. Despite reperfusion therapy, a significant proportion of patients develop adverse cardiac remodeling and HF, characterized by wall thinning, left ventricular dilatation and a progressive loss of the contractile function. Patients with HF development post MI have a three-fold total mortality risk and four-fold cardiovascular mortality (Jenca et al. 2021). The reduced cardiac output activates the sympathetic nervous system leading to a neurohumoral response. Catecholamines, norepinephrine and epinephrine, are released from the sympathetic nerves and the adrenal medulla, respectively, to compensatory enhance myocardial contractility via β-adrenergic receptor signaling. Nevertheless, chronic activation of the sympathetic nervous system leads to adverse remodeling, hypertrophy and fibrosis (Florea and Cohn 2014). Furthermore, as a stress signal due to the increased myocardial stretch, atrial and brain natriuretic peptides, ANP and BNP, are released from the atria and the ventricles. NPs have antihypertensive effects and counterbalance the volume overload induced by the catecholamines (Volpe, Carnovali, and Mastromarino 2016). Current treatment options targeting the neurohormonal response are beta-blockers, mineralocorticoid receptor agonists and Angiotensin-converting enzyme (ACE) inhibitors, angiotensin receptor blockers and statins. Commonly used beta-blockers for the treatment of HF are Bisoprolol, Carvedilol and Metoprolol, among others, which reduce the heart rate and myocardial contractility (Bristow 2000). These pharmacological approaches reduce mortality but fail to fully prevent the adverse cardiac remodeling and the development of heart failure (Carberry et al. 2024). Thus, more recent clinical trials, such as the CANTOS and COLCOT trial, focus on targeting inflammation after MI. The CANTOS study demonstrated that an IL-1β antibody significantly reduced the cardiovascular events (Ridker et al. 2017). In the COLCOT trial, the anti-inflammatory drug Colchicine led to a significantly lower risk of cardiovascular events in patient with recent MI (Tardif et al. 2019). These studies are based on the observation that dying cardiomyocytes and necrotic tissue trigger a local inflammatory response also referred to as “sterile inflammation”. The acute inflammation is driven by immune cells of the

innate immune system to clear the tissue from damaged cells and debris. (Prabhu and Frangogiannis 2016). Within the first three days post MI, neutrophils rapidly infiltrate the myocardium followed by M_1 macrophages with a pro-inflammatory gene profile and Ly6^{hi} monocytes. Between day 4 and day 14, the inflammatory phase switches to a resolution or reparative phase, characterized by an accumulation of anti-inflammatory M_2 macrophages, Ly6^{lo} monocytes, T helper 1 cells (T_H1) and regulatory T cells (Treg) (Yan et al. 2013). The kinetics of infiltrating immune cells is depicted in **Figure 1**.

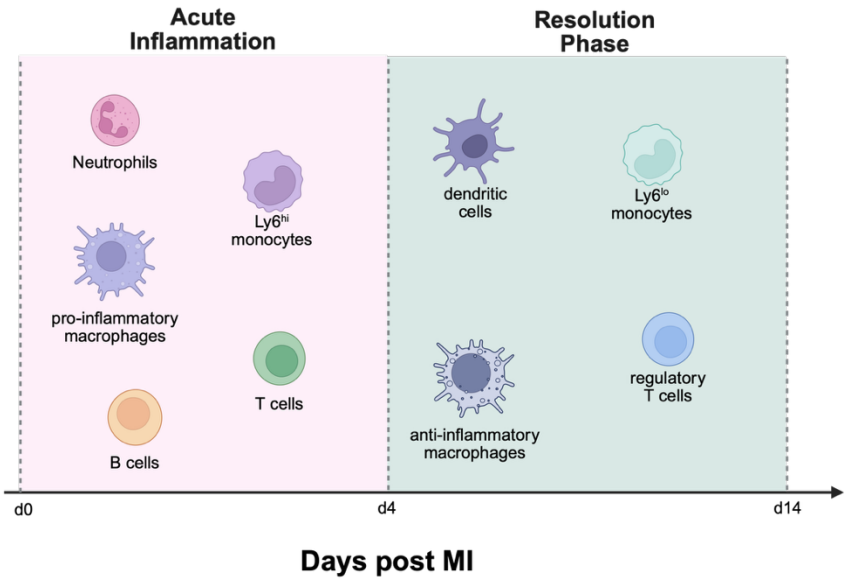


Figure 1: Immune cells infiltrate the myocardium after myocardial infarction. During the first days after myocardial infarction pro-inflammatory cells, like pro-inflammatory macrophages, neutrophils, Ly6^{hi} monocytes, shape the acute inflammatory phase. In the resolution phase, also called reparative phase, anti-inflammatory cells like regulatory T cells, anti-inflammatory macrophages, Ly6^{lo} monocytes accumulate in the heart. This image was created with BioRender.com and is adopted from (Prabhu and Frangogiannis 2016).

3.2 Immune system

The immune system is the primary defense of the body against pathogens like bacteria and viruses and is essential for the elimination of damaged cells. The different immune cell types can be classified into innate and adaptive immune system. Cells of the innate immune system, macrophages, neutrophils and natural killer cells, recognize pathogen-associated molecular patterns (PAMPs) through their germline-encoded pattern recognition receptors (PRRs) and are responsible for a fast response (Chen et

al. 2025). In contrast to the innate immune system, the adaptive immune response is slower, but more specific due to immunological memory. The two major cell types mediating the adaptive immune response are B cells, which produce antigen-specific antibodies, and T cells, which coordinate the responses against pathogens but also maintain the immune homeostasis through life (Chi, Pepper, and Thomas 2024).

3.2.1 T cells

T cells can be divided into cluster of differentiation (CD) 4 T helper cells, CD8 cytotoxic T cells and FoxP3+ regulatory T cells (Treg). Like most immune cells, T cells develop from hematopoietic stem cells which differentiate to lymphoid progenitor cells in the bone marrow. Afterwards, the maturation process from lymphoid progenitor cells to CD4 and CD8 T cells takes place in the thymus. The least mature T cells are called double-negative (DN) thymocytes harboring neither CD4 nor CD8 T cell receptors (TCR). From there, T cell development involves four stages: DN1 (CD44+CD25-), DN2 (CD44+CD25+), DN3 (CD44-CD25+) and finally (CD44-CD25-) (Godfrey et al. 1993). A critical checkpoint in this process is called β-selection during the DN3 stage where the T cell receptor-β (TCR-β) gene is rearranged via recombination activating gene 1/2 (RAG1/RAG2) mediated gene recombination (Yang, Jeremiah Bell, and Bhandoola 2010). A functional TCR-β chain pairs with a pre-T cell-α forming the pre-TCR complex. The production of a TCR-β chain ensures the transition from the DN4 stage to a double-positive stage, characterized by the expression of both CD4 and CD8 T cell receptors. Thymocytes without a functional TCR-β chain undergo apoptosis (Dutta, Zhao, and Love 2021). The subsequent positive selection ensures that only T cells with a functional TCR survive, while negative selection eliminates T cells that react to self-antigens to maintain self-tolerance in the body (Sha et al. 1988). T cells that recognize Major histocompatibility complex (MHC) class II molecules become CD4+ T cells, whereas those recognizing MHC class I become cytotoxic CD8+ T cells. The naïve T cells exit the thymus and migrate to the peripheral lymphoid tissue.

Naïve T cells become activated through direct contact with antigen presenting cells (APCs), like dendritic cells and macrophages, forming the immune synapse. T cell activation requires two signals: Signal one is TCR recognition of an antigen presented on the MHC complex of an APC (Grakoui et al. 1999). However, signal one is not sufficient to induce a full T cell activation. Induction of the TCR in absence of the

costimulatory signal drives T cells towards a state called anergy (Schwartz 1990). Signal two is provided by the binding of CD80/86 on the APC to CD28 on the T cell surface that prevents anergy (Harding et al. 1992). Both signals together activate transcription factors like Nuclear factor k-light chain enhancer of activated B cells (NF-κB), Nuclear factor of activated T cells (NFAT) and Activator protein-1 (AP-1) which mediate for example the interleukin-2 (IL-2) production (Shaw et al. 1988; Jain, Valge-Archer, and Rao 1992; Cross et al. 1989).

Beyond T cell activation, APCs also secrete cytokines which determine the T cell differentiation to a specific T cell subset. The majority of CD4+ T cells are conventional T cells (Tcon). Tcon can be subdivided into T helper cell 1, 2, 17 (T_H1, T_H2 and T_H17) (Zhu, Yamane, and Paul 2010). T cells differentiate into T_H1 cells in the presence of IL-12 and IFN-γ, express the transcription factor T-bet and predominantly secrete IFN-γ for the immune defense (Mullen et al. 2001; Lighvani et al. 2001). Secondly, in response to IL-4, naïve T cells differentiate to T_H2 cells which are involved in anti-parasitic immunity and the development of allergies (Le Gros et al. 1990; Li, Zhang, and Sun 2011). Thirdly, T_H17 cells secrete IL-17A and IL-17F and require the presence of TGF-β and IL-6 (Veldhoen et al. 2006). T_H17 cells recruit neutrophils to defend against bacteria and fungi (Ye et al. 2001; Huang et al. 2004). In the presence of TGF-β and IL-2, naïve conventional T cells differentiate into regulatory T cells (Treg) in the periphery (Chen et al. 2003). Besides these induced Treg, Treg can also occur as thymus-derived natural Treg, natural Treg, after a FoxP3 lineage development during thymic selection. Approximately 5-10 % of the CD4+ T cell population are Treg expressing the lineage-specific transcription factor FoxP3 (Sakaguchi et al. 1995). Treg suppress immune responses by the secretion of anti-inflammatory cytokines, such as IL-10 and TGF-β (Asseman et al. 1999). Mutations in the *FoxP3* gene leading to Treg deficiency or dysfunction resulting in a pathological syndrome characterized by immune dysregulation, polyendocrinopathy, enteropathy, with X-linked inheritance (IPEX) (Wildin et al. 2001).

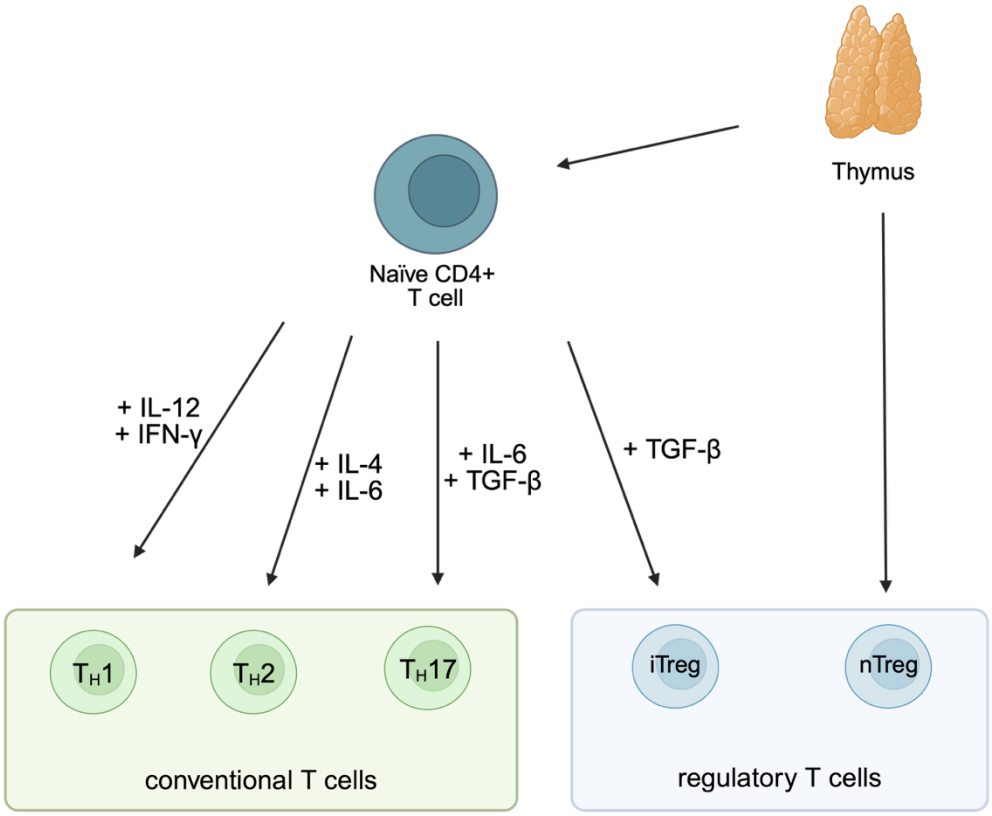


Figure 2: Differentiation of different T cell subsets. Thymus-derived naïve CD4+ T cells differentiate into conventional T cells, T_H1, T_H2 and T_H17 and induced regulatory T cells (iTreg) based on the presence of different cytokines. Natural-occurring regulatory Treg (nTreg) derive from the thymus. Figure was created with Biorender.com and adopted from (Jelley-Gibbs et al. 2008).

3.2.2 T cells after Myocardial Infarction

Cardiac antigens like the myosin heavy chain α (MYHCA) activate CD4+ T cells in the mediastinal lymph nodes (medLN), also called heart-draining lymph nodes, after MI (Delgobo et al. 2023; Rieckmann et al. 2019). Mice without CD4 or MHCII developed severe defects after MI: CD4 KO mice showed an impaired collagen matrix formation, higher numbers of proinflammatory monocytes in the infarcted tissue resulting in an increased mortality rate. Also, OT-II mice which are not able to recognize autoantigens showed similar impaired scar formation and a reduced survival rate indicating that CD4+ T cells are required for a proper scar formation to prevent LV dilation (Hofmann et al. 2012). Nevertheless, chronic T cell activation in the ischemic failing heart promotes adverse cardiac remodeling (Bansal et al. 2017). A temporal analysis of the infiltrating immune cells post MI revealed that T cells infiltrating the heart from the mediastinal lymph nodes are a heterogeneous population with pro-inflammatory T_H1 cells as the predominant subset in the heart, while T_H17 and T_H2 cell population

remained minimal (Yan et al. 2013). Importantly, also regulatory T cells (Treg) accumulate in the infarcted area and drive the transition from a pro-inflammatory to a pro-reparative phase (Weirather et al. 2014). They suppress the immune response by blocking the pro-inflammatory cytokine release of Tcon, the chemokine production and neutrophil infiltration (Weiss, Ramos, and Delgobo 2022). Moreover, T cells interact with macrophages what leads to a switch from pro-inflammatory to a pro-reparative state mediated by IL-10 and TGF-β (Jung et al. 2017; Ikeuchi et al. 2004). A more recent publication by Alshoubaki et al. described how Treg adopt a specific post-MI transcriptome, thereby mediating the monocyte/macrophage function and promoting cardiac repair (Alshoubaki et al. 2024). Treg facilitate proper scar formation in the infarction zone by interacting with fibroblasts. Co-culture of Treg and fibroblasts significantly reduced α-SMA and matrix metalloprotease 3 (MMP-3) expression in fibroblasts (Saxena et al. 2014). Notably, via TGF-β expression of the matricellular protein secreted protein, acidic and rich in cysteine (SPARC) which is required for the extracellular matrix assembly and wound healing (Xia et al. 2020). Furthermore, Tang et al. showed that the Treg expansion reduced cardiomyocyte apoptosis partially via IL-10 secretion but also by cell-cell contact (Tang et al. 2012).

In summary, Increasing FoxP3 frequency by a CD28 super agonistic antibody or Treg transfer improved cardiac function, whereas Treg depletion in mice resulted in a reduced survival rate and more pronounced cardiac defects (Weirather et al. 2014). More recent discovery shed first light on the molecular mechanisms how Treg fulfill their protective function. Cardiac Treg showed an upregulated expression of CD73, the ectoenzyme that converts AMP to adenosine (ADO), on their cell surface after MI and CD73 deficiency impaired their immunosuppressive capacity and cardiac healing (Zhuang et al. 2022). Besides their local response in the infarcted heart, CD4+ T cells also shape the systemic response. IFN-γ secreting Tcon promote splenic myelopoiesis and the generation of proinflammatory monocytes while Treg attenuate this process (Gladow et al. 2024).

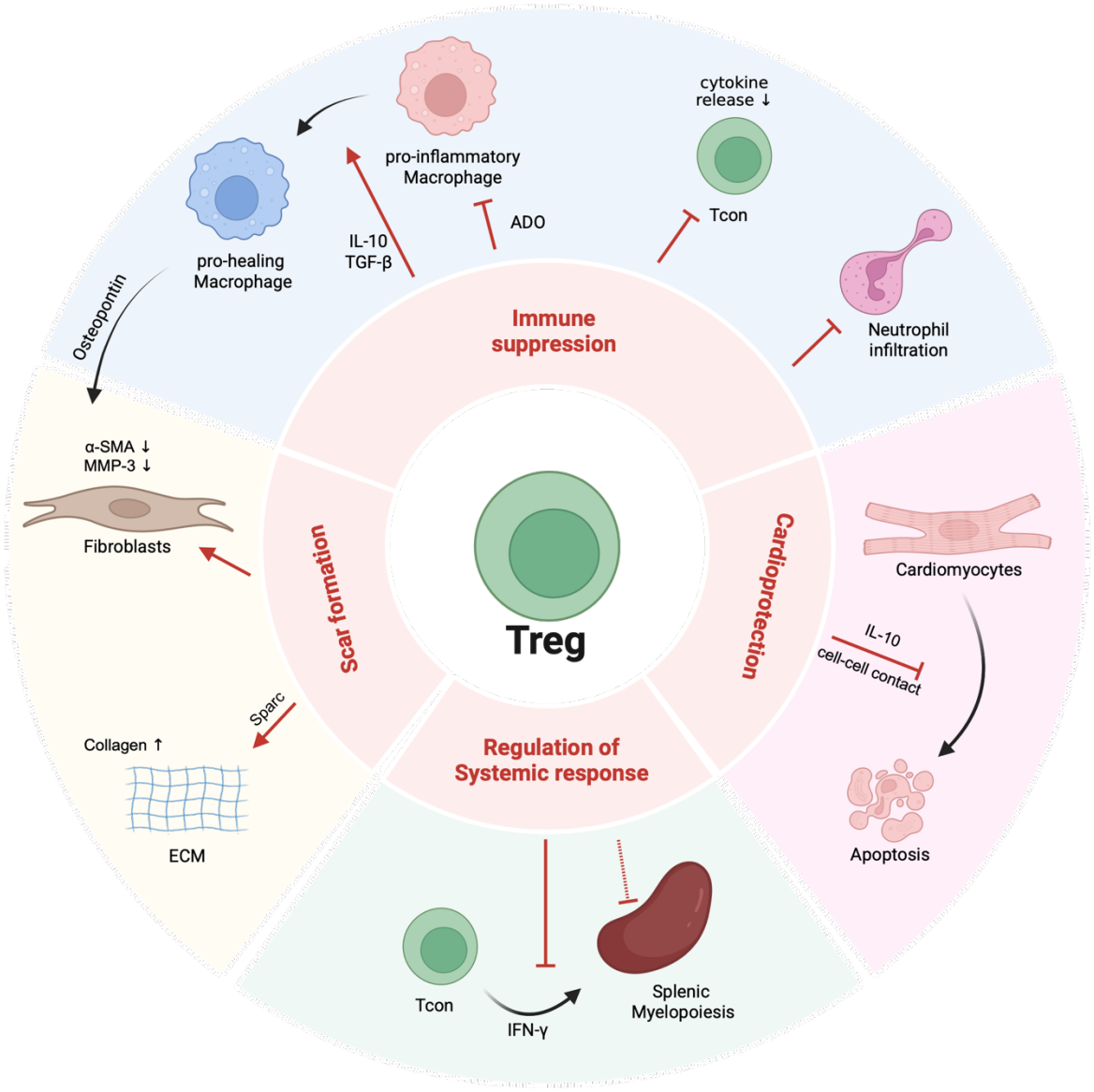


Figure 3: Treg mediate the cardiac repair via immune-suppression, cardio protection, the regulation of the systemic response and promoting the scar formation. To suppress the inflammatory immune response the shift from pro-inflammatory to pro-healing macrophages is induced via IL-10 and TGF-β secretion, the neutrophil infiltration is blocked and the cytokine release from conventional T cells is dampened by Treg. The cell-cell contact and IL-10 secretion protects cardiomyocytes from apoptosis. Treg attenuate the production of pro-inflammatory monocytes in the spleen thereby regulating the systemic response post MI. Lastly, Treg are important for the scar formation by interacting with fibroblasts and the extra cellular matrix (ECM) via Sparc secretion. This image was created with Biorender.com and adopted from (Weiss, Ramos, and Delgobo 2022).

3.3 cAMP signaling in T cells

cAMP was the first second messenger discovered in 1958 which triggered a signaling cascade to mediate cellular processes like transcription factors or metabolic shifts

(Sutherland and Rall 1958). Since then, cAMP signaling has been studied in many different cell types and various diseases, such as CVD. Adenylyl cyclases (AC1-9) catalyze the conversion of adenosine triphosphate (ATP) to 3', 5' - cyclic adenosine monophosphate (cAMP). AC3, AC6 and AC7 have been described in T cells, whereas AC9 is predominantly expressed (Duan et al. 2010; Huang et al. 2009). Rising intracellular cAMP concentration activates protein kinase A (PKA), exchange protein directly activated by cAMP (EPAC) and cyclic nucleotide-gated ion channels (CNG channels). PKA composed of two regulatory and two catalytic subunits releases the catalytic subunits upon cAMP binding which then phosphorylates serine and threonine residues of numerous substrates such as cAMP response element-binding protein (CREB), cAMP responsive element modulator (CREM) and nuclear factor κ-light chain enhancer of activated B cells (NF-κB). EPAC1 and EPAC2 function as guanine nucleotide exchange factors for GTPases (Rap1 and Rap2) which further modulate cellular processes (de Rooij et al. 2000). Importantly, cAMP is specifically regulated in highly compartmentalized areas of the cell. A-kinase anchoring proteins (AKAPs) localize PKA to its targets and allow a specific and fast subcellular signaling cascade. In T cells, 7 different AKAPs are discovered for compartmentalization of cAMP signaling: Ezrin, AKAP79, D-AKAP1, AKAP450, MTG8, MTG16b and AKAP95 (Wehbi and Taskén 2016).

3.3.1 cAMP regulates T cell function

cAMP was initially described in T lymphocytes showing inhibitory but also stimulatory effects on DNA synthesis (Wang, Sheppard, and Foker 1978). Further research shed light into the complex cAMP-mediated regulation of T cell function, involving T cell activation, T cell proliferation and cytokine homeostasis. During T cell activation, TCR stimulation increases local cAMP production and PKA phosphorylation in lipid rafts (Abrahamsen et al. 2004). Phosphorylated PKA activates, among others, C-terminal Src kinase (Csk) which then subsequently inhibits the activity of the lymphocyte-specific cytoplasmic kinase (Lck) resulting in a downregulation of TCR signaling (Arumugham and Baldari 2017; Wehbi and Taskén 2016). Ezrin holds PKA close to the lipid rafts at the cell membrane which is important for a negative feedback loop to prevent excessive T cell activation. Disruption of the AKAP/PKA complex resulted in enhanced TCR signaling suggesting that the compartmentalization of PKA is required for cAMP-mediated regulation (Ruppelt et al. 2007). Additionally, the co-

stimulation with CD28 leads to enhanced PDE4-mediated cAMP degradation in lipid rafts (Tasken and Ruppelt 2006; Abrahamsen et al. 2004). High levels of cAMP increase Cytotoxic T lymphocyte antigen 4 (CTLA-4) expression and thereby inhibit the binding of CD28 (Lorton and Bellinger 2015). Moreover, elevated cAMP levels uncouple the IL-2R complex and inhibit the subsequent activation of signal transducer and activator of transcription 5 (Stat5)/Janus kinase 3 (Jak3) resulting in a reduced T cell proliferation (Rodriguez et al. 2013). Beyond IL-2, also other cytokines like TNF-α, IL-5 and IL-10, are also regulated by cAMP signaling (Jimenez et al. 2001; Heijink et al. 2003; Liopeta et al. 2009). Recently, it has been shown that the generation of IL-17 in T_H17 cells is dependent on cAMP and ß-adrenergic signaling (Lauten et al. 2025). Lastly, cAMP levels differ between T cell subsets. Treg harbor more cAMP than Tcon and it is further induced upon T cell activation (Bopp et al. 2007). Different mechanisms have been discovered that mediate raise of intracellular cAMP in Treg: The Treg-specific transcription factor Foxp3 leads to a reduced expression of PDE3B (Gavin et al. 2007). Additionally, AC9 expression is enhanced by the microRNA miR-142-3p, which is also expressed exclusively in Treg (Huang et al. 2009). When this microRNA is missing, genes related to IFN-γ and IFN-γ levels are elevated (Ma et al. 2019). Increased cAMP is crucial for Treg to fulfill their immunosuppressive function. On the one hand, Treg can transfer cAMP to Tcon directly via gap junctions (Bopp et al. 2007). Additionally, CD39 and CD73 on the Treg cell surface degrade ATP to ADO. ADO binds to the A_{2A} receptors on the cell surface of Tcon and increases intracellular cAMP (Klein and Bopp 2016).

3.3.2 G protein-coupled receptors in T cells

G-protein coupled receptors (GPCR) are a diverse superfamily of cell surface receptors with seven transmembrane domains. Roughly 34 % of the drugs approved by the FDA target GPCRs underlining their therapeutic importance in cardiovascular disease, diabetes and others (Hauser et al. 2017). By binding to its extracellular ligand, such as hormones or neurotransmitters, a conformational shift is induced and the G_α subunit dissociates from the $G_{\beta,\gamma}$ dimer. The activated subunit proteins are divided in four groups: G_s, G_i, G_q and $G_{12/13}$. G_s stimulates while G_i inhibits AC-mediated cAMP synthesis.

3.3.2.1 Adrenergic receptors

Among others, adrenergic receptors are an important member of GPCRs in T cells. The subtypes α– and β-adrenergic receptors (β-AR) exist in five and three isoforms, respectively. Immune cells, including T cells, express predominantly β_2-AR subtype (G_s coupled) and its expression is upregulated during T cell activation (Ramer-Quinn, Baker, and Sanders 1997). β-AR bind catecholamines, norepinephrine and epinephrine, and have been studied in several pathophysiological conditions including cardiovascular diseases. When T cells are exposed to catecholamines, T cell proliferation and IL-2 production upon activation is suppressed, which can be reversed by beta-blockers. Moreover, the suppressive capacity of Treg is enhanced and CTLA-4 expression is upregulated (Guereschi et al. 2013). The inhibition of β-AR by terbutaline increased IL-17 secretion and the proportion of T_H17 cells through PKA signaling but had the opposite effect on IFN-γ secretion (Lauten et al. 2025; Carvajal Gonczi et al. 2017). Catecholamines are mainly produced by sympathetic nervous fibers, but T cells also express the tyrosine hydroxylase (TH), the enzyme for catecholamine synthesis. High levels of catecholamines released from T cells downregulate the Treg suppressive function in an autocrine loop (Cosentino et al. 2007).

3.3.2.2 Adenosine receptors

Another GPCR family member is the adenosine receptor that can be divided into four subtypes: A_1, A_{2A}, A_{2B} and A_3 (Fredholm et al. 2001). The A_{2A} receptor ($A_{2A}R$) is predominantly expressed in T cells (Deaglio et al. 2007). $A_{2A}R$ stimulation by its ligand ADO decreased T cell proliferation, cytokine secretion like IL-2, IL-4 and IFN-γ and inhibited T_H1 and T_H2 cell development (Huang et al. 1997; Csoka et al. 2008). Mice lacking A_{2A} had a more severe disease progression and enhanced inflammation during experimental autoimmune encephalomyelitis (EAE) further underlining the A_{2A}-mediated immunosuppressive effects (Ingwersen et al. 2016).

3.3.3 Phosphodiesterases in T cells

Phosphodiesterases are a superfamily of 11 enzyme families (PDE1-11) that are crucial regulators of the intracellular cyclic nucleotide homeostasis. Over 100 different isoforms have been discovered in different cell types (Conti and Beavo 2007; Kelly et al. 2025). PDE classes are defined by their C-terminal catalytic domain, whereas the

N-terminus differs between the different isoforms. Characteristic differences are also based on their affinity to cyclic nucleotides. PDE4, 7 and 8 are cAMP-specific, PDE5, 6 and 9 cGMP-specific while PDE1, 2, 3, 10 and 11 harbor the capacity to degrade both cyclic nucleotides.

3.3.3.1 PDE1

The PDE1 family consists of three isoforms: PDE1A, PDE1B and PDE1C. All isoforms are activated through calcium and calmodulin (CaM) binding but exhibit different substrate preferences. PDE1A and PDE1B hydrolyze cGMP more efficiently than cAMP, PDE1C has a dual-substrate specificity for both cyclic nucleotides (Goraya and Cooper 2005). PDE1 was not detected in resting human T lymphocytes, but the expression could be induced upon T cell activation (Kanda and Watanabe 2001).

3.3.3.2 PDE2A

PDE2A is a dual-substrate PDE hydrolyzing cAMP (K_m 30µM) and cGMP (K_m 10µM) (Martins, Mumby, and Beavo 1982). PDE2A exists in three splice variants with different N-terminus and distinct subcellular localizations. PDE2A1 is cytosolic, while PDE2A2 and PDE2A3 are membrane bound. PDE2A is also called the cGMP-activated cAMP-hydrolyzing PDE because of its unique function. Activated by cGMP binding to its GAF-B domain PDE2A the rate of cAMP hydrolysis is increased (Bender and Beavo 2006). In 1996, PDE2A expression in T cells was described for the first time (Michie et al. 1996). 25 years later, research revealed T cell subpopulation differences in the expression of PDE2A (Kurelic et al. 2021). Upon TCR stimulation PDE2A expression is selectively upregulated in Tcon but not in Treg suggesting a switch in the cyclic nucleotide crosstalk from a PDE3B-dependent positive to a PDE2A-dependent negative cGMP-to-cAMP crosstalk. Moreover, PDE2A upregulation has also been confirmed *in vivo* in T cells isolated from the periphery lymphatic organs of EAE mice in acute stage (Kurelic et al. 2021).

3.3.3.3 PDE3B

Another cGMP regulated dual-substrate PDE is PDE3 with its isoforms PDE3A and PDE3B. T lymphocytes express PDE3B which mediates the positive cGMP-to-cAMP cross-talk. PDE3 harbors a higher hydrolysis rate for cAMP than for cGMP causing the

inhibition of cAMP hydrolysis when cGMP is bound (Bender and Beavo 2006). Importantly, Treg express significantly lower levels of PDE3B due to the subpopulation-specific transcription factor *Foxp3* (Gavin et al. 2007). The expression of *Foxp3* leads to transcriptional repression of PDE3B. Moreover, the predominant microRNA-142 in Treg, miRNA-142-5p, represses PDE3B expression which is one of the key mechanisms how Treg harbor more intracellular cAMP which is essential for their suppressive capacity. Treg-specific deletion of miR-142 in mice led to a lethal autoimmune syndrome due to an impaired autoimmune tolerance (Anandagoda et al. 2019). Notably, the pharmacological inhibition of PDE3 with Cilostamide showed beneficial effects on skin allograft rejection (Feng et al. 2011).

3.3.3.4 PDE4

The PDE4 family comprises four isoforms with PDE4A, PDE4B and PDE4D being the predominant forms expressed in CD4+ T cells (Landells et al. 2001). Upon TCR stimulation, PDE4A/D are upregulated whereas PDE4B expression showed only transient upregulation within the first 24h upon anti-CD3/CD28 stimulation (Peter et al. 2007). During T cell activation PDE4 forms a complex with ß-arrestin that is then transported to lipid rafts to regulate cAMP as a negative feedback loop (Bjørgo and Taskén 2006). PDE4 as the predominant PDE in T cells has been studied extensively over many years and linked to different autoimmune diseases. The inhibition of PDE4 led to lower IL-2, IFN-γ and IL-5 release (Arp et al. 2003; Foissier et al. 1996; Peter et al. 2007). Moreover, siRNA-mediated KO of PDE4D also reduced T cell proliferation (Peter et al. 2007). Current anti-inflammatory treatments also target PDE4: Roflumilast for chronic obstructive pulmonary disease, Apremilast for psoriasis and Crisaborole for moderate atopic dermatitis (Baillie, Tejeda, and Kelly 2019).

3.3.3.5 PDE7

The cAMP-specific PDE7 has two isoform PDE7A and PDE7B with each three splice variants determining the cellular localization. In CD4+ T cells, predominantly expressed isoform is PDE7A localized in the Golgi apparatus and during T cell activation PDE7A1 and PDE7A3 expression were upregulated (Szczypka 2020; Kanda and Watanabe 2001; Glavas et al. 2001). Resting naïve CD4+ T cells express more PDE7A1 than memory T cells (Nueda et al. 2006). Moreover, PDE7 suppressed T cell proliferation and Il-2 production (Li, Yee, and Beavo 1999). The pharmacological inhibition of PDE7

was beneficial for the clinical outcome in EAE, an animal model for multiple sclerosis (Redondo et al. 2012). Nevertheless, a study on PDE7A-deficient mice demonstrated preserved T cell function and PDE7B knock-out (KO) mice showed normal inflammatory cell infiltration indicating that depletion of PDE7 does not impair T cell function (Yang et al. 2003; Chevalier et al. 2012).

3.3.3.6 PDE8

PDE8, with PDE8A being the predominant isoform in lymphocytes, is the cAMP-specific phosphodiesterase with the highest affinity (K_m 0.15 µM) that plays a critical role in the regulation of T cell function (Bender and Beavo 2006). Treg harbor significantly lower PDE8A compared to Tcon, but PDE8A expression can be induced with TCR stimulation in both subsets (Glavas et al. 2001; Vang et al. 2010; Vang et al. 2016). The functional consequences of differential PDE8A expression between both T cell subsets are evident in cellular adhesion and motility. Naïve Treg adhere twofold more potently than naïve Tcon cells, which is blunted by TCR activation resulting in an increased PDE8A expression (Basole et al. 2017). Pharmacological inhibition of PDE8 by PF-04957325 decreases integrin-mediated adhesion by reducing the expression of adhesion molecules and chemokine release in Tcon. In contrast, Treg motility remains unaffected by PDE8 inhibition (Basole et al. 2017). The pathophysiological relevance of PDE8A was firstly demonstrated with the ovalbumin-induced allergic airway disease (AAD) mouse model which showed upregulation of PDE8A in CD4+ population (Vang et al. 2016). More recent studies confirmed that PDE8 inhibition influences the disease progression in the EAE model further supporting its role in inflammatory diseases (Basole et al. 2022).

3.4 Detection of cAMP via Förster Resonance Energy transfer (FRET) live-cell imaging

Traditional methods used in cyclic nucleotide studies involved protein binding assays or radioactive immunoassays to quantify cAMP levels (Brooker, Terasaki, and Price 1976; Gilman 1970). Further development that enabled monitoring temporal and spatial cyclic nucleotide dynamics is Förster resonance energy transfer (FRET) live-cell imaging. FRET was discovered by Theodor Förster in 1948 and is a distance-dependent, but non-radiative energy transfer from a donor to an acceptor

fluorophore when the distance is less than 10nm, the donor emission spectrum is overlapping at least 30% with the acceptor excitation spectrum and the dipoles of the fluorophores are correctly orientated to each other (Förster 1948). The Jablonski diagram in **Figure 4A** shows the phenomenon of FRET. When the donor fluorophore is excited by light with a wavelength matching the excitation spectrum, one electron absorbs a photon and raises from S_0 (singlet state) to an excited energy state (S_1). When the acceptor is in close proximity, the energy from the relaxation is transferred to the acceptor by dipole-dipole interactions. The electron in the acceptor molecule raises to the excited state and releases a photon when it comes back to the S_0 state. In the case of FRET exciting the donor fluorophore causes a decrease in the donor's fluorescence and an increase in the acceptor's fluorescence due to the energy transfer. The efficiency of FRET (E) is dependent on the actual distance (r) between the fluorophores and the acceptor and the Förster distance R_0 standing for the distance where FRET efficiency is 50 %. R_0 depends on e.g. on the spectral overlap, the dipole orientation and the quantum yield. The efficiency of FRET can be described with the following equitation:

$$E = \frac{R_0^6}{(R_0^6 + r^6)} \quad (1)$$

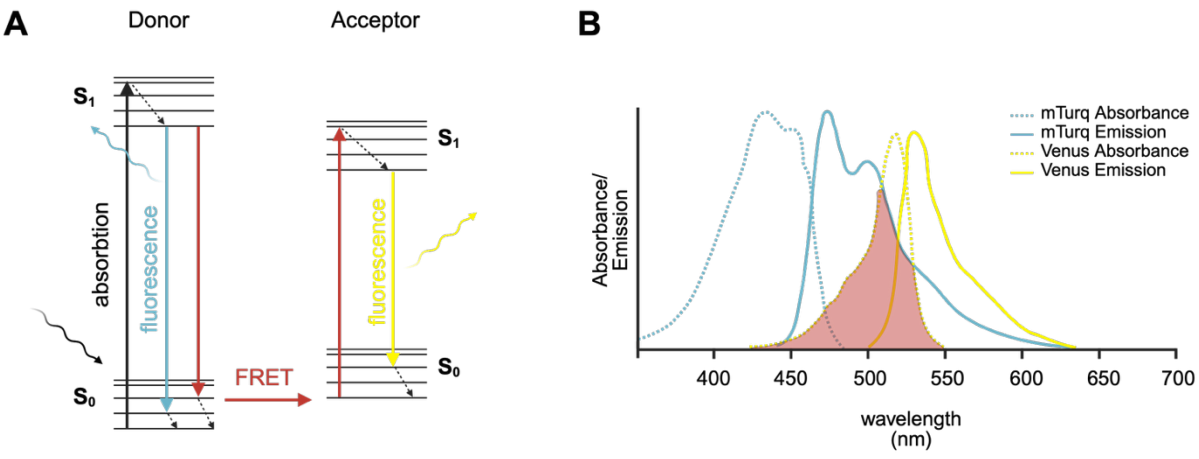


Figure 4: Principle of Förster Resonance Energy Transfer (FRET). (**A**) Jablonski diagram. After excitation of the fluorophore, one electron is raised from the singlet state (S_0) to the excited state (S_1) by absorption of a photon. The energy is released during the relaxation either by fluorescence or by Förster resonance energy transfer to the acceptor fluorophore. The energy leads then to the excitation of the acceptor electron and to the emission of a photon when this falls back to singlet state (S_0). (**B**) Absorption and Emission spectrum of the donor (mTurquoise; mTurq) and acceptor fluorophore

(td-cp Venus; Venus). The spectral overlap between donor emission and acceptor absorbance is depicted in red. The image was created with Biorender.com.

Most recently published biosensor is cAMP Fluorescence Imaging Reporter based on Epac, short cAMPFIRE, with three variations differing in their affinity to cAMP: cAMPFIRE-L with EC_{50} = 2.7 μM, cAMPFIRE-M with EC_{50} = 1.45 μM and cAMPFIRE-H with EC_{50} = 0.38 μM (Massengill et al. 2022). The cAMPFIRE biosensor contains an improved Epac1-based cyclic nucleotide-binding domain and two fluorophores: mTurquoise2 (mTurq) as donor fluorophore and Tandem dimer-circularly permutated Venus (td-cpVenus) acceptor fluorophore (Massengill et al. 2022). The spectral overlap of these fluorophores ranges from 450-550 nm (**Figure 4B**). In comparison to the previous Epac-based biosensors with CFP/YFP fluorophores the mTurqouise2/Venus pair has a higher quantum yield that increases the R_0 (Goedhart et al. 2012). Additionally, the tandem dimer of Venus increases the FRET efficiency because the number of acceptors correlated with R_0 (Koushik, Blank, and Vogel 2009). A transgenic mouse model expressing the FRET sensor cAMPFIRE-M ubiquitously enables real-time measurements in primary cells (Nakashima et al. 2025). The principle of the cAMPFIRE-M biosensor is shown in **Figure 5A**. cAMP binds to the cyclic nucleotide binding domain and induces a conformational shirt. The two fluorophores mTurq and td-cpVenus move apart and the larger distance stops the FRET that was occurring in the unbound state. Upon cAMP stimulation the decrease in FRET results in an increase in the donor fluorescence and in a decrease in the acceptor fluorescence (**Figure 5B**).

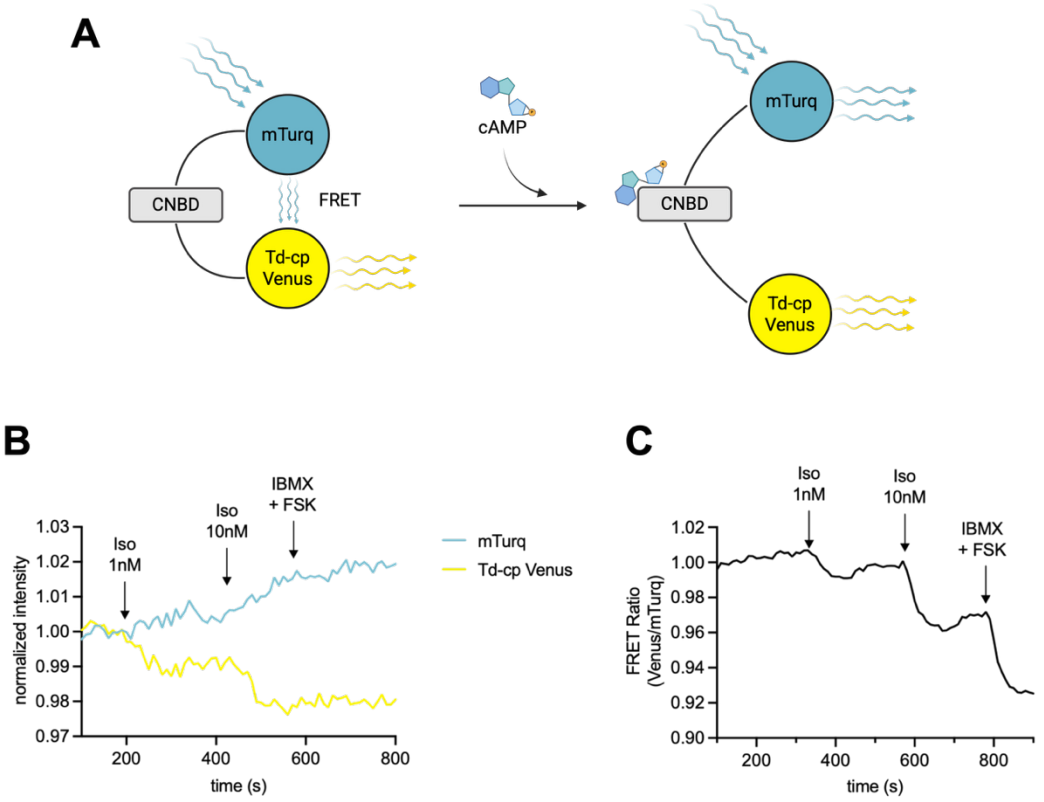


Figure 5: FRET measurements with cAMPFIRE-M biosensor. (**A**) Schematic principle of the cAMPFIRE-M biosensor. When cAMP binds to the cyclic nucleotide binding domain (CNBD) a conformational shift is induced and the distance between both fluorophores mTurquoise2 (mTurq) and td-cp Venus is enlarged and no FRET occurs. (**B**) Fluorescence intensity of the donor and acceptor fluorophore and (**C**) FRET Ratio (Venus/mTurq) during live-cell imaging. Intracellular cAMP levels were increased by increasing concentrations of isoproterenol (ISO) and IBMX/Forskolin treatments. Image was created with Biorender.com.

4 Aim of this work

The regulation of the immune response by T cells is of critical importance in the healing process of the heart after MI. However, the molecular mechanisms controlling the T cell function in the context are poorly understood. To address this gap, this PhD thesis focuses on the regulation of the cAMP signaling pathway in T cells. The main emphasis on the β-adrenergic receptor signaling and the degradation of intracellular cAMP mediated by PDE. This work was divided in two central objectives:

4.1.1 Visualization of cAMP signaling and the regulation of intracellular cAMP mediated by PDE in T cell responses after MI

To achieve the overall aim, it was crucial to monitor intracellular cAMP dynamics in T cells isolated from the heart-draining mediastinal lymph nodes (local response) and isolated from the spleen (systemic response) at different time points during the post-MI healing process. In FRET live-cell imaging the responsiveness of β-adrenergic receptors was compared between Sham and MI mice. Furthermore, with the commercially available selective PDE inhibitors the cAMP activity upon inhibition of the most abundant PDE was determined via FRET measurements.

4.1.2 Elucidating the role of PDE2A as a regulator of the cAMP-to-cGMP cross-talk in T cell responses after MI

The second aim was to investigate the impact of PDE2A on T cell responses following MI. For this purpose, a genetically modified CD4-specific PDE2A knockout (cKO) mouse line was subjected in a MI mouse model. The phenotypic characterization of the cardiac function is based on echocardiography and immunohistochemistry. Additionally, the immunological/biology perspective is investigated by immunoblotting and ELISA.

5 Material and Methods

5.1 Material

5.1.1 Animals

Mouse lines used in this work are listed in Table 1.

Table 1: Mouse lines.

Mouse line	Genetic background	Origin
cAMPFIRE-M	C57/BL6J	Laurinda Jaffe
$PDE2A^{flox}CD4^{cre}$	C57/BL6J	Viacheslav O. Nikolaev

5.1.2 DNA oligonucleotides

DNA oligonucleotides were used for polymerase chain reaction (PCR) to analyze the genotype of $PDE2A^{flox}CD4^{cre}$ mice and for qRT-PCR. The sequence of the DNA oligonucleotides from Eurofins Genomics (Ebersberg) are listed in Table 2.

Table 2: DNA Oligonucleotides for PCR.

DNA Oligonucleotides	Sequence
Cre forward	5´ GCGGTCTGGCAGTAAAAACTA 3´
Cre reverse	5´ GTGAAACAGCATTGCTGTCACTT 3´
PDE2A forward	5´ ACTGGTCAGTTCTGAGCCTCACCC 3´
PDE2A reverse	5´ AGTCTGGACTCCCCATCTAGCAGG 3´
PDE8 forward	5´ AGCTGGCTGTGCTCTACAAC 3´
PDE8 reverse	5´ AGTGTCCGGTAGTCATTCCTCT 3´
TBP forward	5´ GTAGCGGTGGCGGGTATC 3´
TBP reverse	5´ CATGAAATAGTGATGCTGGGA 3´

5.1.3 Antibodies

Primary and secondary antibodies for immunoblotting are listed in Table 3 and Table 4.

Table 3: Primary antibodies.

Primary Antibody	dilution	Manufacturer	Catalog number
Anti-GAPDH	1:150000	HyTest	5G4
Anti-PDE2A	1:1000	Proteintech	
Anti-PDE3B	1:2500	kind gift from Dr. Sergei Rybalkin	
Anti-PDE4B	1:2000	abcam	ab170939
Anti-PDE4D	1:2000	abcam	ab171750
Anti-pPKA substrates	1:1000	Cell signaling	9621
Anti-Tyrosine Hydroxylase	1:1000	Sigma	Ab152

Table 4: Secondary antibodies.

Secondary Antibody	dilution	Manufacturer	Catalog number
Goat anti-mouse	1:5000	Biorad	170-5047
Goat anti-rabbit	1:5000	Biorad	170-5046

5.1.4 Chemicals

Chemicals used in this work are listed in Table 5.

Table 5: Chemicals.

Chemical	Manufacturer	Catalog number
(-)-Isoproterenol hydrochloride	Sigma Aldrich	#I6504-100MG
20 % SDS-Solution	AppliChem	A0675-1L
3-Isobutyl-1-Methylxanthine (IBMX)	AppliChem	#A0695-0001
37 % Hydrochloric acid (HCl)	Carl Roth	9277.1

4-(2-hydroxyethyl)-1-piperazineethanesulfonic acid (HEPES)	Sigma Aldrich	#H4034-500G
50x Tris-acetate-EDTA (TAE) buffer	AppliChem	A1691,1000
Agarose universal peqGold	VWR	35-1010
Ammonium persulfate (APS)	Sigma Aldrich	A3678-25G
BAY 60-7550	Santa Cruz	#sc396772
Bromophenol blue sodium salt	Carl Roth	A 512.1
Calcium chloride	Sigma Aldrich	#C8106
Cilostamide	Santa Cruz	#sc201180A
Dapi Fluoromount G	Southern Biotech	0100-20
Direct PCR Lysis Reagent	Viagen	102-T
DNS ladder, 100bp	New England biolabs	N3231S
dNTP mix	Promega	U1511
Ethylenediaminetetraacetic acid (EDTA)	AppliChem	A1104, 0500
Forskolin	Hello Bio	#HB1348-10MG
Gel Loading Dye Purple, 6x	New England Biolabs	B7025S
Glycerol	Millipore	356350-500ML
Glycine	Carl Roth	3908.3
GoTaq reaction buffer	Promega	M7911
L-ascorbic acid	Sigma Aldrich	#A0278
Magnesium chloride hexahydrate	Sigma Aldrich	#M2670
Methanol 99 %	Thermo Scientific	L13255.0F
Midori Breen	Nippon Genetic	MG04
N,N,N',N'-Tetramethylethylenediamine (TEMED)	Sigma Aldrich	T9281-100ML

NECA	tocris	#1691
PF-04957325	MedChem	#HY-15426
Poly-D-lysine hydrobromide	Sigma Aldrich	#P1149-10MG
Ponceau S	Sigma Aldrich	P3504-10G
Potassium chloride	Sigma Aldrich	#P9541-500G
Powdered milk	Carl Roth	T145.2
Protein Ladder (10-250 kDa)	Thermo Scientific	26619
Proteinase K	AppliChem	A3830, 0500
Rolipram	Sigma Aldrich	#6520-10MG
ROTI Histofix	Carl Roth	P087
Rotiphorese Gel 30 (37,5:1; Acrylamide)	Carl Roth	3029.1
Sudan black	Roth	0292.1
Tris-(hydroxymethyl)-aminomethane (TRIS)	Carl Roth	4855.2
Triton X-100 Solution, 10 %	AppliChem	A1287,0100
Tween 20	Sigma Aldrich	P1379-500ML
β-Mercaptoethanol	Sigma Aldrich	M6250-100ML

5.1.5 Cell culture

Reagents used for cell culture are listed in Table 6.

Table 6: Cell Culture reagents.

Reagent	Manufacturer	Catalog number
Bovine serum albumin (BSA)	Sigma Aldrich	#A6003-25MG
Dulbecco's Phosphate buffered saline (DPBS)	Sigma Aldrich	#D8537
FCS	Sigma Aldrich	#F4135-500ML
L-Glutamin solution	Sigma Aldrich	#G7513-100ML

LEAF purified Anti-ms CD28 ab	Biolegend	#102102
MEM non-essential amino acids	Gibco	#11140050
Na-Pyruvate	Gibco	#11360070
Penicillin/Streptomycin	Sigma Aldrich	# P0781-100ML
Recombinant Murine IL-2	Fisher scientific	#212-12
RPMI 1640	Gibco	#42401018
Tryphan blue	Biochem	#L6323
Ultra LEAF purified Anti-ms eCD3 ab	Biolegend	#100340
β-mercaptoethanol	Gibco	#31350010

5.1.6 Kits

Kits used in this work are listed in Table 7.

Table 7: Kits.

Kit	Manufacturer	Catalog number
CD4+ T cell isolation Kit, mouse	Miltenyi Biotech	130-104-454
IFN-γ ELISA MAX DELUXE	Biolegend	430804
iScript cDNA Synthesis Kit	BioRad	170-8891
RNeasy Plus Micro Kit	Qiagen	74034
RNeasy Fibrous Tissue Mini Kit	Qiagen	74104
SuperSignal West Pico PLUS	Thermo Scientific	34580
SyberGreen (Perfecta) for IQ	QuantaBio	95053-500

5.1.7 Consumables

Consumables used in this work are listed in Table 8.

Table 8: Consumables.

Consumables	Manufacturer	Catalog number
2 mL Syringe	BD Emerald	#307727
24-well plates	Sarstedt	#83.3922.500
6-well plates	Sarstedt	#83.3920
96-well plate, flat bottom	Sarstedt	#83.3924
Amersham Protran 0,45 NC, nitrocellulose	Cytiva	10600002
Bacillol 30 Foam	Hartmann	ANY8.1
Falcon tube, 15 mL	Sarstedt	62.554.016
Falcon tube, 50 mL	Sarstedt	62.559.004
Filter paper, Type 598	Hahnemühle	5984657
Filtropur S 0,2 Syringe Filter	Sarstedt	83.1826.001
Glass coverslips 25mm	VWR	#631-0171
Gloves S (nitrile, powder free)	Medimex	700103
Kimtech	Kimberly Clark	P502.1
Laboratory film	Parafilm	PM-996
LS column	Miltenyi Biotech	#130-042-401
Luer-Lok syringe 50 mL	BD Plastipak	300865
MACS SmartStrainer 30µM	Miltenyi Biotech	#130-098-458
Microcentrifuge tube 1.5 mL	Sarstedt	72.690.001
Microcentrifuge tube 2 mL	Sarstedt	72.691
PCR 0.1 mL tube	Biozym	711200
Pipette tips 10 µL	Sarstedt	70.1130.600
Pipette tips 1000 µL	Sarstedt	70.3050.100

Pipette tips 200 µL	Sarstedt	70.760.502
PluriStrainer, 30 µM	pluriSelect	43-50030-03
Round glass coverslips, 25 mm	VWR	631-0171
Safe Seal reaction tubes, 1.5 mL	Sarstedt	72.706.400
Safe Seal reaction tubes, 2 mL	Sarstedt	72.695.500
Serological pipette 10 mL	Sarstedt	86.1254.001
Serological pipette 2 mL	Sarstedt	86.1252.001
Serological pipette 25 mL	Sarstedt	86.1685.001
Serological pipette 5 mL	Sarstedt	86.1253.001
Serological pipette 50 mL	Sarstedt	86.1256.001
Softa-Man acute	Braun	19114

5.1.8 Devices and instruments

Devices and instruments used in this work are listed in Table 9.

Table 9: Devices and instruments.

Device/instrument	Manufacturer
Accu-jet pro Pipette Controller	Brand
Arduino board	Arduino
Centrifuge 5810 R	Eppendorf
Centrifuge Fresco 17	Thermo Scientific
Centrifuge Megafuge 8R	Thermo Scientific
Centrifuge Pico 17	Thermo Scientific
CMOS camera (OptiMOS)	QImaging
CO_2-incubator MCO-5AC	Sanyo
DV2 CUBE 05-EM, 505 dcxr, D480/30nm, D535/40nm	Photometrics
E-box Gel documentation	Vilber

FlexStation3 Multi-Mode Microplate Reader	Molecular devices
Freezer	Liebherr
Fridge	Liebherr
Gene Touch (PCR Machine)	Bioer
Glacier Ultralow temperature freezer	Nuaire
HERAcell vios 160i CO_2- Incubator	Thermo Scientific
HP Elite Display E241i	HP
HP EliteDesk 800nG1 TWr	HP
Laboclav	HSP
Laboratory balance	Precisa
LED pE-100 440nM	CoolLED
Leica DMI 3000B	Leica
MACS MultiStand	Miltenyi Biotec
Magnetic stirrer	IKA
MaxQ4450 Benchtop Orbital Shaker	Thermo Scientific
Microcentrifuge	VWR
Microwave	Panasonic
Mixing Block MB-102	Bioer
Neubauer improved count chamber	Marienfeld Superior
pH meter, Level 1	inoLab
Precision Scale	KERN PCB
Research Plus (10-1000 μL)	Eppendorf
Research Plus pipettes	Eppendorf
Rotor Gene-Q Cycler	Qiagen
Shaker DRS-12	ELMI
Shaker SSL4	Stuart
Sonoplus GM mini20	Bandelin
Thermomixer C	Eppendorf
Western Blot equipment	BioRad

5.1.9 Software

Software used in this work is listed in Table 10.

Table 10: Software.

Software	Company
BioRender	BioRender
Claude Sonnet 4.6	Antrophic
Endnote	Microsoft
Excel	Microsoft
GraphPad Prism	Graphpad
ImageJ	National Institutes of Health
Micro-Manager	Open Source Microscopy
NDP.view 2	Hamamatsu
nSolver analysis software 4.0	Nanostring Technologies
PowerPoint	Microsoft
PyCharm	JetBrains
Tbase, 4D	4D SAS
Word	Microsoft

5.1.10 Buffers

5.1.10.1 Buffers used for histological analysis

Buffers used for the histological analysis are listed in Table 11.

Table 11: Buffers used for histological analysis.

Buffer	Compound
Citrate buffer	2.94 g Tri-sodium citrate (dihydrate) in 1 mL H_2O
	0.5 mL Tween 20
	pH 6.0
IHC washing buffer	1 x TBS buffer
	0.05 % (v/v) Tween 20

Sudan black B dilution	0.2 % (v/v) in 70 % ethanol
Sudan black B stock	1 % (m/v) in 100 % ethanol
TBS buffer 10x	100 mM Tris 1.5 M NaCl pH 7.5

5.1.10.2 Buffers used for Cell culture methods

Buffers used for primary CD4+ T cell isolation and cardiomyocyte isolation are listed in Table 12 and Table 13.

Table 12: Buffers used for CD4+ T cell isolation and culture.

Buffer	Compound
MACS buffer	0.5 % (w/v) BSA in DPBS (without Ca^{2+}/Mg^{2+})
Supplement 1	2 mM L-Glutamine solution 1x MEM non-essential amino acids 1 mM Na-Pyruvate 100 µg/mL Penicillin/Streptomycin 30 µM β-mercaptoethanol 5 % (v/v) FCS, heat-inactivated
Supplement 2	5 % (v/v) Heat inactivated FCS
T cell culturing medium	40 mL RPMI 1640 4.23 mL Supplement 1 2.3 mL Supplement 2

Table 13: Buffers used for cardiomyocyte isolation.

Buffer	Compound
1x Perfusion buffer	113 mM NaCl 4.7 mM KCl 0.6 mM KH_2PO_4 0.6 mM $Na_2HPO_4x2H_2O$ 1.2 mM $MgSO_4x7H_2O$ 12 mM $NaHCO_3$

	10 mM $KHCO_3$
	10 mM HEPES
	30 mM Taurine
	5.6 mM D-(+) Glucose
	9.9 mM BDM
Digestion buffer	29.5 mL 1x Perfusion buffer
	3.75 µL 100 mM $CaCl_2$
	100 µL 2.5 % Trypsin
	300 µL (= 30 mg) Collagenase
Stop buffer 1	2.25 mL 1x Perfusion buffer
	250 µL FCS solution
	1.25 µL 100 mM $CaCl_2$
Stop buffer 2	9.5 mL 1x Perfusion buffer
	500 µL FCS solution
	3.75 µL 100 mM $CaCl_2$

5.1.10.3 Buffers used for microscopical methods

Buffers used for FRET live-cell imaging are listed in Table 14.

Table 14: Buffers used for FRET live-cell measurements.

Buffer	Compound
FRET Buffer	1mM $CaCl_2$
	10 mM HEPES
	544 mM KCl
	1mM $MgCl_2$ x $6H_2O$
	144 mM NaCl
	pH 7.4
PDL	0.1 mg/mL

5.1.10.4 Buffers used for protein biochemistry methods

Buffers used for protein biochemistry methods are listed in Table 15 and Table 16.

Table 15: Buffers used for sample preparation.

Buffer	Compound
4x Laemmli buffer	2.4 g 1 M Tris, pH 6.8
	40 mL Glycerol
	40 mL 20% SDS Solution
	0.2 g Bromophenol blue sodium salt
RIPA buffer	1mM EDTA, pH 8.0
	150 mM NaCl
	0.1 % (v/v) SDS
	1 % NaDOC
	20 mM Tris, pH 7.5
	1 % Triton X-100

Table 16: Buffers used for SDS-PAGE and immunoblotting.

Buffer	Compound
4 x Tris/SDS, pH 6.8	0.4 % (v/v) 20 % SDS solution
	500 mM Tris (pH 6.8)
4 x Tris/SDS, pH 8.8	0.4 % (v/v) 20 % SDS solution
	1.5 M Tris (pH 8.8)
APS	10 % (w/v)
10 x SDS Running buffer, pH 8.3	1.9 M Glycine
	250 mM Tris
	1 % (v/v) SDS solution
10 x Transfer buffer	1.9 M Glycine
	325 mM Tris
1 x Transfer buffer	20 % (v/v) Methanol
	1x Transfer buffer
10 x Tris-buffered saline (TBS) buffer, pH 7.4	1.5 M NaCl
	100 mM Tris
TBS-T buffer	0.1 % (v/v) Tween 20
	1x TBS buffer
Blocking buffer	0.5 % - 5 % (w/v) powdered non-fat milk
	in 1 x TBS-T buffer

5.2 Methods

5.2.1 *In vivo* experiments

5.2.1.1 Animals

Ten to twelve-week-old wild-type (WT) and transgenic mice (TG), both males and females, were used in conducting this study. Animals were kept and bred in the central animal facility of the University Medical Center Hamburg-Eppendorf (UKE) under pathogen-free conditions. The mice were kept in a 12 h light/dark cycle and had excess to chow and water *ad libitum*. Two weeks before the start of the *in vivo* experiments, the mice were transferred to the experimental barrier. Animals were handled following national and international animal welfare guidelines authorized by Behörde für Justiz und Verbraucherschutz Hamburg (N26/2023 and ORG1113).

5.2.1.2 cAMPFIRE-M biosensor mice

C57BL/6J mice expressing global cAMPFIRE-M biosensor were previously generated by Prof. Laurinda Jaffe (Nakashima et al. 2025). Shortly, the cAMPFIRE-M expression cassette was inserted into intron 1 of the *Rosa26* locus mediated by CRISPR/Cas9 gene editing and bred with Hprt-Cre to generate the global expression. In this study, all mice used in this study were homozygous for the ubiquitous expression of the cAMPFIRE-M biosensor.

5.2.1.3 Generation of a PDE2A conditional Knock-Out (cKO)

The CD4+ T cell specific Knock-Out of PDE2A mice (C57BL/6J background) was generated by crossing $PDE2A^{flox}$ (Carlantoni et al. 2024) and $CD4^{cre}$ mice (Jackson Laboratories strain #022071; provided by Dr. Rainer Meiler). This line was maintained by breeding heterozygous littermates ($PDE2A^{fl/+}$ $cre^{+/-}$ x $PDE2A^{fl/+}$ $cre^{-/-}$) producing PDE2A cKO mice ($PDE2A^{fl/fl}$ $cre^{+/+}$) and littermate controls ($PDE2A^{+/+}$ $cre^{+/+}$).

5.2.1.4 LAD Ligation

The MI was induced in the mouse model via permanent ligation of the left anterior descending (LAD) artery. 10- to 12-week-old mice were anaesthetized with isoflurane, injected with Buprenorphine and intubated for mechanical ventilation during surgery. The third left intercostal space was opened to reach the heart. Then, the LAD artery was permanently tied off with a suture. Afterwards, the chest was closed, and mice

were treated with analgesics for 7 days. The control group are Sham operated mice which underwent the same surgery except the suture around the LAD artery. LAD ligation surgeries were performed by Svenja Kupsch.

5.2.1.5 Echocardiography

The cardiac function of the mice was monitored by transthoracic echocardiography using *VisualSonics Vevo 3100*. The mice were anaesthetized with 1-2 % isoflurane on a heat plate. Echocardiography was performed and analyzed in B- and M-mode of the short and long axis view by Svenja Kupsch.

5.2.1.6 Tissue collection

Total body weight was measured, and mice were sacrificed by cervical dislocation under anesthesia. The heart and lung weight was determined on a micro scale. The heart was dissected in three parts. The base and apex were snap-frozen in liquid nitrogen and stored at -80°C for further analysis. The Cross-sectional heart tissue was fixed in 4 % Paraformaldehyde (PFA) over night for histological staining. The tibia was isolated from skin and soft tissue and its length measured using a caliper.
For the immune cell isolation from spleen and lymph nodes, the organs were separately collected in ice-cold PBS and homogenized through a 40 µM cell strainer to generate a single cell suspension.

5.2.2 Nucleotide methods

5.2.2.1 DNA Extraction

Experiments in this study were preformed using transgenic mice with the PDE2A^{flox}CD4^{cre} system. To determine the genotype a tail biopsy was taken by the animal care takers and lysed to extract the DNA. For this, biopsies were incubated in directPCR tail lysis buffer containing proteinase K (20 µg/mL) for at least 6 h. Lysis was finalized with a 45-minute incubation at 85°C and stored at 4°C.

5.2.2.2 Polymerase Chain Reaction (PCR)

After DNA lysis a PCR was conducted to determine the genotype. The PCR reaction mix is described in Table 17.

Table 17: Master Mix for Genotyping.

reagent	1x
5x green buffer	5 µL
dNTPs	0.5 µL
Forward Primer	1 µL
Reverse Primer	1 µL
Polymerase	0.5 µL
ddH_2O	15 µL
DNA	2 µL

The amplification of the DNA fragments was conducted in a GeneTouch Thermal Cycler using the following conditions (Table 18).

Table 18: PCR program for PDE2A and Cre genotyping.

Temperature	Time	Cycle
95°C	4 min	
95°C	30 sec	x30
62°C	30 sec	
72°C	1 min	
72°C	10 min	
4°C	∞	

The PCR products were analyzed by electrophoresis on 2 % agarose gels prepared in 1x TAE buffer containing Midori Green (6 µL per 100 mL). A 100 bp DNA ladder was included on each gel for fragment size determination. Electrophoresis was performed at 100 V for 30 min and the separated DNA samples were visualized under UV light.

5.2.2.3 RNA Isolation

RNA was isolated from frozen heart tissue with the RNeasy® Fibrous Tissue Mini Kit according to the manufacturer's instructions. Briefly, the tissue was homogenized in 300 µL RLT buffer containing 10 % β-mercaptoethanol and digested with proteinase K at 55°C for 10 min. After centrifugation for 3 min at 17000 rpm the supernatant was transferred to a new tube and mixed with 100 % ethanol. The suspension was

subsequently applied to a RNeasy Mini Column, centrifuged for 15 s at 17000 rpm and the flow-through was discarded. The column was washed once with RW1 buffer, centrifuged again and incubated with DNase for 15 min at room temperature. After another 15 s centrifugation step, the column was washed with RW1 and two times with RPE buffer. Finally, the membrane was dried in a 2 min centrifugation at 17.000 rpm and the RNA was eluted in 20 µL RNase-free water.

RNA from T cells was isolated with RNAeasy Plus Micro Kit according to manufacturer's protocol. Briefly, the cells were washed with PBS, lysed in 350 µL RLT buffer containing 10 % β-mercaptoethanol, mixed with 350 µL and transferred to a gDNA Eliminator Spin column. After a centrifugation step for 30 s at 13000 rpm, 70 % ethanol was added to the flow-through and the suspension was subsequently transferred to a RNeasy MinElute spin column. After a 15 s centrifugation step, 700 µL RW1 buffer was added to the column followed by another 15 s centrifugation step. Then, 500 µL RPE buffer was added to the column and after another centrifugation step 80 % ethanol was pipetted on top of the column. Lastly, the column was centrifugated for 2 min in with closed lid and then for 5 min with open lid. Finally, RNA was eluted with 14 µL RNase-free water during a 1 min centrifugation. The RNA concentration was measured with *DeNovix DS-11* and samples were stored at -80°C.

5.2.2.4 cDNA synthesis

Isolated RNA from T cells was further used for complementary DNA (cDNA) by using the iScript cDNA Synthesis Kit following the manufacturer's protocol. **Table 19** and **Table 20** summarize the reaction mix and the cycling steps required for cDNA synthesis. Synthesized cDNA was stored at -20°C.

Table 19: Reaction mix for cDNA synthesis.

reagent	Volume
iScript RT	1 µL
RNA template	200 ng
5x iScript reaction mix	4 µL
Nuclease-free water	Up to 20 µL total volume

Table 20: Program for cDNA synthesis.

Temperature	Time
25°C	5 min
46°C	20 min
95°C	1 min
4°C	∞

5.2.2.5 qRT-PCR

The synthesized cDNA from CD4+ T cells was used for gene expression analysis with qRT-PCR. With the Primer-BLAST tool from NCBI primer pairs for the genes of interest were designed (**Table 2**). The reaction mix which was used for the qRT-PCR and the cycling conditions for the Rotor-Gene Q cycler (72-well rotor) are listed in **Table 21** and **Table 22**, respectively. The analyzed C_T values are determined with the Rotor-Gene Q software and Microsoft Excel. The target gene was normalized to the housekeeping gene with the following equitation.

$$\Delta C_T = C_T(gene) - C_T(housekeeping\ gene) \quad (2)$$

Table 21: qRT-PCR mix.

Component	Volume
cDNA (1:1)	1 µL
Forward Primer (25 nM)	0.5 µL
Reversed Primer (25 nM)	0.5 µL
SYBER Green	5 µL
RNAse-free water	3 µL
Total volume	10 µL

Table 22: Program for qRT-PCR.

Temperature	Time	
95°C	10 min	
95°C	10 s	50x
60°C	15 s	
72°C	20 s	
72-95°C	0.5°C/step	

5.2.3 Histological analysis

5.2.3.1 Tissue preparation for histological analysis

The cross-sectional heart tissue was fixed in 4 % PFA overnight and stored in PBS at 4°C. The tissue embedding in paraffin, heart sectioning in 4 µM slices and was performed by Kristin Hartmann (UKE mouse pathology core facility).

5.2.3.2 Immunohistochemistry of CD4 and Foxp3 positive cells

Immunohistochemistry analysis of cross-sectional heart tissue was carried out to quantify bulk CD4+ positive cells but also Treg (FoxP3+). Standard staining procedure was performed by Kristin Hartmann (UKE mouse pathology core facility) and images of the sections were taken using the *Sysmex Pannoramic MIDI II*. FoxP3 positive cells were counted manually of whole heart sections. The mean value of three to four 4 µM heart slides per mouse was calculated for n=3 mice per group.

5.2.3.3 Interstitial fibrosis

To quantify interstitial fibrosis the cross-sectional heart tissue was embedded in paraffin and stained with Picrosirius-red (PSR) by Kristin Hartmann at the UKE mouse pathology core facility. Whole slide images were analyzed using the Hamamatsu NDP.view2 software. For each heart three images at a 40x magnification were exported as .tiff format. The percentage of fibrotic tissue (labeled in red) was subsequently analyzed using a python pipeline. Briefly, the images were classified with K-Means into five classes depending on their composition score (brightness and saturation) and their Red/yellow ratio (**Figure 6A**). In the next step, each class was calibrated based on three images of each cluster with the L*a*b method. Red pixels were detected with a certain threshold for a. Yellow with a threshold set for b and the red dominance factor determined the ratio required to distinguish red from yellow. During the image processing, the contrast of each image was normalized using the Contrast Limited Adaptive Histogram Equalization (CLAHE) method and subsequently analyzed based on the class-specific thresholds. The percentage of fibrosis was determined as the percentage of red pixels (fibrosis) in relation to the total tissue area (red+yellow) (**Figure 6B**).

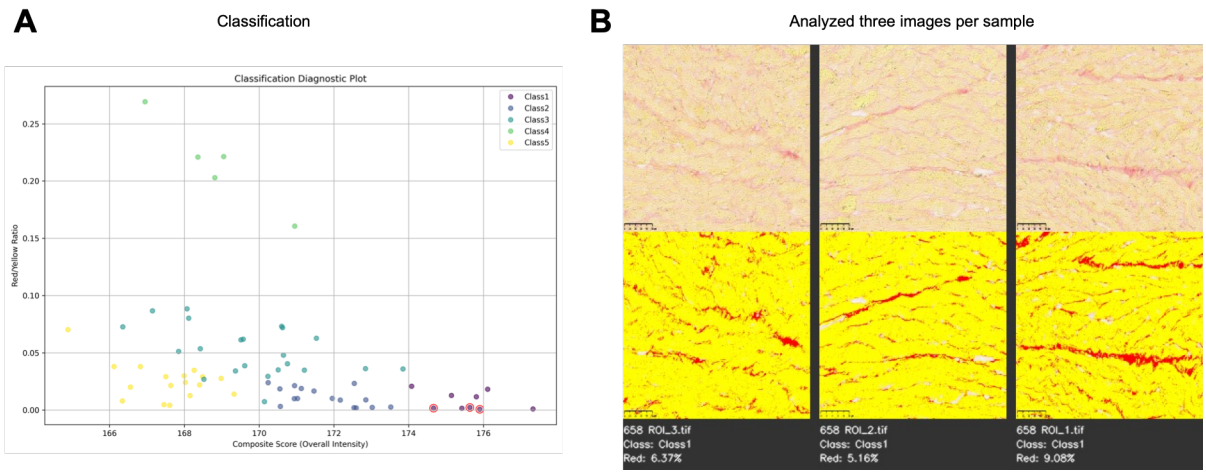


Figure 6: Automatic analysis of fibrotic area in heart cross-sectional areas. (**A**) All images were analyzed and classified in 5 classes with K-Means based on their composition score (brightness and saturation) and their red/yellow ratio. (**B**) 3 image areas were analyzed per sample with the respective thresholds of each class. The original images are depicted in the upper row and the analyzed image in the row below. Tissue area is labeled in yellow and the fibrotic area in red. No tissue areas are labeled in white. Scale bar = 50 µM.

5.2.3.4 Wheat germ agglutinin staining

Cross-sections of the hearts were stained with wheat germ agglutinin (WGA) to analyze the cardiomyocyte size. 4 µM heart tissue sections were dewaxed and hydrated in Xylol, and decreasing concentration of ethanol (Table 23).

Table 23: Tissue preparation for WGA staining.

Solution	Incubation (min)
Xylol 100 %	20
Xylol 100 %	20
Ethanol 100 %	3
Ethanol 100 %	3
Ethanol 96 %	5
Ethanol 90 %	5

Ethanol 80 %	5
Ethanol 65 %	5
Ethanol 50 %	5
Ethanol 25 %	5
Water	5

In the next steps, the slides were boiled in citrate buffer for 15 min, washed three times with TBS-T (0.1 % Tween-20). The area of interest was encircled with a Dako Pen and incubated with 30 µL wheat germ agglutinin (WGA) solution (75 µg/mL) for 30 min. Then, slides were washed three times with TBS-T. To quench auto-fluorescence 0.2 % Sudan black was added for 30 min. After another washing step in TBS-T and lastly in TBS, the slides were mounted with a *Fluoromount G mounting medium* and stored at 4°C. Images were taking with the green filter (wavelength 488 nm) and 15 ms exposure time using the the 20x Zeiss Plan-Apochromat objective in the *Sysmex Pannoramic MIDI II*.

5.2.3.5 Quantification of cardiomyocyte cross-sectional area

The quantification of the cardiomyocyte cross-sectional area was performed by Greta Boer. Two image sections were taken in the inner left ventricle at a 40x magnification for further analysis (**Figure 7A**). Importantly, each image contained mostly round cardiomyocytes. In the first step, each image was normalized to an equal fluorescence intensity (**Figure 7B**). Then, the machine-learning *Ilastik* pixel classifier was trained with 12 images to determine the background and labeled cell surface only using the green channel of each image. With that, a batch processing was performed to generate a probability map (green: cell boarder; red: background) to minimize the noise that would disrupt further analysis (**Figure 7C**). These images were further analyzed with *ImageJ*. A threshold for brightness in a range from 225-255 was applied and all cardiomyocytes were identified with a size between 900-8000 pixel^2 and circularity from 0.5-1.0 and their cell area analyzed (**Figure 7D**).

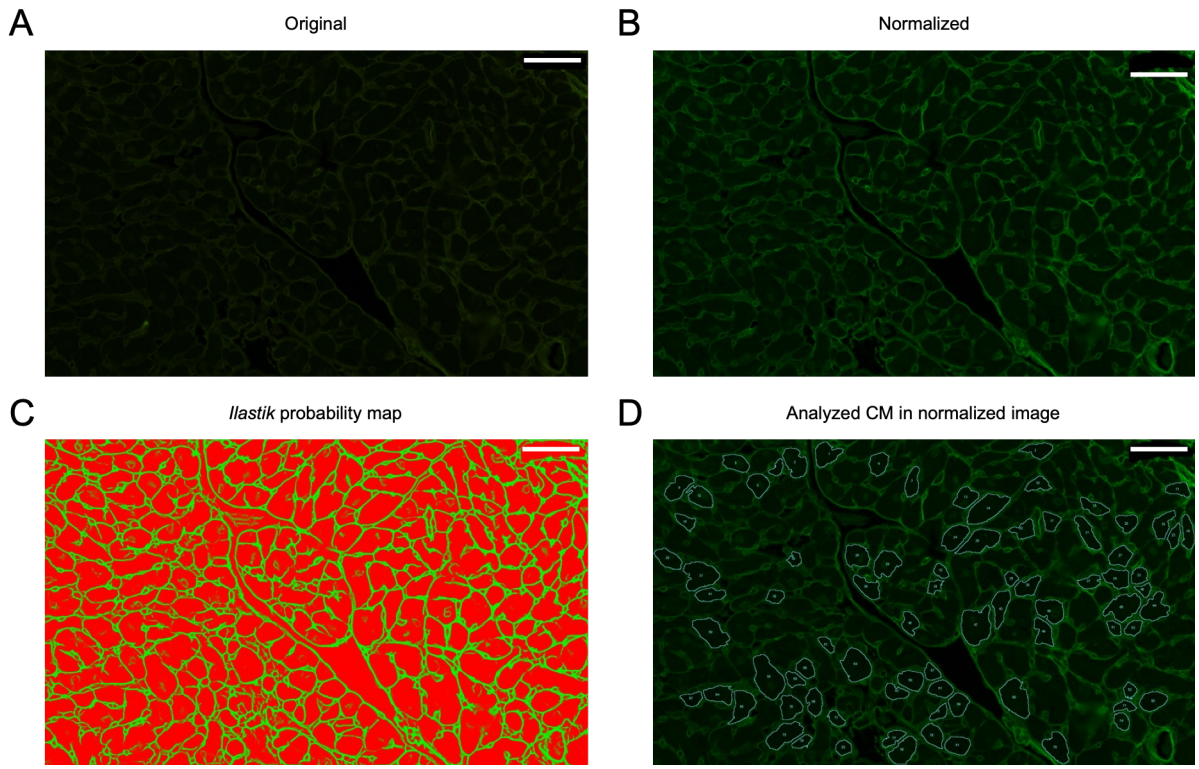


Figure 7: Determination of CM cross-sectional area in heart sections. (**A**) Original WGA image at 40x magnification. (**B**) Processed image with normalized fluorescence intensity. (**C**) Probability map classified with a trained algorithm in *Ilastik*. Background is labeled in red and the cell boarder in green. (**D**) Overlay of the normalized image with the analyzed cardiomyocytes (CM). Scale bar = 50 µM.

5.2.4 Cell Culture

5.2.4.1 Isolation of CD4+ cells

The single cell suspension of homogenized spleen and medLN was centrifuged at 400 xg for 5 min at 4°C, the supernatant was discarded, and the cell pellet resuspended in 5 mL ice-cold PBS. For cell count, 10 µL cell suspension was diluted 1:10 in trypan blue solution and counted in a Neubauer counting chamber. The rest of the cell suspension was again centrifuged (400 xg, 5 min, 4°C) before the CD4+ T cell Biotin Kit was used according to manufacturer's protocol for magnetic-activated cell sorting (MACS). For every 10^7 cells the cell pellet was resuspended in 100 µL MACS buffer and incubated for 15 min at 4°C with the CD4+ T cell Biotin-antibody cocktail (10 µL/10^7 cells). In the second step of the isolation, 30 µL/10^7 cells MACS buffer and 20 µL/10^7 cells Anti-Biotin Microbeads were added to the suspension. After another 15 min incubation at 4°C, the suspension was transferred to a pre-rinsed LS column placed on a string magnet. All microbeads-labeled cells bind to the magnetic column

and only the unlabeled CD4+ T cells were collected in the flow through. The column was washed one time with 3 mL MACS buffer before the cell suspension was centrifuged at 500 xg for 5 min at 4°C. The supernatant was discarded, and the cell pellet resuspended in RPMI complete media for cell culture. CD4+ cells were cultured overnight in the presence of 10 U/mL IL-2. For *in vitro* activation, plates were pre-coated with anti-CD3 antibody for 2 h at 37°C and soluble anti-CD28 antibody was added to the cell culture media.

5.2.4.2 Isolation of primary cardiomyocytes

Isolation of primary cardiomyocytes was conducted by Dr. Alexander Froese and Dr. Nadja Beck. After sacrificing the mice by cervical dislocation, the heart was dissected in ice cold PBS. Then, the aorta was cannulated with a blunt cannula and fixed with suture. The cannula was perfused for 3 min with 1x prewarmed perfusion buffer in a Langendorff perfusion system. Afterwards, the digestion buffer containing collagenase and trypsin was used for further perfusion. The atria were removed and the heart was cut into fine pieces for 30 s in 2.5 mL digestion buffer before adding 2.5 mL stop buffer 1 to the suspension. The heart was further mechanically disrupted by pipetting up and down with a needleless syringe for 3 min and filtered through gauze. After a 10 min incubation at room temperature the supernatant was discarded and 10 mL of Stop buffer 2 were used to resuspend the cell pellet. Finally, the re-calcification process was performed by adding increasing $CaCl_2$ concentrations every 4 min up to 100 nM to the cell suspension. For FRET, cardiomyocytes were seeded on Laminin-coated round glass coverslips (25 mm) and incubated for at least 1 h at 37°C and 5 % CO_2 before the measurements.

5.2.5 Microscopical methods

5.2.5.1 Förster Resonance Energy Transfer (FRET) Live-cell imaging

FRET live cell imaging enables the visualization of intracellular cAMP dynamics. For this purpose, CD4+ T cells were isolated from spleen or mediastinal lymph nodes of mice expressing the cytosolic cAMPFIRE-M biosensor. Non-activated and *in vitro* activated T cells were plated on Poly-D-Lysine 25 mm round glass coverslips for 30 min at 37°C. Non-attached cells were washed off afterwards. FRET measurements were performed with an Autoflour cell chamber containing 400 µL FRET buffer. The

treatment with different chemicals was started after a stable baseline was set. All chemicals were pre-diluted in FRET buffer and added slowly in a volume of 400 µL to the chamber. The measurements were performed at room temperature. Images were taken every 10 s with the *MicroManager 1.4* software. The inverted fluorescence microscope contained an oil-immersion 63x/1.4 objective, a CoolLED light source at 440 nM wavelength, a dual beam splitter DV2 Dual View (Cube 05-EM, 505 dxcr, D480/30m, D535/40m) and a CMOS camera chip. The raw data was analyzed using *Microsoft Excel.* The donor and acceptor fluorophores have a spectral overlap. Thus, raw FRET data was corrected with a bleed through factor and normalized to baseline afterwards. The FRET ratio was calculated with the following formula:

$$Ratio = \frac{Venus - b * mTurq}{mTurq} \quad (3)$$

5.2.6 Protein biochemistry methods

5.2.6.1 Sample preparation for immunoblotting

In the first step of the preparation of cell lysates, cultured CD4+ T cell suspension was transferred to a new Eppendorf tube and centrifuged for 5 min at 500 xg and 4°C. Afterwards, the supernatant was removed, the cells were washed with PBS and centrifuged again. After the second removal of the supernatant the cell pellets were resuspended in 20 µL 1x laemmli buffer, heated for 5 min at 95°C for protein degradation and stored at -20°C.

5.2.6.2 Sodium dodecyl sulfate polyacrylamide electrophoresis (SDS-PAGE)

20 µL of the prepared samples as described before were applied to a 10 % sodium dodecyl sulfate polyacrylamide (SDS-PAGE) gel. The gels were run for 15 min at 90 V, followed by 90 min at 140 V in 1x SDS-running buffer. Due to pore size and pH differences between the stacking and separating gel, all samples accumulate at the border of both gels and are further separated by size in the separation gel. The position of the protein in the separating gel correlates with the molecular weight of the protein. Thus, a molecular weight standard is also applied to the gel.

Table 24: Volume of each compound in Stacking and Separating gel.

Gel	Compound
Stacking gel	0.5 mL Acrylamide
	2.31 mL ddH_2O
	0.94 4x Tris/SDS, pH 6.8
	188 µL 10 % APS
	75 µL TEMED
10 % Separating gel	4 mL Acrylamide
	5 mL ddH_2O
	3 mL 4x Tris/HCl, pH 8.8
	48 µL 10% APS
	96 µL TEMED

5.2.6.3 Immunoblotting and immunodetection

The protein separation by SDS-PAGE is followed by immunoblotting and immunodetection to visualize proteins. First, the transfer of the proteins from the SDS-PAGE gel to a nitrocellulose membrane is done with the wet-tank method. The gel is placed on the nitrocellulose membrane between two layers of Whatman paper on each side. Outside of this sandwich was a sponge of each side. The transfer was performed in transfer chambers from BioRad with pre-cooled 1x Transfer Buffer containing 20 % methanol. An electric field with 100 V was applied for 90 min in the cold. After the transfer, the nitrocellulose membrane was incubated in 5 % milk powder in TBS-T for 30 min to reduce unspecific signals. The subsequent incubation in a primary antibody that binds to the protein of interest was performed overnight at 4°C. Primary and secondary antibodies are listed in Table 3 and Table 4.

On the next day, the nitrocellulose membrane was washed for three times in TBS-T. The secondary antibody was diluted 1:5000 in 5 % milk powder and added for 1 h. The secondary antibody detects the primary antibody in a species-specific manner. After another three-time washing step with TBS-T, the membrane was incubated with 300 µL of detection solution from SuperSignal West Pico PLUS Kit. The secondary antibody is coupled to a horseradish oxidase, which catalyzes the oxidation of luminol which can be detected by iBright 1500 gel documentation system. The relative quantification was determined by *ImageJ* and significant differences were investigated using *GraphPad Prism*.

5.2.6.4 IFN-γ ELISA

The IFN-γ secretion of cultured T cells was measured using the ELISA MAX DELUXE (Biolegend) according to the manufacturer's instructions. The pre-coated plate was washed with 300 µL ELISA wash buffer for four times before 100 µL cell culture supernatant and standards (diluted 1:1 in Assay buffer A) were added to each well and the plate incubated for 2 h at room temperature. The plate was washed afterwards followed by an 1 h incubation with 100 µL Detection Antibody solution. The plate was again washed four times before adding 100 µL Avidin-HPR solution for 30 min. Then, the final washing step with ELISA wash buffer included five steps before 100 µL Substrate Solution F was added to the wells for a 15-min incubation in the dark. Finally, the reaction was added with 100 µL Stop solution and the absorbance was measured at 450 nm and 570 nm on *FlexStation 3 Multi-Mode Microplate Reader*. The data was further analyzed using *Microsoft Excel* and *GraphPad Prism*.

5.2.7 Statistics

In this thesis, bar graphs depict data represented as mean ± standard error of the mean (SEM). For FRET experiments n is the number of cells measured. For the analysis of the PDE2A cKO mice n represents the number of mice and was used for statistical analysis with *GraphPad Prism*. The normal distribution was tested using the Kolmogorov-Smirnov test with Dallal-Wilkinson-Lille approximation. Differences between the groups were test using one-way ANOVA followed by Sidak's multiple comparison tests, Student's t-test, or a non-parametric Kruskal-Wallis test, as indicated in each figure legend. Significant differences are indicated as *$p<0.05$, **$p<0.01$, ***$p<0.001$, and ****$p<0.0001$.

6 Results

6.1 Visualization of cAMP signaling and the regulation of intracellular cAMP mediated by PDE in T cell responses after MI

6.1.1 ß-adrenergic receptor (ß-AR) signaling

MI causes tissue damage and cell death leading to the release of high levels of catecholamines which activate ß-AR on the cell surface and increase cAMP production. However, it is unknown how infiltrating T cells react to the high levels of catecholamines. To investigate this, CD4+ T cells were isolated from spleen and heart-draining lymph nodes (medLN) of cAMPFIRE-M biosensor mice at three distinct time points after MI: pro-inflammatory phase (3 days post MI, d3), inflammatory phase (7 days post MI, d7) and in the remodeling phase (8 weeks post MI, 8w). The echocardiography measurements of the hearts revealed a characteristic decrease in Ejection Fraction (EF) after MI which verified a constant infarction in the MI group compared to the Sham group at all three time points (**Figure 8**).

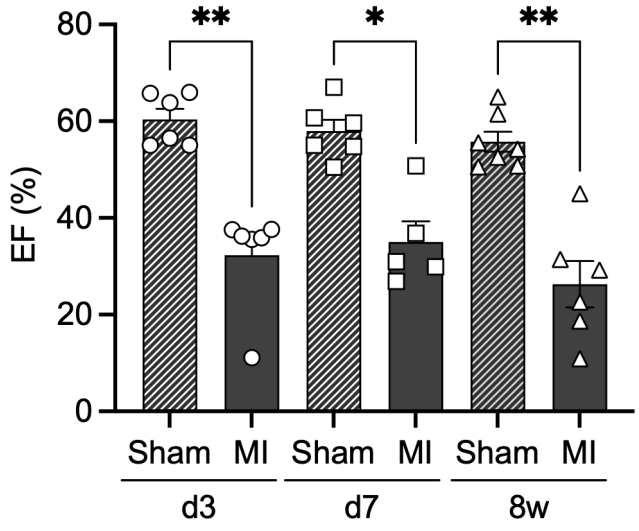


Figure 8: Verification of the Myocardial Infarction model of cAMPFIRE-M biosensor mice at day 3 (d3), day 7 (d7) and 8 weeks (8w) post MI. Ejection Fraction (EF) measured in Echocardiography. N = 5-7 mice per group. Results are shown as mean +- SEM. *p<0.05, **p<0.005 by one-way ANOVA followed by a non-parametric Kruskal-Wallis test.

The intracellular cAMP dynamics in T cells was monitored with a highly sensitive cAMP biosensor, cAMPFIRE-M, which was expressed ubiquitously in homozygous mice. MACS-sorted CD4+ T cells were cultured overnight with or without anti-CD3/anti-CD28 antibodies for T cell activation and used for FRET live-cell imaging on the next day. During the measurements, the ß-AR were stimulated with increasing concentrations of the non-selective ß-AR agonist isoproterenol (ISO; 1 nM and 10 nM). The maximal sensor response was induced by a final treatment with 10 µM Forskolin (FSK) and 100 µM IBMX. FSK stimulated the adenylyl cyclases and IBMX is a pan-PDE inhibitor. The response to ISO was quantified as % in comparison to the maximal sensor response. Representative traces from FRET measurements in non-activated T cells and the respective quantifications are depicted in **Figure 9**. At day 3, there was a trend observed in lymphatic T cells showing that ß-AR responded less to 1 nM ISO stimulation in MI mice in comparison to Sham mice, but without significant impact (p_{medLN} =0.3346). At day 7, the 1 nM ISO response was significantly reduced in T cells from medLN of MI mice (p_{medLN} = 0.0008) compared to Sham mice. In the chronic phase of cardiac remodeling (8w) the ISO-stimulated increase in cAMP production was comparable between MI and Sham groups. Interestingly, splenic T cells did not show differences to ISO treatment between MI and Sham at any time point.

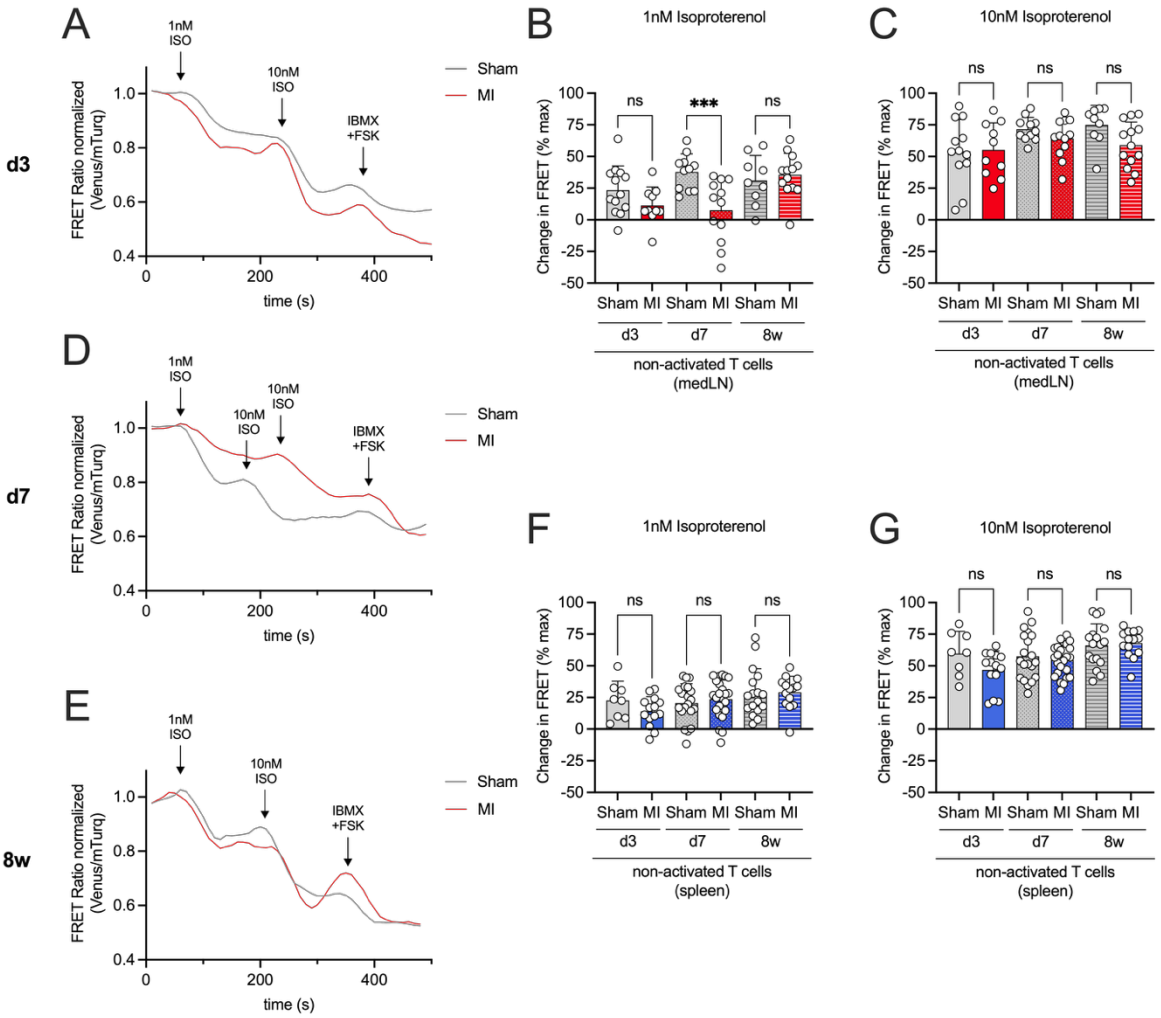


Figure 9: Stimulation of ß-AR in non-activated T cells after MI. CD4+ T cells were isolated from spleen or medLN of cAMPFIRE-M biosensor mice at different time points post MI/Sham surgery. After an overnight culture, FRET live-cell imaging was performed. Bulk CD4+ T cells were stimulated with increasing concentrations of the non-selective ß-AR agonist isoproterenol (ISO) followed by Forskolin (FSK; 10 µM) and 3-Isobutyl-1-Methylxanthine (IBMX; 100 µM). Representative FRET traces from T cells isolated from medLN on day 3 (d3) (**A**), day 7 (d7) (**D**) and 8 weeks (8w) (**E**) post MI/Sham. (**B**,**C**) Quantification of the FRET responses shown upon the stimulation of 1 nM (**B**) and 10 nM ISO (**C**) in percentage to the maximal FRET response. (**E**,**G**) Quantification of the FRET responses to 1 nM (**F**) and 10 nM (**G**) ISO in splenic T cells. Results are shown as mean +- SEM. ***p<0.001, ns–not significant by one-way ANOVA followed by Sidak's multiple comparison test.

In vivo, T cells driving the disease are activated T cells, which may return to a resting state during the overnight culture. Thus, the experimental setup was repeated in *in vitro* activated CD4+ T cells after anti-CD3/anti-CD28 antibody culture to mimic the *in vivo* situation. This approach determines whether disease-associated alterations are maintained in activated T cells. Representative FRET traces and quantification of

FRET responses to ISO stimulation are shown in **Figure 10**. Interestingly, activated CD4+ T cells from MI mice showed a reduction on d3 post MI ($p_{medLN,NA}$= 0.0426; $p_{medLN,A}$= 0.0128), but unlike non-activated T cells, activated T cells displayed no significant differences in ß-AR responsiveness between Sham and MI mice on d7. T cells isolated from the spleen did not show significant alterations after MI in any stage of the disease.

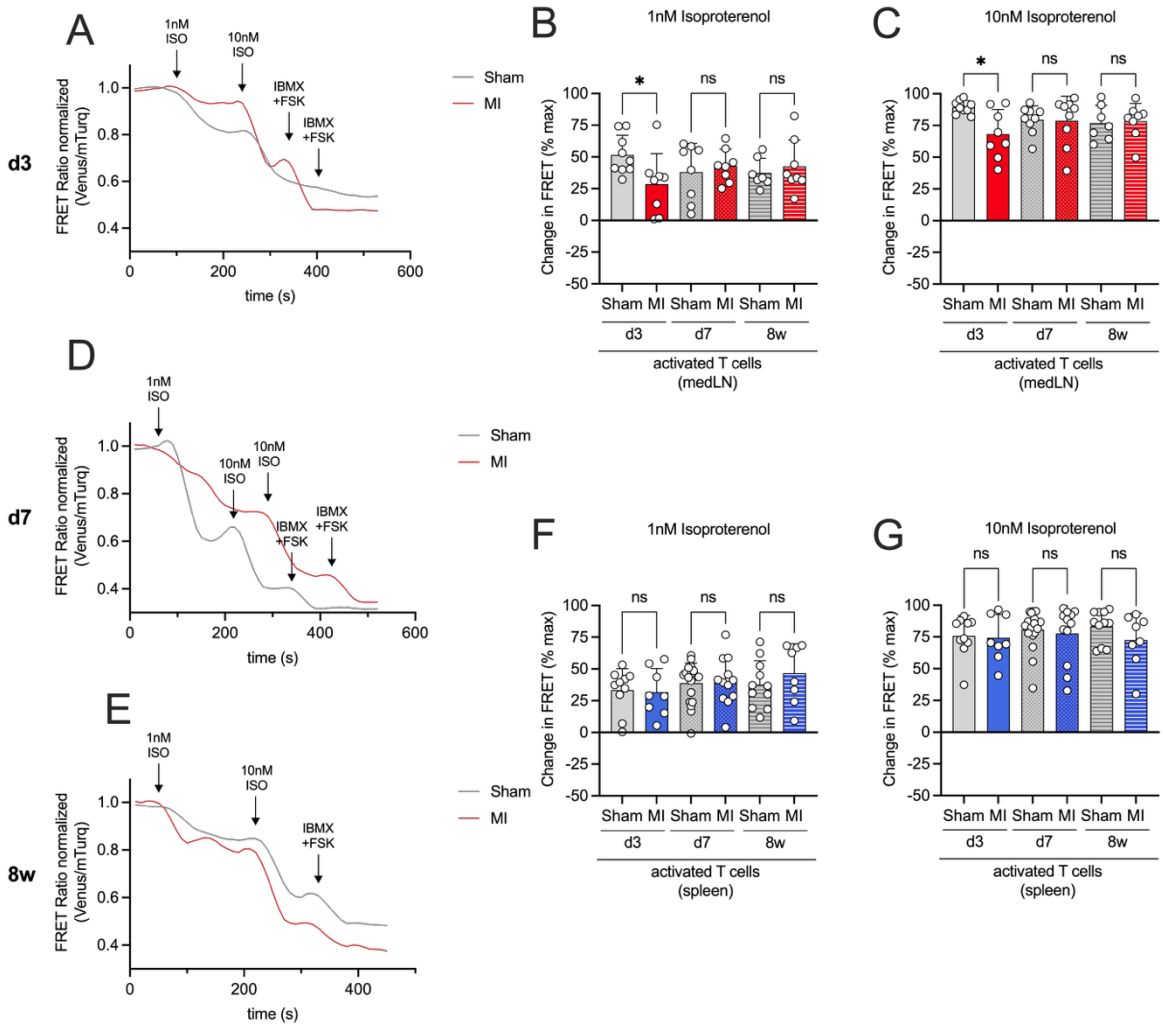


Figure 10: ß-AR stimulation in *in vitro* activated CD4+ T cells after MI. Bulk CD4+ T cells were isolated from medLN and spleen from transgenic cAMPFIRE mice on d3, d7 and 8w post MI/Sham and cultured overnight with anti-CD3/anti-CD28 antibodies. FRET measurements were performed on the next day. To test ß-AR receptor sensitivity cells were treated with 1 nM and 10 nM isoproterenol (ISO). The change in FRET was quantified in comparison to the sensor saturation induced by Forskolin (FSK; 10 µM) and 3-Isobutyl-1-Methylxanthine (IBMX; 100 µM). Representative traces show FRET measurements of lymphatic activated T cells 3d (**A**), 7d (**D**) and 8w (**E**) after MI/Sham. The quantification of these traces is shown in (**B**) and (**C**). (**F,G**) Quantification of the response upon ISO stimulation in splenic CD4+ cells. Bar graphs are shown as mean

± SEM. *p<0.05, ns–not significant by one-way ANOVA followed by Sidak's multiple comparison test or a non-parametric Kruskal-Wallis test.

Cardiomyocytes are known for its desensitization of the ß-AR during heart failure development. To be able to compare effects observed in T cells to the effects reported for cardiomyocytes, also cardiomyocytes were isolated from cAMPFIRE-M biosensor mice and the responsiveness of their ß-AR to ISO stimulation were tested with FRET live-cell imaging on the same day of the isolation. The cells were pre-incubated with ICI-118551 to block $ß_2$-AR and stimulated with 3 nM and 100 nM ISO and a finally with 100 µM IBMX/10 µM FSK to saturate the FRET sensor. The results are depicted in **Figure 11**. The analysis revealed that $ß_1$-AR desensitize only on d7, but not on d3 or 8w post MI (p_{d7}= 0.0424).

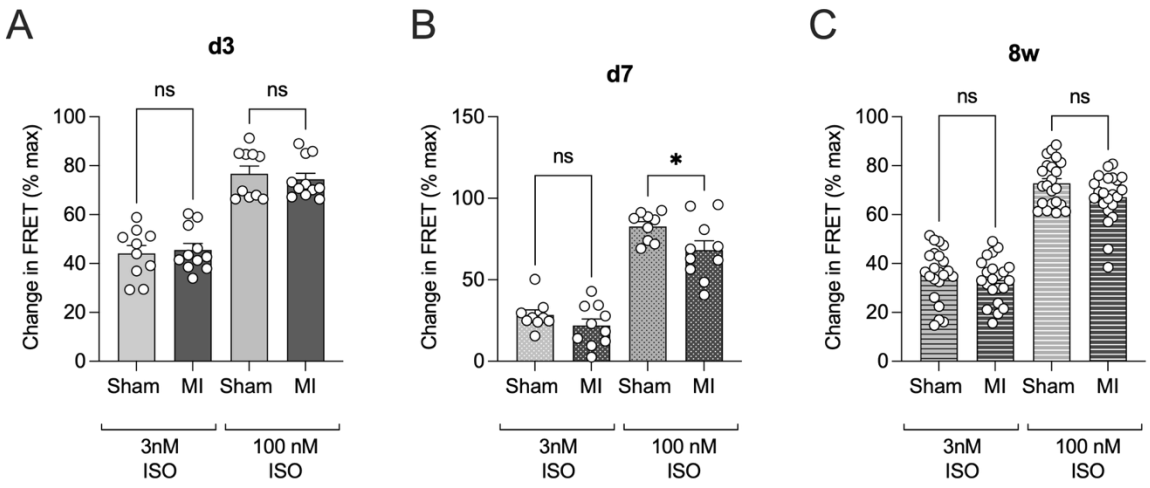


Figure 11: Real-time measurements of FRET responses in cardiomyocytes after MI upon isoproterenol (ISO) treatment. Cardiomyocytes were isolated from cAMPFIRE-M biosensor mice (**A**) 3 days (d3), (**B**) 7 days (d7) and (**C**) 8 weeks (8w) post MI/Sham surgery. The sensitivity of ß-AR to low (3 nM) and high concentration (100 nM) isoproterenol (ISO) stimulation was measured in FRET live-cell imaging in the presence of ICI-118551, a $ß_2$-AR inhibitor. The maximal response was induced by a final Forskolin and IBMX treatment and the response to isoproterenol was quantified as the Change in FRET in % to the maximal response. Bar graphs are shown as mean ± SEM. *p<0.05, ns–not significant by one-way ANOVA followed by Sidak's multiple comparison test.

6.1.2 $A_{2A}R$ signaling

Another important example of a G_s-coupled GPCR is the adenosine receptor, in T cells predominantly the $A_{2A}R$. Like ß-AR, $A_{2A}R$ mediate immunosuppressive responses via

cAMP-mediated pathways. However, unlike the systemic release of catecholamines triggering ß-AR, the A_{2A} receptor ligand ADO is a purinergic signaling molecule locally released in inflamed tissue. Therefore, comparing the ß-AR to the A_{2A}R should reveal whether the adrenergic and purinergic signaling pathways differentially modulate T cell responses after MI. In this experimental setup, the A_{2A}R on CD4+ T cells from medLN were stimulated by the specific agonist 5'-Ethylcarboxamidodenosine (NECA) and changes in cAMP levels were monitored via FRET live-cell imaging (**Figure 12**). The treatment with NECA (10 nM and 100 nM) resulted in a concentration-dependent increase in cAMP production. The cAMPFIRE-M sensor was saturated by 10 µM FSK and 100 µM IBMX at the end of each measurement. A comparison between T cells isolated from Sham mice to T cells isolated from MI mice revealed no significant changes at any timepoint during the disease progression.

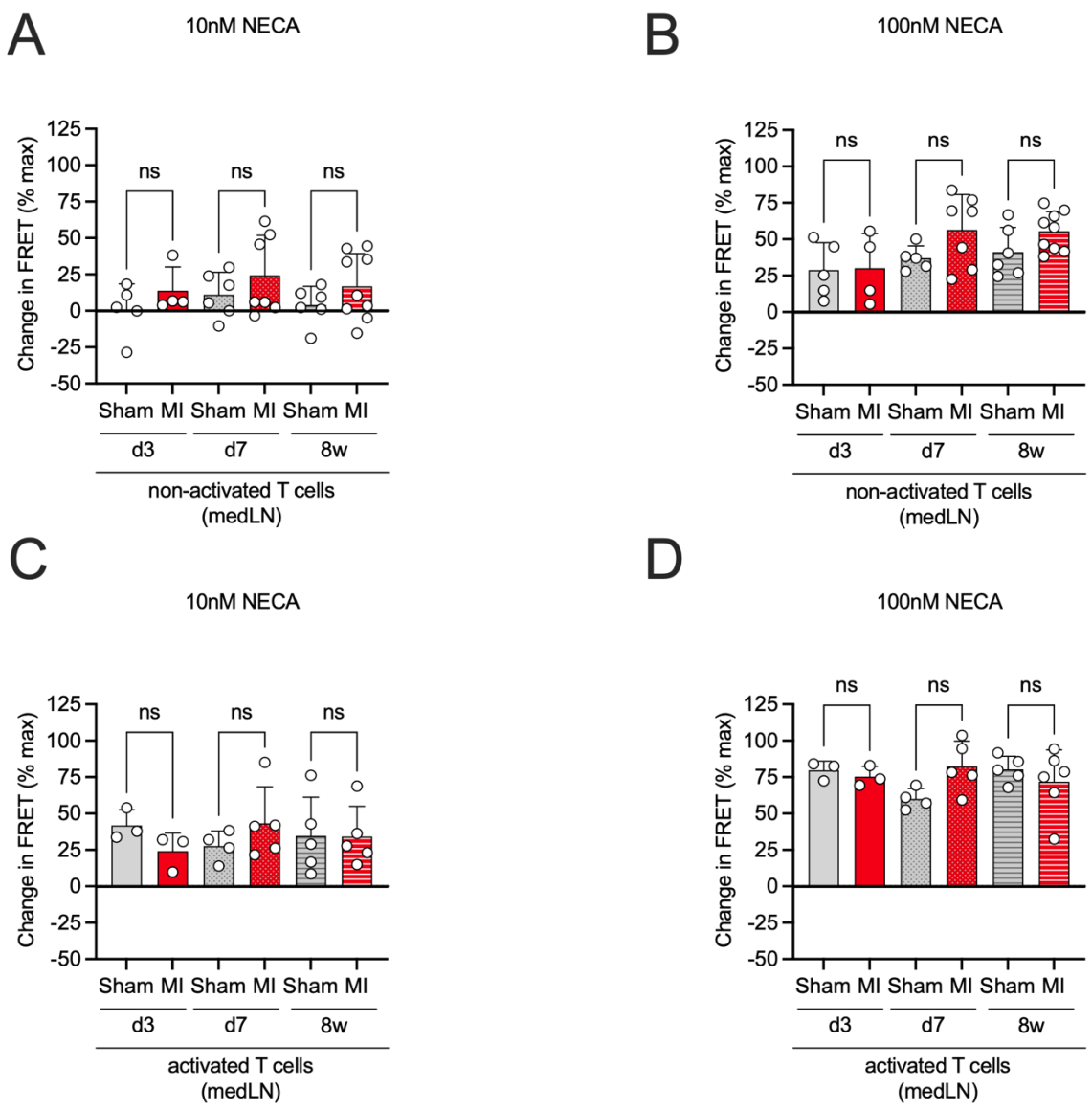


Figure 12: $A_{2A}R$ stimulation in non-activated and *in vitro* activated T cells after MI. MACS-sorted T cells from medLN were cultured overnight with and without anti-CD3 and anti-CD28 antibodies. In FRET measurements cells were stimulated with increasing concentrations of $A_{2A}R$ agonist NECA in increasing concentrations (10 nM; 100 nM). The cAMPFIRE-M biosensor was saturated with Forskolin (FSK, 10 µM) and 3-Isobutyl-1-Methylxanthine (IBMX; 100 µM) to quantify the change in FRET as % of max response. (**A**,**B**) Change in FRET upon treatment with 10 nM (**A**) and 100nM (**B**) NECA in non-activated T cells. (**C**,**D**) Change in FRET upon treatment with 10 nM (**C**) and 100nM (**D**) NECA in *in vitro* activated T cells. Bar graphs are shown as mean ± SEM. ns–not significant by one-way ANOVA followed by Sidak's multiple comparison test or Kruskal-Wallis test.

6.1.3 Phosphodiesterases are in charge of balance intracellular cAMP

Different G_s-coupled GPCRs initiate cAMP production via AC. However, the cellular response is tightly controlled by the balance between cAMP synthesis and degradation

mediated by PDE. As described in the previous section, the ß-AR adapt to the constant catecholamine stimulation in CD4+ T cells after MI. Therefore, studying the PDE expression and activity in this context will provide a better understanding of how T cell function is regulated after MI.

6.1.3.1 PDE2 in T cells after MI

Beyond the increase of catecholamines, MI also leads to the release of ANP and BNP which enhance cGMP production, the unique dual-substrate enzyme PDE2A represents a good candidate to study in the context of T cell activity after MI. To address this question, FRET live-cell measurements were performed in the presence of a PDE2A-specific inhibitor BAY-60-7550. CD4+ T cells were isolated from medLN and spleen via MACS sorting, cultured overnight either with or without anti-CD3/anti-CD28 antibodies for *in vitro* activation and analyzed in real-time measurements on the next day. The cells were prestimulated with either 10 nM ISO (non-activated T cells) or 1 nM ISO (activated T cells), then PDE2A activity was inhibited by 100 nM BAY-60-7550. Finally, the cAMPFIRE-M biosensor was saturated with 10 µM FSK and 100 µM IBMX to allow the quantification as % of the maximal response (**Figure 13**). The analysis of non-activated and activated T cells from both organs revealed comparable results for PDE2A inhibition by BAY-60-7550 between T cells isolated from Sham and MI mice. These findings indicate that other PDE family members may be more critical in this context.

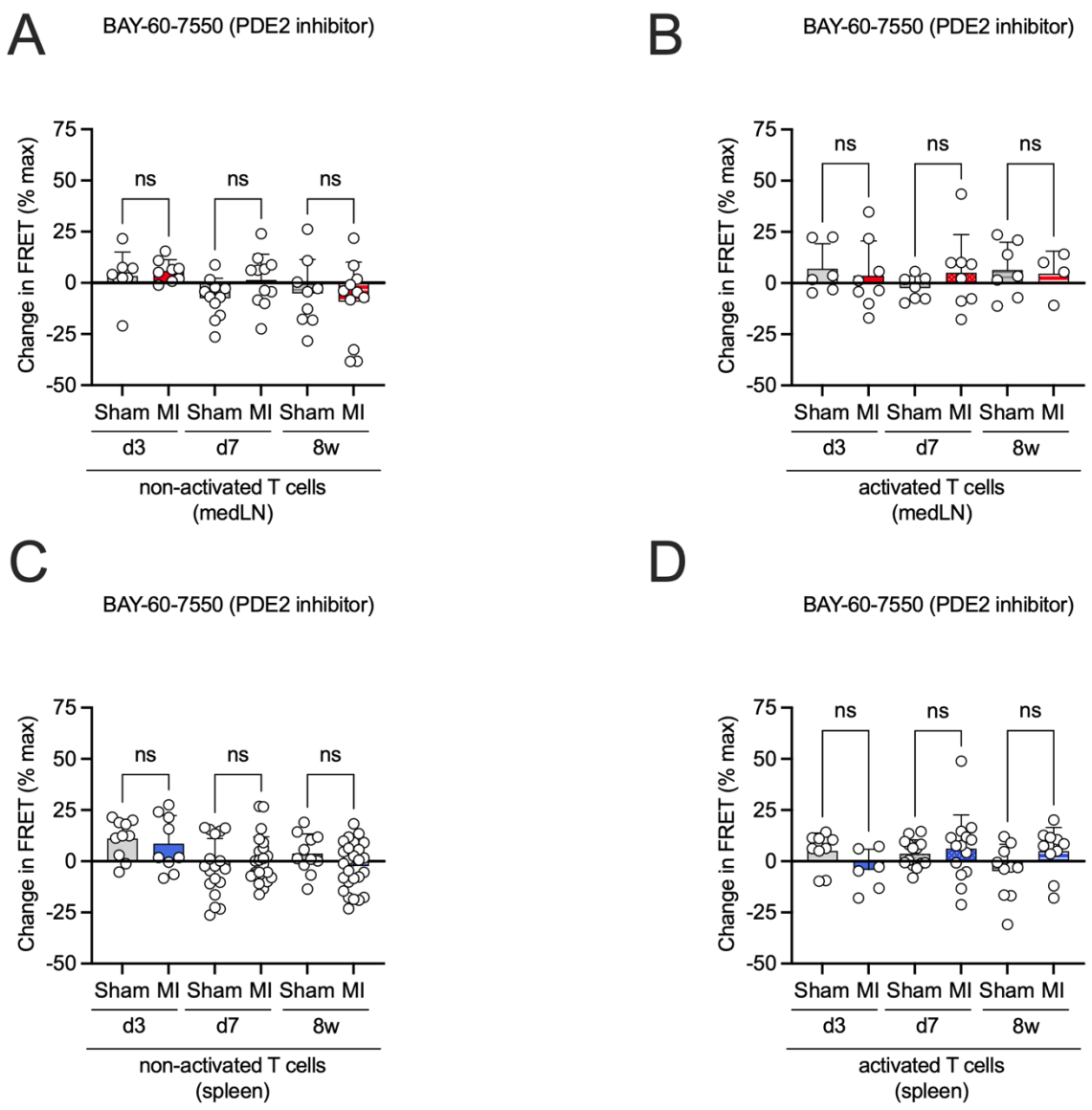


Figure 13: FRET measurements in CD4+ T cells expressing cAMPFIRE-M upon PDE2A inhibition. CD4+ T cells were isolated from medLN (**A**,**B**) and spleen (**C,D**) from cAMPFIRE-M biosensor mice at three distinct timepoints after MI/Sham. Half of the T cell population was cultured overnight with anti-CD3/CD28 antibodies for *in vitro* activation (**B**,**D**). cAMP dynamics were monitored via FRET live-cell imaging. T cells were prestimulated with 10 nM (non-activated) and 1 nM (activated) isoproterenol (ISO) before the treatment with the PDE2A-specific inhibitor BAY-60-7550 (100nM). After a stable baseline, the sensor was saturated with Forskolin (10 µM; FSK) and 3-Isobutyl-1-Methylxanthine (100 µM; IBMX). The change in FRET after PDE2A inhibition is quantified as the % of the maximal response of the sensor and depicted in bar graphs as mean ± SEM. Negative values are caused by a decrease in cAMP levels during the measurements. ns–not significant by one-way ANOVA followed by Sidak's multiple comparison test or Kruskal-Wallis test.

6.1.3.2 PDE3 in T cells after MI

To determine whether predominant isoform PDE3B contributes to the regulation of T cell function after MI, the same experimental approach was applied using the PDE3 specific inhibitor Cilostamide (CILO). During FRET live-cell measurements, CD4+ T cells were first treated with 10 nM or 1 nM ISO to enhance intracellular cAMP levels and then with 10 µM CILO to inhibit PDE3B. A final treatment with 10 µM Forskolin and 100 µM IBMX was used to determine the maximal response of the sensor. The impact of PDE3 inhibition is shown as percentage in comparison to the maximal response (**Figure 14**). However, analyzing bulk CD4+ T cells in non-activated and activated state revealed no significant differences in PDE3B inhibition between MI and Sham mice at any time point of the inflammatory response.

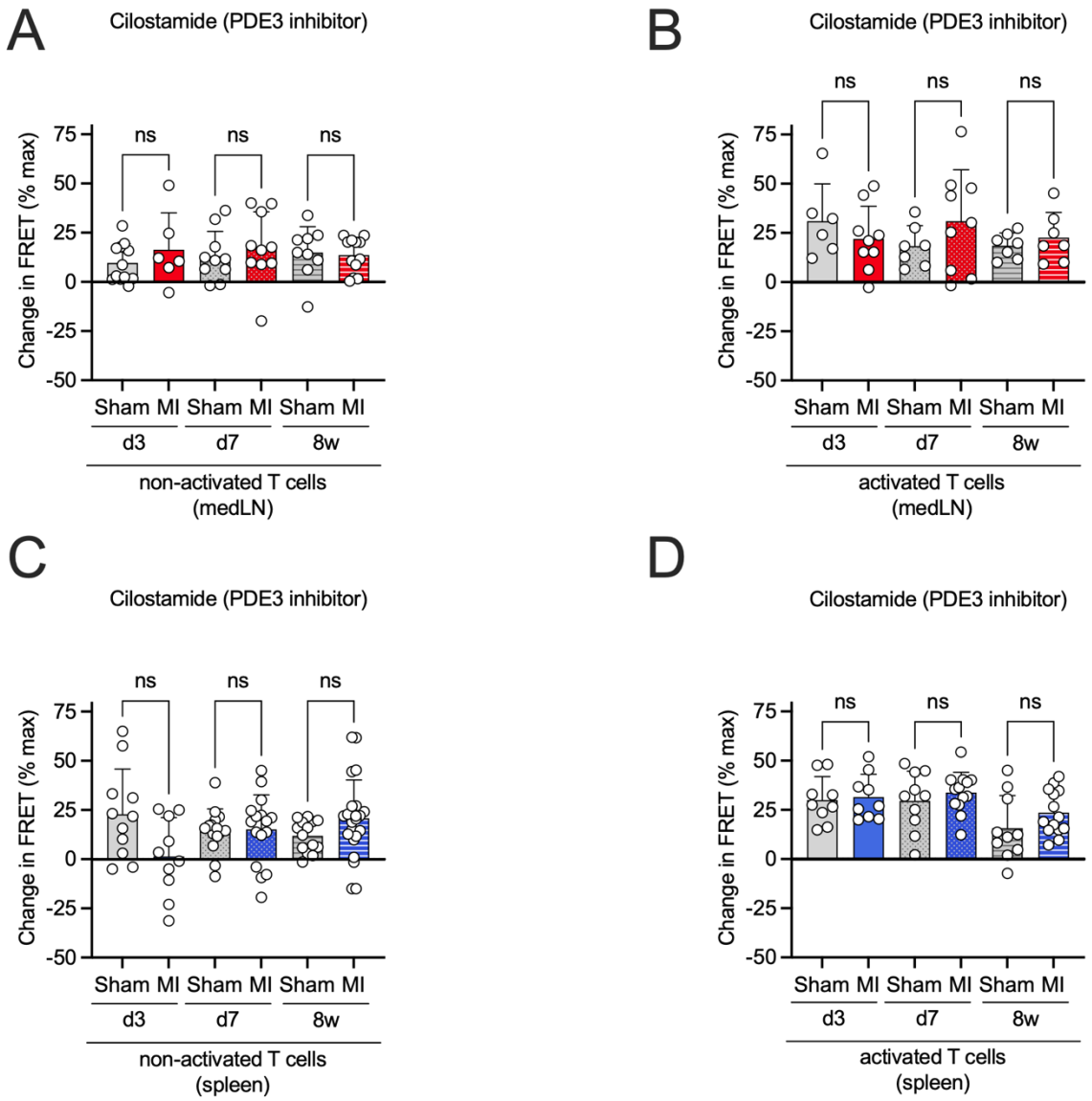


Figure 14: PDE3 inhibition during FRET live-cell measurements in CD4+ T cells. cAMPFIRE-M biosensor mice underwent MI/Sham surgery and CD4+ T cells were isolated at three timepoints post-surgery from medLN (**A**,**B**) and spleen (**C**,**D**) and cultured overnight with (activated) and without (non-activated) anti-CD3/anti-CD28 antibodies. On the next day, FRET measurements were performed to analyze cAMP signaling. T cells were treated first with 10 nM (non-activated) and 1 nM (activated) isoproterenol (ISO), second with the PDE3-specific drug 10 µM cilostamide (CILO) and lastly with 10 µM Forskolin (FSK)/ 100 µM 3-Isobutyl-1-Methylxanthine (IBMX). The impact of PDE3 inhibition is shown as percentage of the maximal response and visualized in bar graphs as mean ± SEM. ns–not significant by one-way ANOVA followed by Sidak's multiple comparison test or Kruskal-Wallis test.

6.1.3.3 PDE4 in T cells after MI

Pharmacological inhibition of PDE4, the predominant PDE in T lymphocytes, demonstrates an anti-inflammatory effect in autoimmune diseases. Nevertheless, the contribution of PDE4 in the T cell response after MI remains unexplored. To address this gap, the role of PDE4 was investigated in murine CD4+ T cells during FRET real-time measurements using the PDE4 inhibitor Rolipram (ROLI). Following the previous strategy, MACS-sorted CD4+ T cells isolated from MI or Sham mice were prestimulated with 10 nM/ 1 nM ISO before the treatment with 10 µM ROLI and a final stimulation with 10 µM FSK/100 µM IBMX. The analysis of (non-)activated CD4+ T cells from medLN and spleen indeed revealed a significant alteration in the PDE4 inhibition. While the acute inflammatory response (d3 and d7) due to the myocardial injury did not affect PDE4 activity, in the chronic heart failure progression (8 weeks post MI) CD4+ T cells showed an increase the FRET change after ROLI treatment by 2-fold (p_{medLN} = 0.0497; p_{spleen} = 0.0418). This effect was visible in activated T cells isolated from the medLN and non-activated T cells isolated from the spleen.

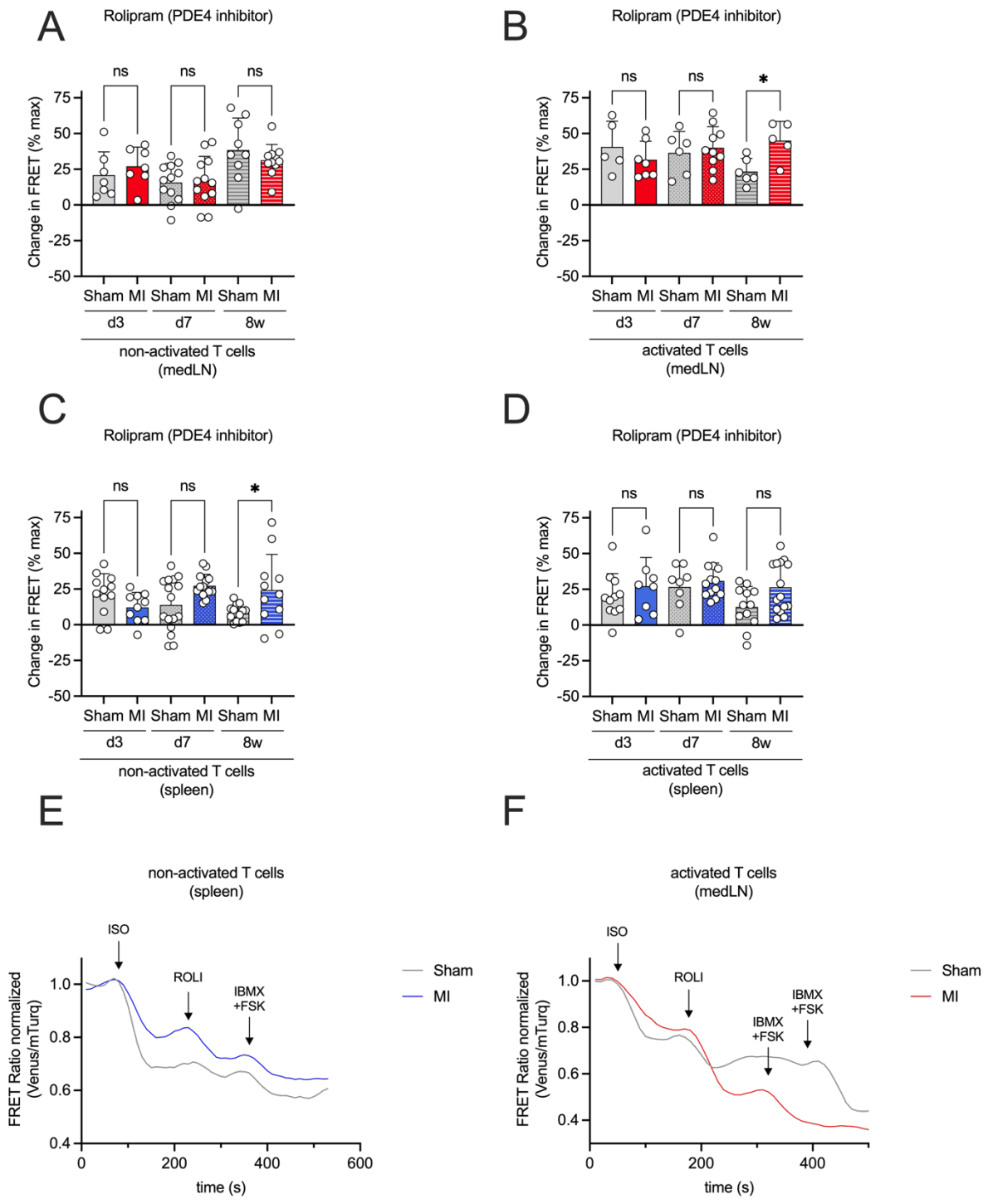


Figure 15: PDE4 inhibition in CD4+ T cells expressing cAMPFIRE-M biosensor. Murine T cells were MACS-purified from medLN and spleen 3 days (d3), 7 days (d7) and 8 weeks (8w) post MI or Sham surgery. T cells were cultured overnight in two conditions: non-activated or activated with anti-CD3/anti-CD28 antibodies. On the next day cAMP dynamic was analyzed in FRET measurements. CD4+ T cells were stimulated with 10 nM/ 1 nM isoproterenol (ISO) before the treatment with the PDE4 specific inhibitor 10 µM Rolipram (ROLI) and a final stimulation with 10 µM Forskolin (FSK)/100 µM IBMX. (**A**-**D**) Quantification of the FRET response to PDE4 inhibition via ROLI in comparison to the maximal sensor response (% of max) and depicted in bar graphs as mean ± SEM. Representative traces of FRET measurements 8w post MI in

non-activated splenic T cells (**E**) and activated lymphatic T cells (**F**). *p<0.05, ns–not significant by one-way ANOVA followed by Sidak's multiple comparison test.

6.1.3.4 PDE8 in T cells after MI

PDE8 controls T cell chemotaxis by modulating cAMP gradients and regulates integrin-mediated adhesion necessary for T cell infiltration into inflamed tissue like the myocardium after MI (Basole et al., 2017). Thus, the contribution of PDE8 to the T cell regulation was examined across the inflammatory response due to MI. FRET live-cell measurements were performed in murine CD4+ T cells expressing cAMPFIRE-M isolated from medLN and spleen at three distinct time points post MI. After the ISO-mediated increase of intracellular cAMP, PDE8 was inhibited via PF-04957325 treatment. The biosensor was saturated by 10 µM FSK/100 µM IBMX stimulation to quantify the inhibitory response in relation to the maximal response (% of max). Representative traces and the respective quantification are shown in **Figure 16**. The analysis of the pro-inflammatory response d3 revealed a higher response to PDE8 inhibition in T cells from both organs after MI surgery in comparison to Sham mice (p_{medLN}=0.0323; p_{spleen}=0.0099). Interestingly, comparable levels were detected in MI vs. MI T cells for the time point d7, shortly after the T cell peak in the heart, or for 8w, the chronic heart remodeling phase.

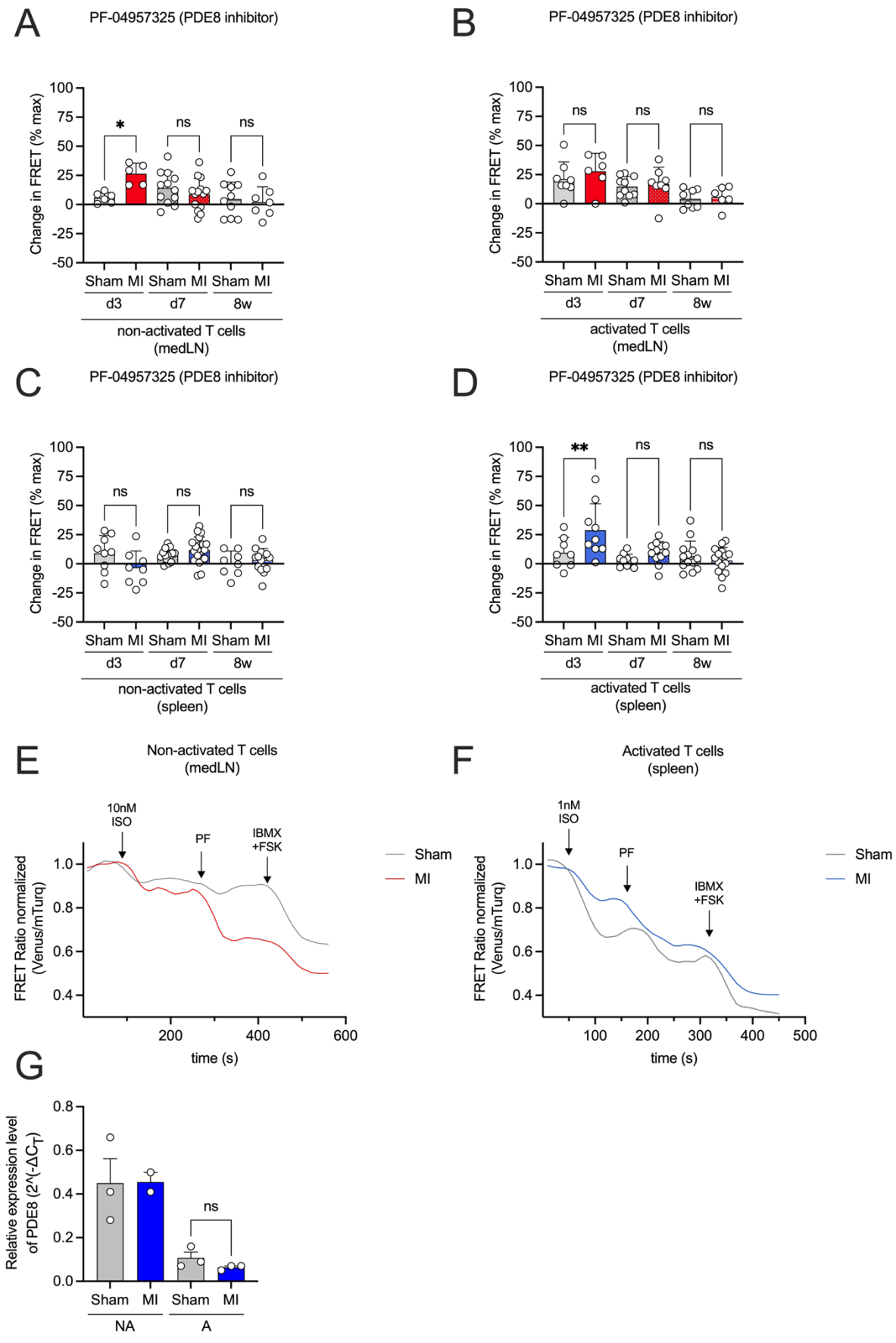


Figure 16: MI affects PDE8 response in T cells at the early stage of T cell infiltration. Murine CD4+ T cells from spleen and medLN from cAMPFIRE-M

biosensor mice were analyzed 3 days (d3), 7 days (d7) and 8 weeks post Myocardial Infarction or Sham surgery. T cells were isolated via MACS sorting and cultured overnight, either with (activated) or without (non-activated) anti-CD3/anti-CD28 antibodies before FRET measurements. After a pre-stimulation with isoproterenol (ISO), PDE8 was inhibited with 1 µM PF-04957325 (PF) followed by saturation with Forskolin (FSK, 10 µM)/ IBMX (100 µM). The response to PDE8 inhibition is shown as % of the change in FRET in relation to the maximal sensor response in bar graphs (mean ± SEM). ***p<0.001, ns–not significant by one-way ANOVA followed by Sidak's multiple comparison test or Kruskal-Wallis test.

6.1.4 Summary

The aim of the first subsection was to investigate the effects of ß-AR signaling and intracellular cAMP dynamics in T cells across different time points of the inflammatory response after MI. This was achieved by various FRET live-cell measurements with either stimulating ß-AR or $A_{2A}R$ leading to cAMP production or inhibiting PDE-mediated cAMP degradation with specific inhibitors. Firstly, the ß-AR is de-sensitized due to the sympathetic overdrive at d3 in activated and on d7 non-activated T cells from the medLN, but not in splenic T cells. In contrast, the response of $A_{2A}R$ to its stimulus was constant in T cells from MI and Sham mice during the disease progression. Secondly, among the PDE examined PDE4 and PDE8 showed significant alterations in chronic heart failure (8w) and at the early onset of T cell infiltration (d3), respectively. The response to PDE2A and PDE3B inhibition was comparable in all stages of the disease.

6.2 The role of PDE2A as a regulator of the cAMP-to-cGMP cross-talk in T cell responses after MI

High levels of catecholamines activate ß-AR after MI, which was investigated in **6.1**. On the other hand, the post-myocardial milieu is also shaped by high levels of NPs which activate cGMP production. Taken together with the observation that the cGMP-activated cAMP-degrading PDE, PDE2A, is upregulated differentially in T cells upon T cell activation, PDE2A became a potential candidate for modulation of T cell function after MI. To investigate this, a PDE2A conditional Knock-Out (cKO) was induced in murine CD4+ T cells *in vivo* using the Cre-lox-system (described in **5.2.1.3**).

6.2.1 Myocardial infarction mouse model

PDE2A cKO mice and age-matched littermate controls expressing cre (Ctrl) were subjected to MI or Sham surgery. Mice of both genders were used equally in all groups (n=6-7 mice per group). As crucial parameters for heart failure progression, infarct size, left ventricular (LV) mass and lung weight in relation to the tibia length were determined (**Figure 17**). The infarct size was comparable between Ctrl and cKO mice (**Figure 17 B**). The LV mass/tibia length ratio increased equally due to MI in both groups (p_{Ctrl}=0.0223; p_{KO}= 0.0259) (**Figure 17 C**). Notably, only PDE2A cKO mice showed increased lung weight/tibia length ratio in comparison to Ctrl MI mice (p_{MI}= 0.0333) (**Figure 17 D**).

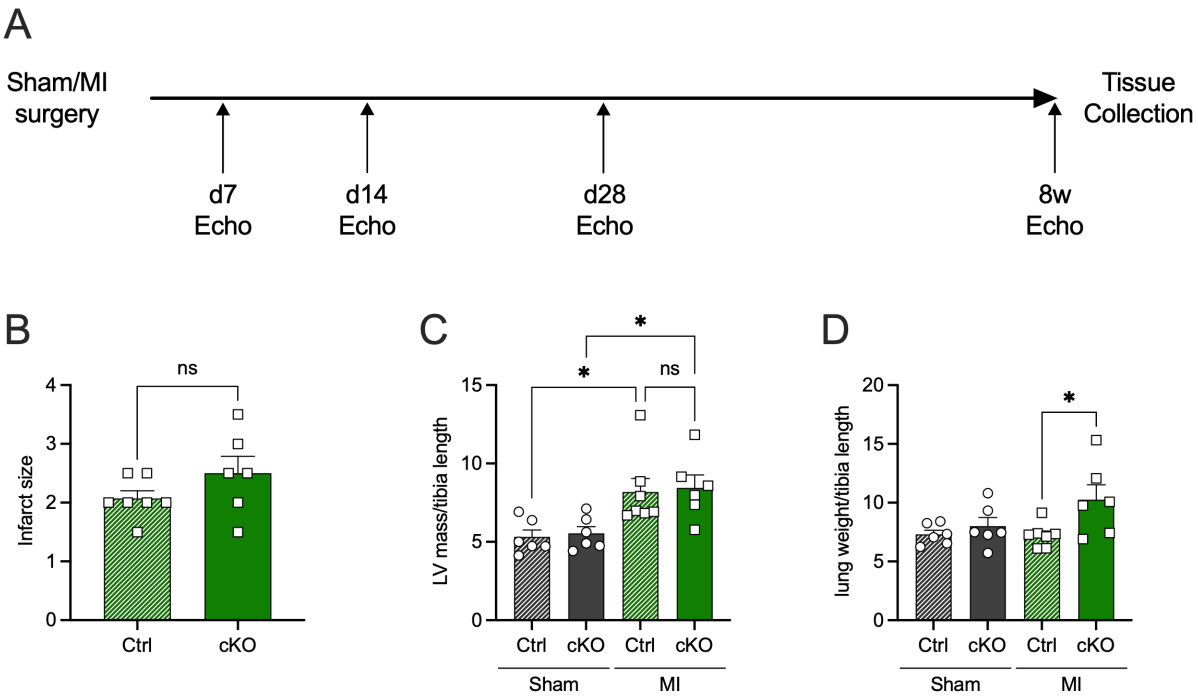


Figure 17: Infarct size, LV mass and lung weight in Ctrl and PDE2A cKO mice 8 weeks post MI. **(A)** Schematic overview of the experimental procedure. **(B)** Infarct size of Ctrl and PDE2A cKO mice. **(C)** Left ventricular (LV) mass in relation to tibia length calculated in echocardiography. **(D)** Lung weight in relation to tibia length. Bar graphs show mean ± SEM. *p<0.05, ns–not significant by Student's t test or one-way ANOVA followed by Sidak's multiple comparison test.

As shown in **Figure 17 A**, the cardiac function was monitored via echocardiography measurements over a time course of 8 weeks post MI/Sham surgery and the results are depicted in **Figure 18**.

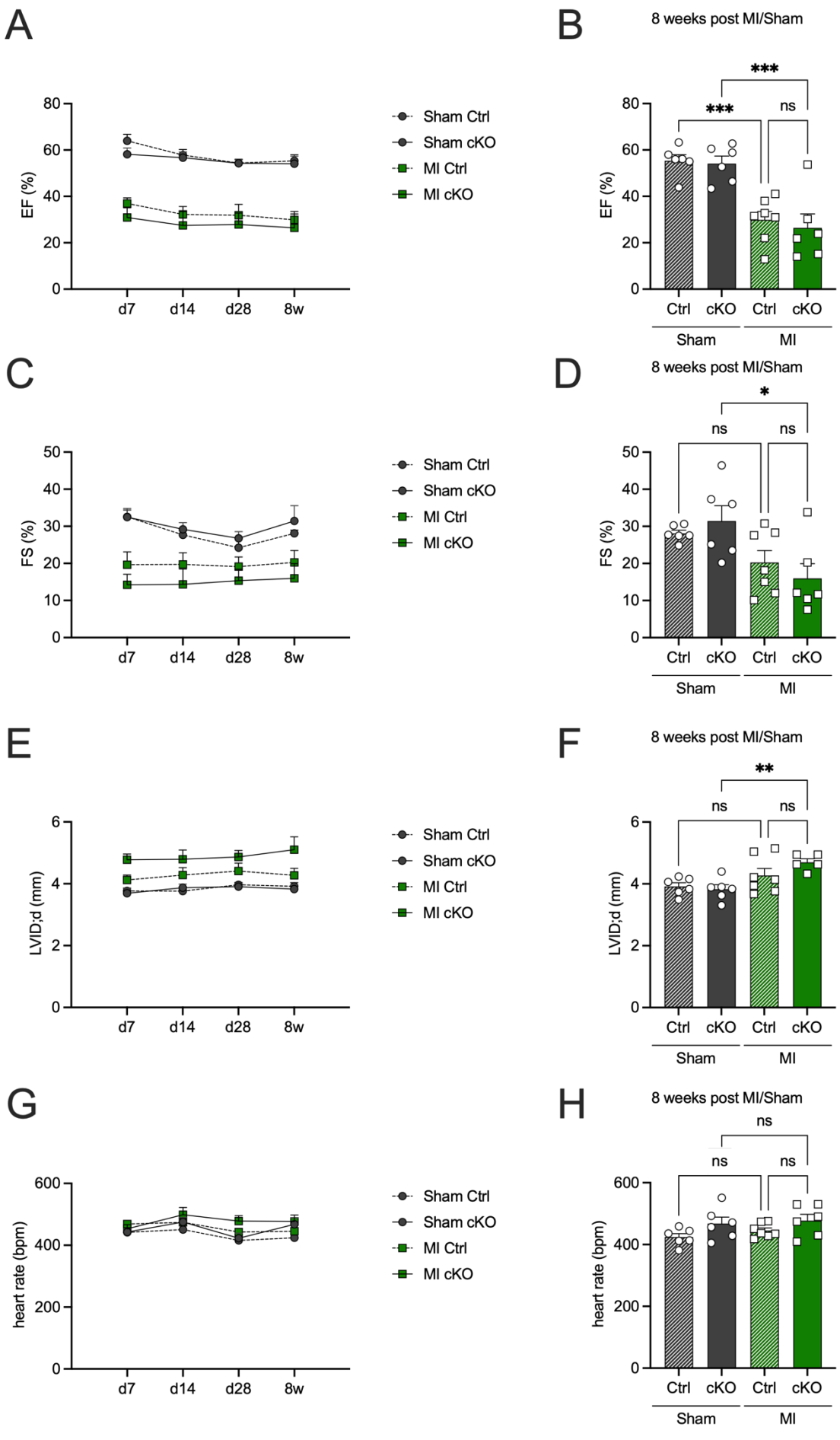

A
EF (%)
d7
d14
d28
8w
Sham Ctrl
Sham cKO
MI Ctrl
MI cKO
B
8 weeks post MI/Sham
***
***
ns
EF (%)
Ctrl
cKO
Ctrl
cKO
Sham
MI
C
FS (%)
D
8 weeks post MI/Sham
*
ns
ns
E
LVID;d (mm)
F
8 weeks post MI/Sham
**
ns
ns
G
heart rate (bpm)
H
8 weeks post MI/Sham
ns
ns
ns

Figure 18: Cardiac function of PDE2A cKO and Ctrl mice. Cardiac function of PDE2A cKO and their control littermates (Ctrl) after MI was investigated by echocardiography over a time course of 8 weeks. (**A,B)** Ejection Fraction (EF) in percentage (**C,D)** fractional shortening (FS) in percentage (**E,F)** diastolic left ventricular internal diameter (LVID;d) and (**G,H)** the heart rate were determined. Data represented as mean values ± SEM. N = 6-7 animals per group. ***p<0.001, **p<0.005, *p<0.05, ns–not significant by one-way ANOVA followed by Sidak's multiple comparison test.

The heart rate did not vary significantly between the groups during the echocardiography measurements (**Figure 18 G,H**). Analysis of the Ejection Fraction (EF) (**Figure 18 A,B**) revealed a significant reduction after MI compared to the respective Sham mice for both genotypes, but no difference between the groups ($p_{EF,Ctrl}$=0.0005; $P_{EF,KO}$=0.003; P_{MI}=0.9078). The effect was noted at d7 and further decreased over time. Fractional shortening (FS) was also reduced due to MI in PDE2A cKO mice ($p_{FS,Ctrl}$=0.2800; $P_{FS,KO}$=0.0118) (**Figure 18 C,D**). Interestingly, the diastolic left ventricular internal diameter (LVID) measured in SAX M-mode is significantly increased exclusively in the PDE2A cKO and increased over time ($P_{LVID,KO}$=0.0071) pointing towards a more pronounced HF development (**Figure 18 E,F**).

Echocardiography measurements allowed the determination of wall thickness in the left ventricle as another readout of the heart failure development. The left ventricular anterior and posterior wall thickness (LVAW/LVPW) were determined in diastole (**Figure 19**)**.** The analysis revealed no significant alterations due to the cKO of PDE2A nor due to MI.

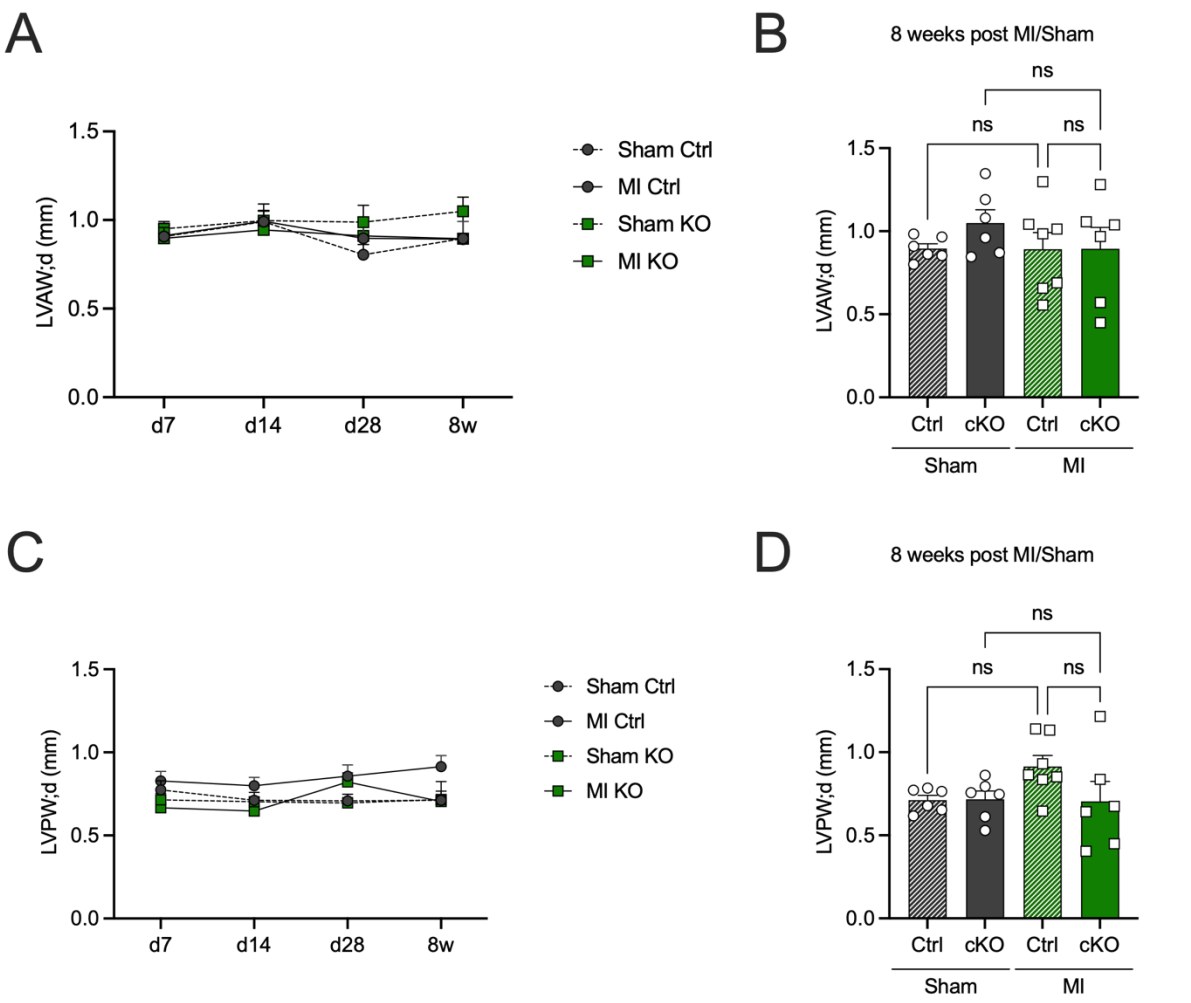


Figure 19: Determination of left ventricular anterior and posterior wall thickness (LVAW/LVPW) in PDE2A cKO and Ctrl mice. Echocardiography measurements were analyzed in SAX M-mode. **(A,B)** Left ventricular anterior wall (LVAW) in diastole (mm) during the time progression (**A**) and at 8 weeks post MI (**B**). **(C,D)** Left ventricular posterior wall (LVPW) in diastole (mm) during the time progression (**C**) and at 8 weeks post MI (**D**). Data represented as mean values ± SEM. n= 6-7 animals per group. ns– not significant by one-way ANOVA followed by Sidak's multiple comparison test.

6.2.2 Cardiac hypertrophy

Based on the observation that the LV mass was increased after MI, which is a marker for hypertrophy, potential differences between both genotypes were further elucidated by measuring the cardiomyocyte size. Cross-sections of the heart were stained with Wheat-Germ Agglutinin (WGA) to visualize cell membranes which allowed the subsequent determination of cardiomyocyte area (**Figure 20**). The hearts from PDE2A cKO and its respective Ctrl mice showed a significant increase in cell size within the left ventricle after MI (p_{Ctrl}=0.0148; p_{KO}= 0.0005). The PDE2A cKO mice showed a trend for larger cardiomyocytes, but without significant impact (p_{MI}= 0.0973).

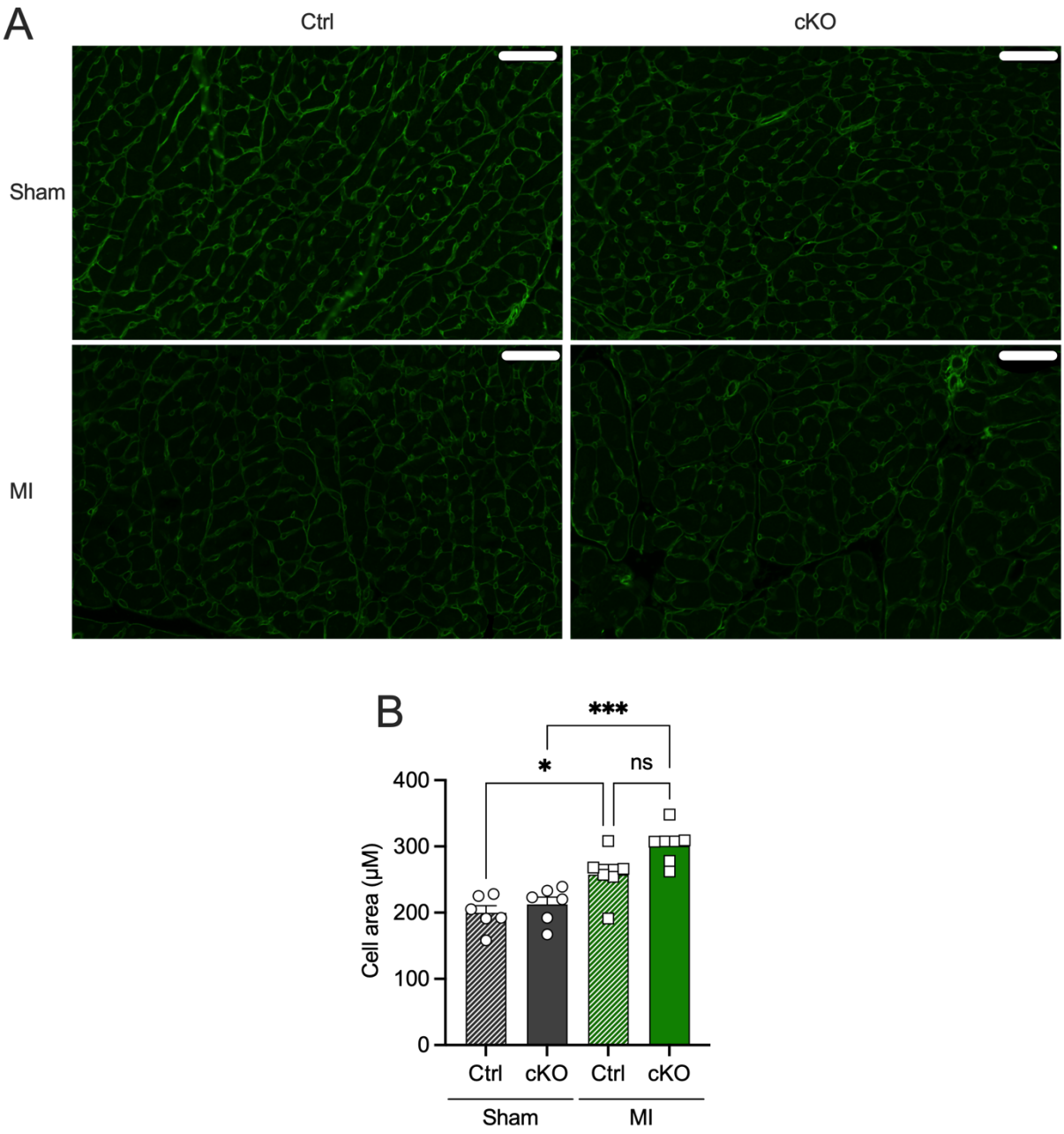


Figure 20: Histological analysis of the impact of the PDE2A dependent loss on hypertrophy development after MI. (**A**) Representative images of Wheat germ agglutinin staining in cross-section of the hearts from Sham Ctrl, Sham PDE2A cKO, MI Ctrl and MI PDE2A cKO mice 8 weeks post MI. Scale bar = 50 µM. (**B**) Quantification of Cardiomyocyte cell area. Cardiomyocytes were analyzed in 2 areas of the left ventricle. n= 4-8 mice per group. Data is shown in bar graphs (mean ± SEM). *p<0.05, **p<0.01, ns–not significant by one-way ANOVA followed by Sidak's multiple comparison test.

6.2.3 Fibrosis

As mentioned earlier, one key function during the healing process is the contribution of immune cells to a functional scar formation and controlling fibrosis. To address the question whether the loss of PDE2A in T cells alters fibrosis, Picrosirius-Red (PSR) staining was performed on heart sections from PDE2A cKO and Ctrl mice 8 weeks post MI. PSR visualized collagen fibers in red within the left ventricular tissue. Representative images and the quantification of collagen fibers are depicted in **Figure 21**. 8w post MI, the collagen content was increased after MI (p_{Ctrl}=0.0033; p_{KO}=0.0135) but is unaffected by the loss of PDE2A in T cells (p_{MI}=0.7770).

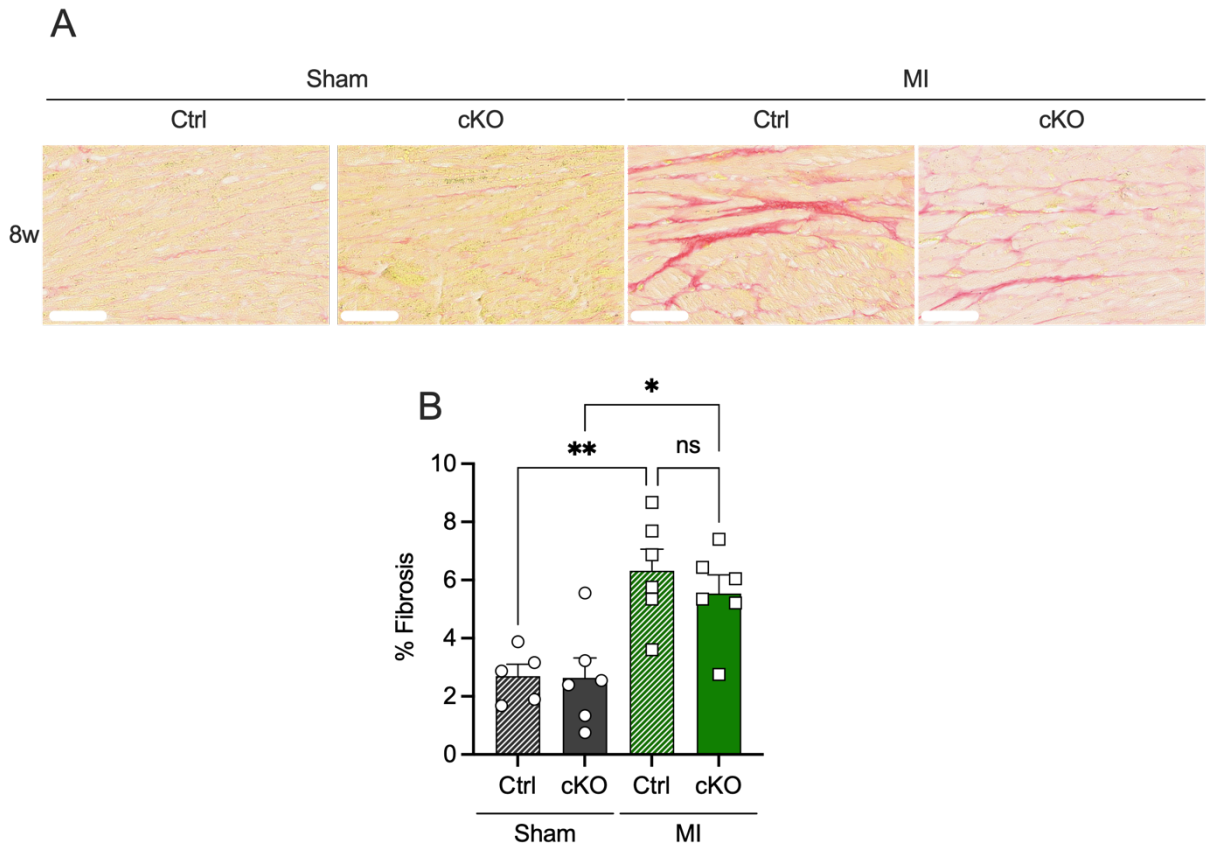


Figure 21: Interstitial fibrosis in cross-sections of PDE2A cKO and Ctrl mice hearts 8 weeks post MI. (A) Representative images of heart cross-sections from Ctrl and PDE2A cKO mice 8 weeks post MI/Sham surgery stained with Picrosirius Red (PSR). Scale bar = 50 µM. **(B)** Quantification of the amount of collagen fibers in relation to the total tissue area (% Fibrosis). Three image sections per mouse were taken with a 40x magnification in the left ventricle. Data is shown in bar graphs (mean ± SEM). *p<0.05, **p<0.005, ns–not significant by one-way ANOVA followed by Sidak's multiple comparison test.

6.2.4 T cell infiltration into the infarcted myocardium

The immune cell infiltration into the myocardium during the inflammatory process after MI, 3 days (d3) and 7 days post MI (d7), was visualized by Immunohistochemistry (IHC). CD4+ and FoxP3+ T cells were labeled with DAB and the number of FoxP3+ cells per heart section was quantified manually in PDE2A cKO and their respective littermates (Ctrl) (n=3 per group). The results and representative images of the IHC staining are depicted in **Figure 22**. Mice of both genotypes showed an accumulation of CD4+ cells in the injured myocardium and the number of FoxP3+ positive cells increased during the inflammatory response. The comparison between Ctrl and PDE2A cKO mice revealed no differences in the total number of FoxP3-positive cells (ns, $p>0.9999$).

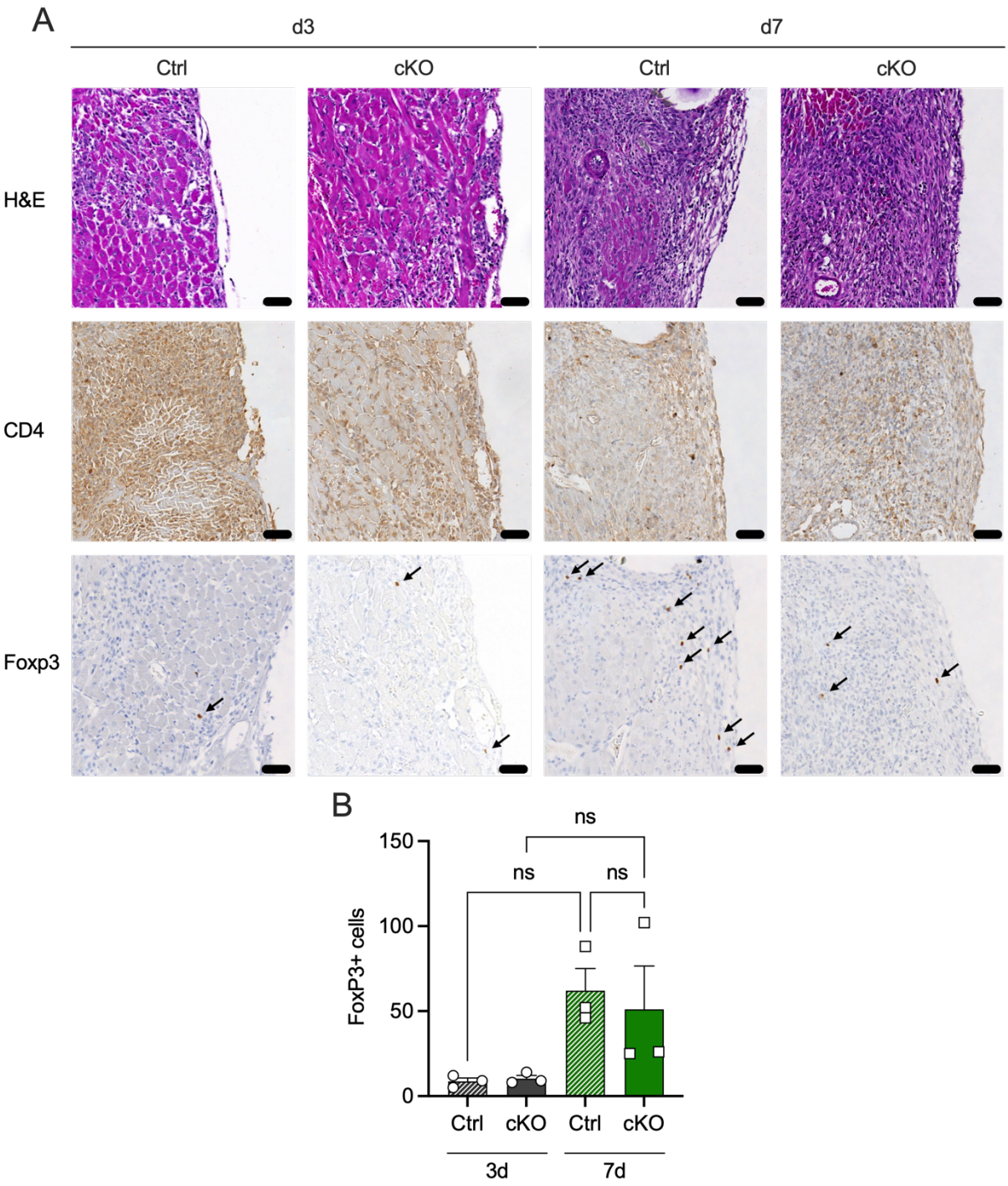


Figure 22: CD4+ T cell infiltration into the myocardium of Ctrl and PDE2A cKO mice on day 3 and day 7 post MI. (A) Representative images of H&E staining, CD4 and FoxP3 positive areas in the cross-sections from the myocardium. Ctrl (cre+) and PDE2A cKO mice were analyzed on day 3 (d3) and day 7 (d7) post MI. Scale bar = 50 µM. **(B)** Quantification of FoxP3+ T cells per heart cross-section from Ctrl and PDE2A cKO mice on d3 and d7 post MI surgery. N = 3 mice per group. Data is shown in bar graphs (mean ± SEM). ns–not significant by one-way ANOVA followed by Kruskal-Wallis test.

6.2.5 medLN tissue

The expression of the tyrosine hydroxylase (TH), the crucial enzyme for catecholamine synthesis and the expression of phosphorylated PKA substrates were determined in acute phase post MI via immunoblotting in medLN tissue isolated from PDE2A cKO and Ctrl mice on d3 post MI/Sham surgery (**Figure 23**). The analysis revealed no significant alterations between Ctrl and PDE2A cKO in Sham and MI conditions ($p>0.9999$).

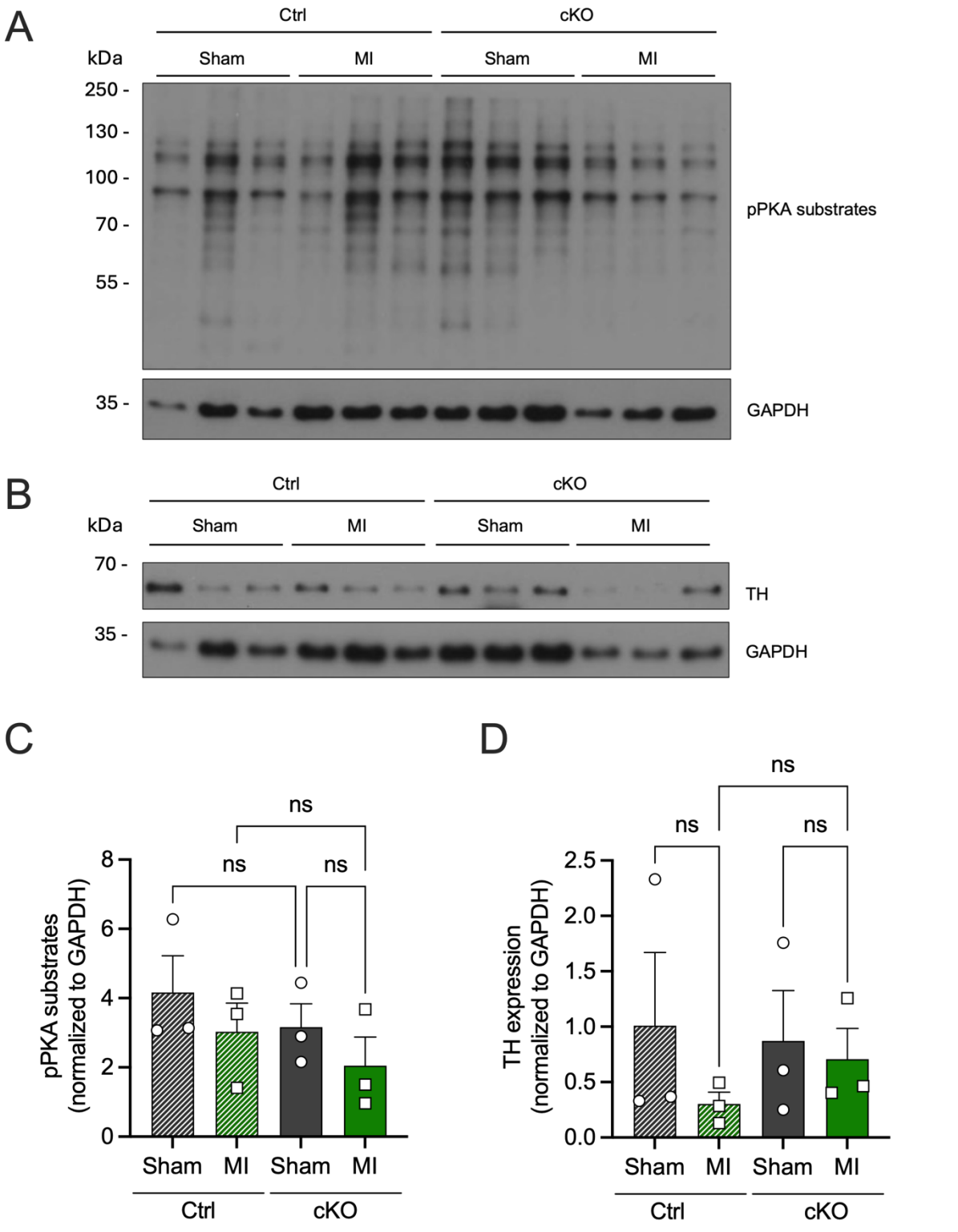


Figure 23: pPKA substrates and Tyrosine Hydroxylase (TH) expression in mediastinal lymph nodes (medLN) from Ctrl and PDE2A cKO mice on day 3 post MI/Sham surgery. (**A,C**) Expression of pPKA substrates normalized to the housekeeping protein GAPDH. (**B,D**) Expression of TH normalized to the housekeeping protein GAPDH. N = 3 mice per group. Data is shown in bar graphs (mean ± SEM). ns – not-significant by one-way ANOVA followed by Kruskal-Wallis test.

In the next step, the expression of PDE2A, PDE3B and PDE4D were analyzed in medLN tissue on d3 via immunoblotting (**Figure 24**). The quantification of the PDE expression showed comparable levels of all three analyzed PDE.

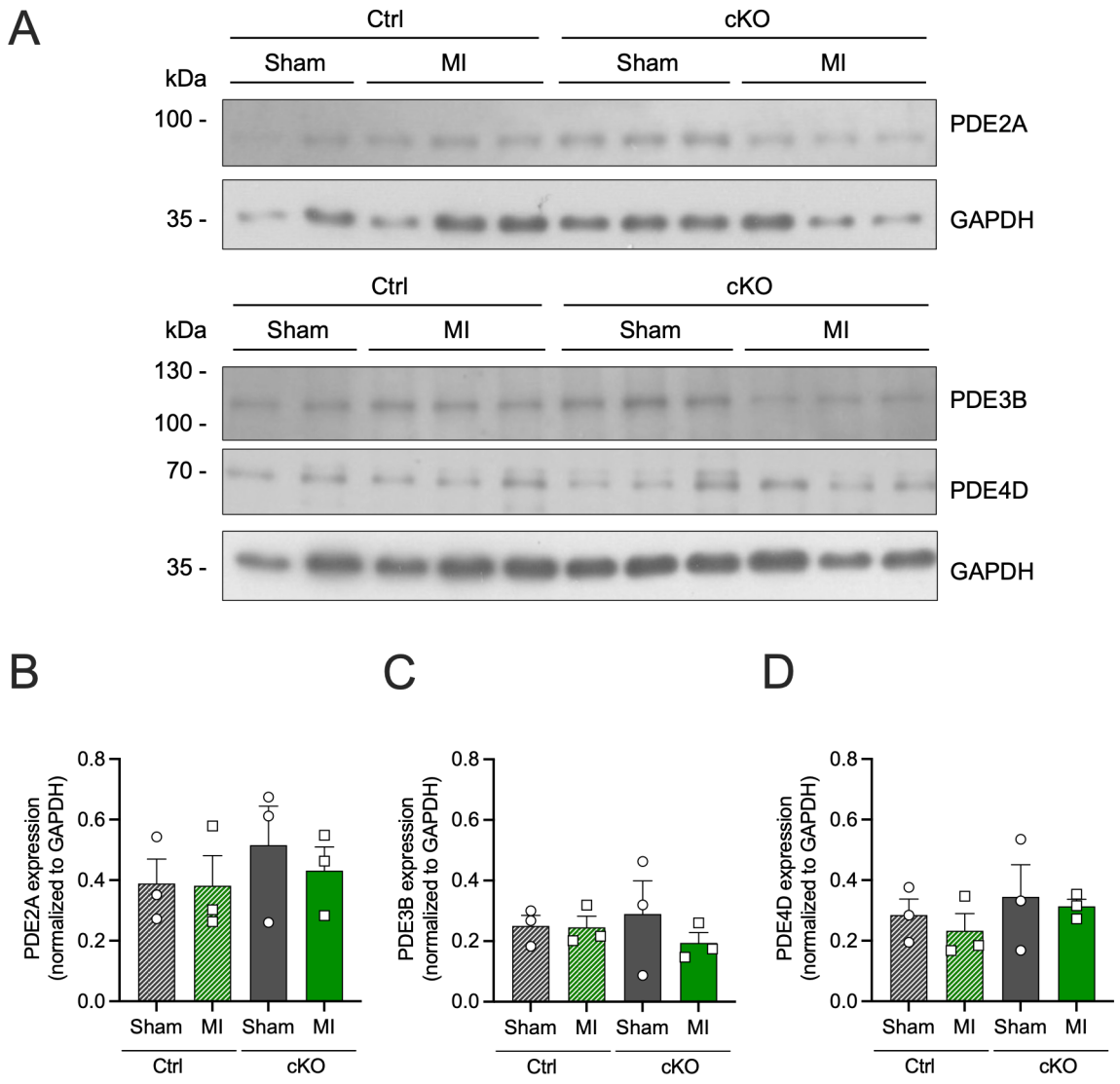


Figure 24: PDE expression in mediastinal lymph node (medLN) tissue from Ctrl and PDE2A cKO mice on day 3 post MI/Sham surgery. (**A**) Immunoblot detection of PDE2A, PDE3B, PDE4D and the housekeeping protein GAPDH. (**B**-**D**) Quantification of PDE2A (**B**), PDE3B (**C**) and PDE4D (**D**) protein expression. N = 3 mice per group. Data is shown in bar graphs (mean ± SEM). ns – not-significant by one-way ANOVA followed by Kruskal-Wallis test or Sidak's multiple comparison test.

6.2.6 Cytokine release

To assess whether the loss of PDE2A in T cells affected cytokine release after MI, the IFN-γ production was determined by ELISA (**Figure 25**). Splenic CD4+ T cells were

MACS-isolated on day 7 after MI or Sham surgery. After a 24 h overnight culture with anti-CD3/CD28 stimulation, the secretion of IFN-γ was measured in cell culture supernatants by ELISA (**Figure 25**). The preliminary analysis of IFN-γ secretion revealed comparable IFN-γ release in PDE2A cKO and Ctrl T cells (p=0.4987).

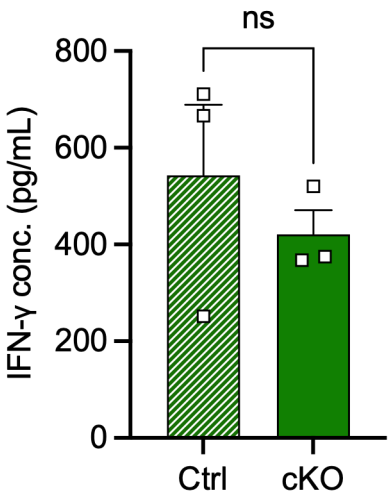


Figure 25: IFN-γ secretion T cells isolated from PDE2A cKO and Ctrl mice on day 7 post MI. MACS-sorted CD4+ T cells were cultured for 24h with *in vitro* activation via Anti-CD3/CD28 stimulation. The concentration of secreted IFN-γ was measured in cell culture supernatants. Data is shown in bar graphs as mean ± SEM. N=3 mice per group. ns – not significant by Student´s t test.

6.2.7 PDE expression in T cells

The PDE2A cKO mouse model was analyzed for the first time under pathological conditions. Thus, it was of interest to validate the KO during the disease progression and further to analyze the expression of the other most abundant PDE in T cells. For this purpose, CD4+ T cells were isolated from spleen at three distinct time points after MI/Sham surgery and cultured for 24 h with and without *in vitro* activation via anti-CD3/CD28 stimulation. The expression of PDE2A, PDE3B, PDE4B/D were quantified via immunoblotting (**Figure 26-26**).

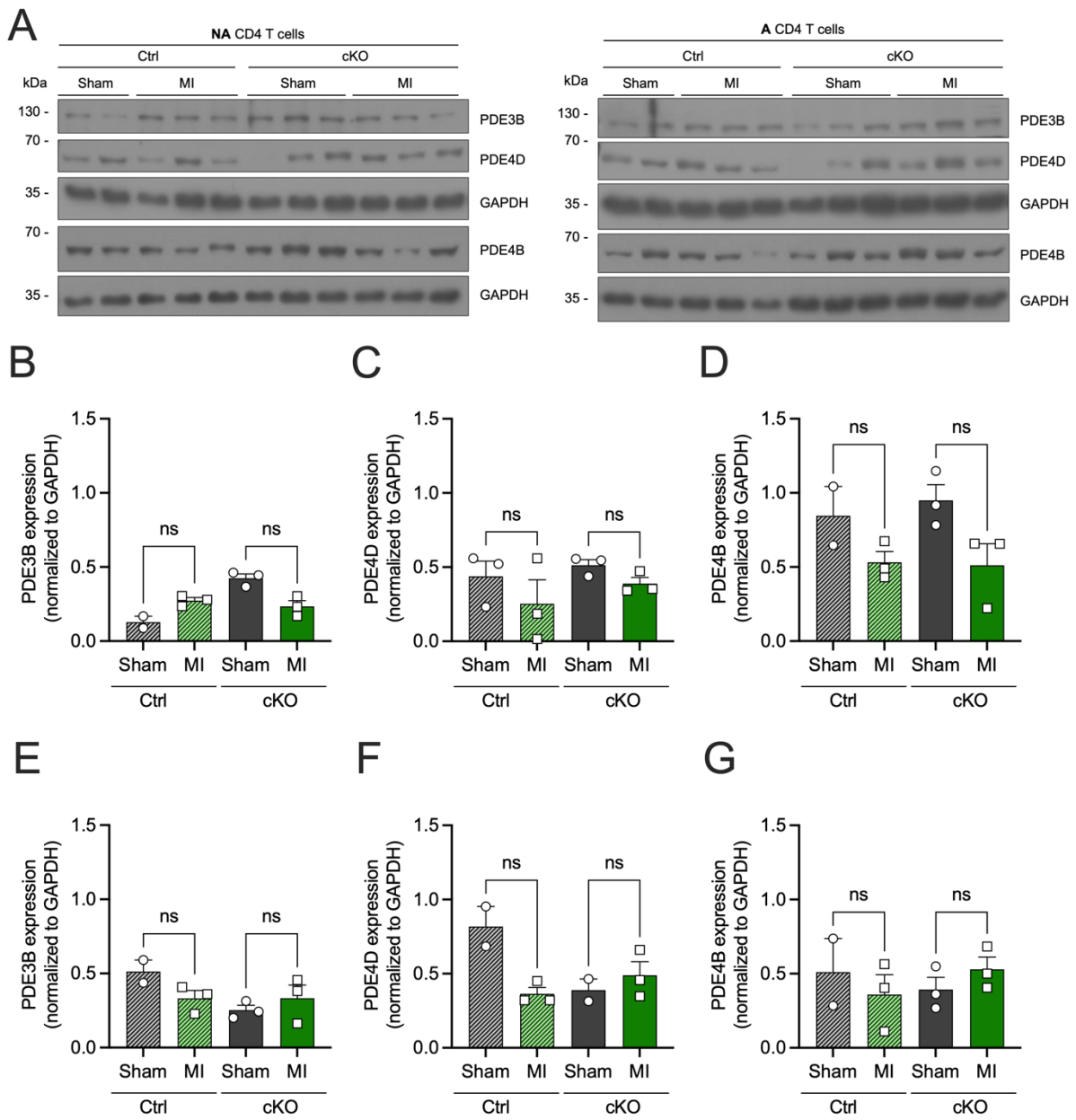


Figure 26: PDE3B, PDE4B/D expression in Ctrl and PDE2A cKO CD4+ T cells on d3 post MI/Sham surgery. Immunoblot analysis of PDE3B, PDE4B and PDE4D expression in non-activated and *in vitro* activated CD4+ T cells isolated from the spleen 8 weeks post MI. (**B**-**D**) Quantification of PDE3B, PDE4B and PDE4D expression in non-activated CD4 T cells. (**E**-**G**) Quantification of PDE3B, PDE4B and PDE4D expression in *in vitro* activated CD4+ T cells. Data shown in bar graphs as mean ± SEM. ns–not significant by one-way ANOVA followed by Sidak's multiple comparison test or Kruskal-Wallis test. N = 2-3 mice per group.

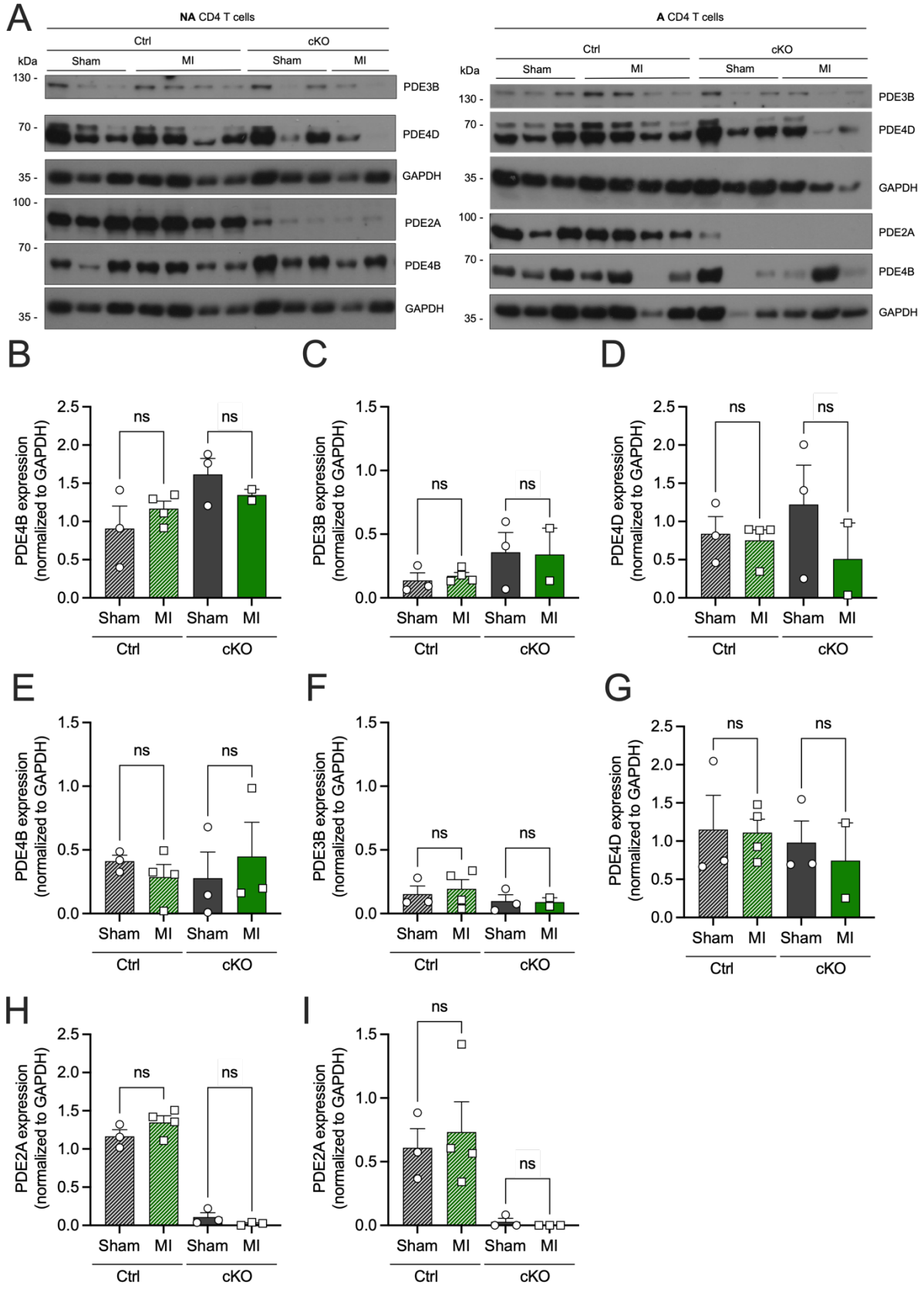


Figure 27: PDE3 and PDE4 expression in T cells on day 7 post MI. (A) Immunoblot analysis of PDE3B, PDE4B and PDE4D expression in non-activated and *in vitro* activated CD4+ T cells isolated from the spleen 8 weeks post MI. (**B-D**) Quantification

of PDE3B, PDE4B and PDE4D expression in non-activated CD4 T cells. (**E**-**G**) Quantification of PDE3B, PDE4B and PDE4D expression in *in vitro* activated CD4+ T cells. (**H**-**I**) Quantification of PDE2A expression in non-activated and activated T cells. Data is shown in bar graphs as mean ± SEM. ns–not significant by one-way ANOVA followed by Sidak's multiple comparison test or Kruskal-Wallis test. N = 2-3 mice per group.

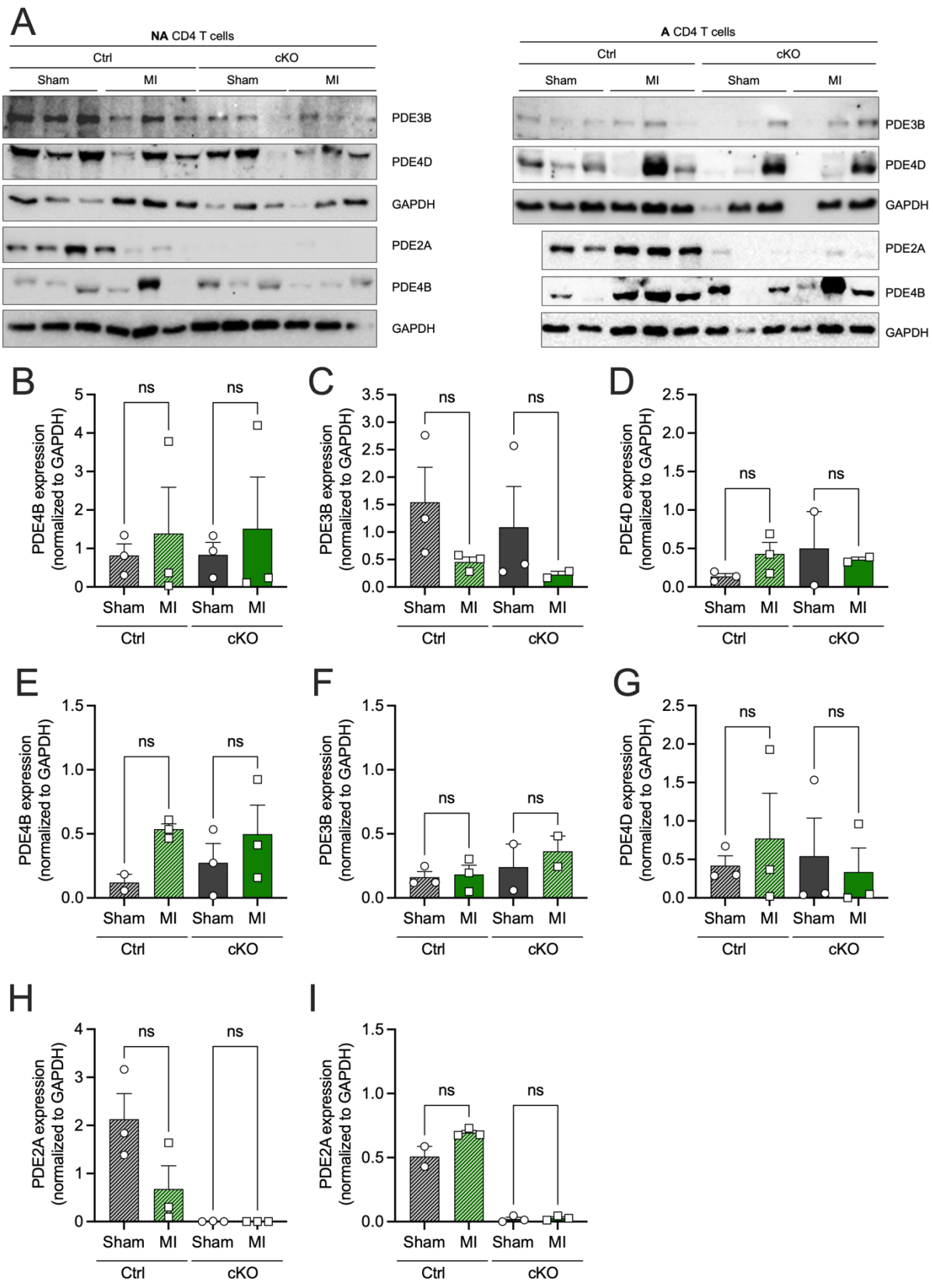


Figure 28: PDE2A, PDE3 and PDE4 expression 8 weeks post MI. (A) Immunoblot analysis of PDE3B, PDE4B and PDE4D expression in non-activated and *in vitro* activated CD4 T cells isolated from the spleen 8 weeks post MI. (**B**-**D**) Quantification of PDE3B, PDE4B and PDE4D expression in non-activated CD4 T cells. (**E**-**G**) Quantification of PDE3B, PDE4B and PDE4D expression in *in vitro* activated CD4

T cells. (**H-I**) Quantification of PDE2A expression in non-activated and activated T cells. Data is shown in bar graphs as mean +- SEM. ns–not significant by one-way ANOVA followed by Sidak's multiple comparison test or Kruskal-Wallis test. N = 2-3 mice per group.

Figure 24-26 depicts PDE2A, PDE3B and PDE4B/D expression in non-activated and *in vitro* activated T cells isolated from Ctrl and PDE2A cKO mice on day 3 (**Figure 26**), day 7 (**Figure 27**) and 8 weeks (**Figure 28**) post MI/Sham surgery. The quantification in comparison to the housekeeping gene GAPDH revealed no significant alterations between Sham and MI nor due to the loss of PDE2A in T cells at any investigated time point.

6.2.8 Summary

The second aim of this thesis was to investigate whether PDE2A modulates the T cell response after MI and thereby influences the cardiac healing process. A PDE2A cKO mouse line and their respective control littermates (expressing cre) were subject in a MI mouse model over a time course of 8 weeks. The PDE2A cKO in CD4+ T cells was verified by immunobloting and the PDE3 and PDE4 expression was comparable during time of disease progression. Echocardiography measurements monitored the cardiac function and revealed a more pronounced impairment in cardiac function. Notably, only cKO MI mice showed an increase in the LVIDd and an increase in lung weight, whereas the heart weight increased equally in both MI groups. Histological analysis of the heart involved the analysis of cardiomyocyte size by WGA staining, the content of fibrosis by PSR staining and the staining of infiltrating CD4 T cells and Treg. In summary, no differences were observed between the PDE2A cKO and Ctrl group in any histological analysis. Lastly, the IFN-γ secretion, a crucial cytokine released after MI, was unaffected by the loss of PDE2A in T cells.

7 Discussion

The central aim of this PhD study was to investigate the role of cAMP signaling in the regulation of T cell function after MI including the induction of the pathway via β-AR and $A_{2A}R$ signaling but also the PDE-mediated cAMP degradation. This signaling pathway plays a pivotal role in cardiac physiology and in immunity. However, the characterization of cAMP signaling in T cells after MI has not yet been explored. With the use of a FRET live-cell imaging approach and an *in vivo* study with PDE2A cKO mice this study provides a first comprehensive picture of T cell cAMP signaling in the context of a CVD.

7.1 β-AR desensitize in local T cells early after MI

MI characteristically activates the sympathetic nervous system that releases high levels of catecholamines to increase contractility and desensitization of the β-AR in the heart due to the sympathetic overdrive which is a well characterized phenomenon (Bristow et al. 1982). The receptor gets phosphorylated by β-adrenergic receptor kinase (GRK2) and is thus unable to induce the AC-mediated increase cAMP (Ungerer et al. 1993). Real-time FRET measurements in cAMPFIRE-M biosensor mice confirmed that β-AR of freshly isolated cardiomyocytes on d7 post MI were less responsive to β-AR stimulation by ISO treatment but compensated this 8w post MI. For the first time, the analysis of β-AR on the surface of T cells from the heart-draining medLN revealed a similar desensitization mechanism like cardiomyocytes. Non-activated T cells, which were cultured over-night with a low dose of IL-2 reacted significantly less to a low concentration of ISO on d7 post MI and likely on d3 post MI, but without significant impact. In contrast, the MACS-sorted T cells from 8w showed a comparable ISO response in Sham and MI operated mice indicating that T cells also adapted to the increased catecholamine levels. Possible mechanism would be the upregulation of the β-AR density on the cell surface. In healthy conditions, murine T cells express only β_2-AR, but it is possible that due to the adaptation β_1-AR are upregulated since ISO treatment activates all β-AR. A change in the β_1:β_2-AR ratio is a common observation in cardiomyocytes during HF development (Bristow et al. 1986). Exhausted CD8 T cells that are exposed to chronic high levels of catecholamines show an upregulation of the β_1-AR although predominantly expressing the β_2-AR in healthy

conditions (Globig et al. 2023). To test this hypothesis, ISO-mediated cAMP increase in T cells from MI and Sham mice should be determined next in the presence of β_1-AR (CGP-20712) or β_2-AR (ICI-118551) inhibitor.

Surprisingly, T cells which were re-activated with artificial anti-CD3/-CD28 antibodies *in vitro* showed the desensitization already on d3 but not on d7 post MI. As described in 3.3, TCR stimulation induces AC-mediated cAMP production which then acts in a negative feedback loop on the TCR activation (Wehbi and Taskén 2016). Moreover, T cell activation also leads to the increased expression of TH, an indication of an increase of T cell derived catecholamine synthesis for a self-amplifying autocrine loop (Cosentino et al. 2007). Possibly this results in a stronger desensitization on d3 in activated T cells than non-activated T cells.

Notably, previous research focused mainly on local T cells residing either in the heart (TCR-M specific T cells) or rely in T cells from medLN, since the latter are recruited to the heart (Delgobo et al. 2023). In 2024, Gladow et al. were the first to describe the importance of systemic T cells in splenic myelopoiesis (Gladow et al. 2024). Thus, it was of interest to compare the receptor-sensitivity between CD4+ T cells located in the medLN and T cells in the spleen. The analysis revealed that T cells from the spleen reacted comparable to β-AR stimulation over the time course of 8 weeks indicating that this T cell pool were unaffected by MI. It is likely, that the sympathetic overdrive is not present or largely reduced present in the spleen due to a different innervation of the lymphatic organs and the spleen itself. T cells in the spleen might not get exposed to high levels of catecholamines and thus do not respond with desensitization. Differences between lymphatic and splenic β-AR has not yet been described for CVD diseases, but for another inflammatory pathophysiological syndrome, the adjuvant arthritis. The disease is also driven catecholamines, mainly norepinephrine, with elevated levels in the LN in comparison with the spleen. Moreover, differences were observed in lymphatic and splenic β-AR sensitivity as adaptation to the disease progression. Treatment with the beta-blocker terbutaline resulted in increased IFN-γ production in LN, but not in the spleen (Lorton et al. 2013).

Inflammation itself is connected to the release of ATP that is degraded via CD39/CD73 to ADO, the ligand of the $A_{2A}R$. ADO levels are increased also post MI and the CD73

deficiency impaired the immunosuppressive capacity of Treg, thereby worsening the cardiac healing (Zhuang et al. 2022). It was therefore of interest to analyze if the high levels of the pro-inflammatory ADO also led to alterations in $A_{2A}R$ sensitivity in the local T cells after MI. Given the fact that ADO is degraded rapidly and acts in the local inflammation site but rather not in a systemic setting only T cells from the medLN were analyzed by FRET live-cell imaging. Unlike the β-AR, the A_{2A}-triggered cAMP increase was not altered in mice that underwent MI surgery indicating similar $A_{2A}R$ sensitivity.

The study of the impact of catecholamines in the immune cell influx post MI adds to other recent publications. For example, β-AR signaling appears to be a central driver for neutrophil infiltration. Short-term blockade by beta-blockers butoxamine and propranolol reduced neutrophil influx and improved the cardiac function (Dahdah et al. 2026). Further evidence for catecholamines influencing inflammation is the changes in macrophage subsets thereby influence the cardiac healing (Lyu et al. 2020). However, this work was the first description showing β-AR signaling in T cells post MI. Taken together, these observations demonstrate that β-AR sensitivity is altered in T cells to adapt to the post MI environment, a mechanism that seems to be conserved across different cell types. The complexity of this regulation varying across disease stages and organs point towards an involvement of β-AR and downstream cAMP signaling in the regulation of T cell responses post MI.

7.2 PDE4 and PDE8 are differentially active during disease development

After investigating the receptors that initiate cAMP production, the attention was turned to the cAMP degradation mediated by PDE. With the indirect measurement of each PDE activity by determining the cAMP increase upon PDE inhibition, two members of the family, PDE4 and PDE8, were found to be differentially active during the disease development.

PDE4 is the most abundant PDE in T cells and well characterized by research conducted over decades. To investigate a potential role of PDE4 in T cells after MI, the impact of PDE4 inhibition by ROLI on intracellular cAMP was determined in murine T cells isolated from cAMPFIRE-M mice after MI. The FRET response to ROLI in both

T cell pools, splenic and lymphatic, was increased during the chronic HF development (8w post MI) but comparable in the acute inflammatory and resolution phase. Interestingly, global PDE4 expression is not upregulated in T cells from Ctrl mice 8 weeks post MI pointing out the highly complex cAMP regulation via compartmentalization. While T cells in the first days are required for wound healing, T cells in the chronic ischemic heart are drivers of adverse remodeling and cardiac defects (Bansal et al. 2017). Pharmacological inhibition of PDE4 has anti-inflammatory effects in different autoimmune settings. Combined with the well characterized role of PDE4 function in T cells, the results indicate that PDE4 might be a potential target to prevent adverse remodeling in the ischemic HF phase. For the treatment of atopic dermatitis, the inhibition of PDE4 is mediated by a topical treatment with Crisaborole, other approved PDE4 inhibitors are taken orally and often cause gastrointestinal side effects like emesis and nausea, which would be of clinical relevance in HF patients (Li, Zuo, and Tang 2018).

Among PDE4 that appears to be predominantly active during the ischemic HF development, a temporally distinct pattern was observed for PDE8. PDE8 activity was increased during the early disease progression, the starting point of the T cell infiltration into the myocardium. In FRET measurements, the inhibition of PDE with the global PDE8 inhibitor PF-04957325 revealed a higher response, indicating higher activity of PDE8, in primary T cells from medLN and spleen after MI. PDE8 harbors the highest affinity to cAMP within the PDE family (K_m 0.15 µM) and most likely be the most efficient PDE when basal cAMP change rapidly (Bender and Beavo 2006). Moreover, PDE8 inhibition was previously linked to the control of T cell adhesion and motility previously. The PDE8 inhibition by PF-04957325 decreased adhesion of Tcon by reducing the expression of adhesion molecules and chemokine release (Basole et al. 2017). Thus, the therapeutic potential to treat inflammation by PDE8 inhibition was investigated in different diseases previously e.g. allergenic airway disease (AAD) model or the MS mouse model, EAE. In particular, the PF-04957325 treatment reduced the inflammatory cell influx and improved the outcome in EAE mice (Basole et al. 2022). Translated to the situation of MI, an increased PDE8 activity on d3 might rather be beneficial for the outcome, because T cells are required for the wound healing in the resolution phase and pharmacological inhibition early post MI resulting in less infiltrating T cells would be rather harmful. It is of important note that the adhesion of

Treg was unaffected by PF-04957325 mediated PDE8 inhibition in that study possibly because PDE8 is less expressed in this T cell subset. Therefore, it would be interesting to test if PDE8 activity is increased in all CD4+ T cells or exclusively in Tcon and further if a PDE8 inhibition would alter the T cell subset ratio between T_H1 and Treg in the infarcted heart. The heterogeneity of CD4+ T cells is the biggest limitation of this work. Beyond elucidating the therapeutic potential of PDE8 and PDE4, it would be necessary to distinguish T cell subset differences also for PDE that are differentially expressed in T cell subsets like PDE3B and PDE2A. Briefly, PDE3B expression is suppressed in Treg and PDE2A expression is upregulated only in Tcon upon TCR stimulation (Gavin et al. 2007; Kurelic et al. 2021). Inhibition of both PDE in FRET measurements revealed no differences between Sham and MI mice. It is possible that effects are influenced by measuring different T cell subsets together. In addition, Treg harbor more cAMP to fulfill their immunosuppressive function pointing out central differences in the cAMP signaling that should be considered in the future.

7.3 Elucidating the role of PDE2A as a regulator of the cAMP-to-cGMP cross-talk in T cell responses post MI

In HF hearts, PDE2 is upregulated to counterbalance β-AR stimulation thereby protecting the heart against hypertrophy due to the high levels of catecholamines (Mehel et al. 2013). PDE2A is an important regulator of the cyclic nucleotide cross-talk. Briefly, more cAMP is hydrolyzed by PDE2A when cGMP is bound to its GAF-B domain. In the context of MI, high levels of natriuretic peptides, ANP and BNP, are released post MI which trigger the cGMP production. Thus, the second aim of this work was to understand if PDE2A is involved in regulating T cell responses post MI. In T cells, PDE2A was initially described 1996 and 25 years later the importance of PDE2A-mediated cyclic nucleotide cross-talk was determined (Michie et al. 1996; Kurelic et al. 2021). The authors showed that PDE2A expression was higher in activated Tcon in comparison to non-activated Tcon, but not in activated Treg. Combining this recent publication with the fact that both cyclic nucleotide pathways are activated in the post-myocardial environment, it was of interest to study the impact of PDE2A in T cells after MI. For this purpose, a CD4+ specific PDE2A KO was generated and subjected to MI surgery. Importantly, this newly generated mouse line showed a stable Knock-Out of PDE2A upon disease progression and no compensatory mechanism by increased PDE3 or PDE4 expression. Immunohistochemistry analysis of cross-sections from Ctrl

and PDE2A cKO mice revealed CD4 and FoxP3 cell infiltrating the myocardium on d3 and d7 post MI. Although the analysis quantified FoxP3 positive cells in the heart cross-sections showing increasing number of Treg from d3 to d7, this is seen as a qualitative result: T cells infiltrated the myocardium of both genetic groups after MI. For quantitative measurements, a FACS analysis for all T cell subsets in the heart should be performed in the future.

In this study, cardiac function was monitored over a time course of 8 weeks by echocardiography measurements pointing towards a more pronounced heart failure in PDE2A cKO mice. First observation was the higher lung congestion in PDE2A cKO while the infarct size and left ventricular mass was comparable. Moreover, the diastolic left ventricular diameter (LVID) was significantly increased only in PDE2A cKO mice further developing over time. The EF decreased in both genetic groups equally verifying a MI in both groups. Wall thinning is observed during HF development and thus it was of interest to determine the wall thickness of the anterior and posterior wall in echocardiography. Wall thickness of both walls was unaltered by MI, but it is noteworthy that the scar possibly influenced the result. Scar tissue is thinner than intact tissue and it cannot be excluded that parts of the walls that were measured contain scar tissue.

Following the analysis of the cardiac function, histological analysis was performed to quantify structural changes. Hypertrophy describes enlargement of cells and therefore it was of interest to quantify the cardiomyocyte size in the left ventricle by WGA staining. The results showed an increase in cell size for both MI groups and a trend towards larger cardiomyocytes in the PDE2A cKO mice but without reaching statistical significance. This supports with modest impact the observation that PDE2A cKO have a higher disease burden than the Ctrl mice.
To address the question if mice without PDE2A in CD4+ T cells have impaired interstitial fibrosis, collagen fibers within the LV were quantified with PSR staining. 8w post MI the interstitial fibrosis is increased due to MI injury but unaffected by the presence of PDE2A in CD4+ T cells. At 8 weeks post MI, the scar is mature and the myofibroblast activation and ECM remodeling have subsided (Frangogiannis 2017). Differences in the scar maturation that may have been present earlier could have resolved to this time point. Taken together, these findings cannot exclude differences

between PDE2A cKO and Ctrl mice during the scar formation but exclude altered interstitial fibrosis in the stage of a mature scar. Beyond considering the scar maturation process, the content of collagen I and collagen III determined by RT-qPCR or immunoblot should be determined in the future.

It was of interest to determine if the cardiac phenotype caused by PDE2A cKO mice is caused by differences in the exposure of T cells to catecholamines. The hypothesis was tested by quantifying the expression of pPKA substrates and TH expression in the mediastinal lymph node tissue on d3 post MI. The analysis revealed no significant changes in the TH expression, crucial enzyme in the catecholamine synthesis, nor in the content of pPKA substrates. Also, PDE2A, PDE3B and PDE4D expression was comparable in medLN tissue lysates. There is no indication of altered catecholamine release or cAMP signaling in the lymphatic tissue.

Lastly, this work does not provide a full immunological characterization of the inflammatory response. Crucial for the response are cytokines as described earlier. Among others, IFN-γ is a cytokine released by T_H1 cells and linked to splenic myelopoiesis after MI (Gladow et al. 2024). Thus, IFN-γ secretion from MACS-isolated T cells was analyzed on d7 post MI. Preliminary data with a low number of mice revealed comparable IFN-γ secretion between PDE2A cKO and Ctrl mice. In the following, determination of cytokine levels in the MI heart would answer the question if PDE2A cKO mice harbor different cytokine levels that influence cardiac healing.

Importantly, this study was performed in male and female mice equally. A recent publication pointed out that there are sex specific differences in the inflammatory response after MI. Females had more immune cells, in particular T cells, in the infarcted area and the inflammatory response is exacerbated (Taylor et al. 2025). Therefore, it is important to investigate also sex-specific alterations in PDE2A cKO mice.

In summary, the PDE2A cKO mice had more cardiac defects and with modest impact a more pronounced HF development. It was excluded that the loss of PDE2A was compensated by other PDE. However, this work does not provide a mechanism how the loss of PDE2A in T cells led to the increased disease burden. There are three open questions which would help to understand the T cell response more in detail: First, are

intracellular cAMP and cGMP levels altered in PDE2A KO T cells. Next, cAMP is required for the immunosuppressive function of T cells. Thus, it would be important to investigate the immunosuppressive capacity of the PDE2A KO Treg under healthy and diseased conditions. Last, the influx of inflammatory cells and a shift in the macrophage population was changed upon Treg depletion (Weirather et al. 2014). It would be important to quantify infiltrating immune cell subsets, including the differentiation between T cell subsets but also M_1/M_2 macrophages. Yet, it remains an open question if the observed phenotype is caused by either increased cAMP levels or impaired cross-talk between cAMP and cGMP due to the loss of PDE2A.

8 Summary and conclusion

In this work, different steps of the cAMP signaling pathway were successfully analyzed to gain deeper understanding how cAMP regulates T cell function after MI and during HF development. With transgenic mice expressing the most sensitive cAMPFIRE-M biosensor intracellular cAMP dynamics in T cells were visualized upon β-AR and $A_{2A}R$ stimulation but also in the presence of PDE-specific inhibitors at different stages post MI.

It was shown that β-AR of T cells desensitize due to the sympathetic overstimulation locally but not systemically early post MI. This overall suggests that, like in autoimmune diseases, cAMP signaling is involved in the regulation of T cell responses. Moreover, increased PDE4 and PDE8 activity was detected in the chronic and acute phase, respectively. In summary, these findings suggest a sequential activation of PDE across disease progression and potentially reflecting stage-specific regulatory roles in the wound healing and HF development.

It was further tested if the loss of PDE2A affects the cardiac healing process after experimental MI in CD4-specific PDE2A cKO mice. Several results such as increased lung weight, increased left ventricle diameter and a trend towards larger cardiomyocytes pointed towards a more pronounced HF development in PDE2A cKO mice. Nevertheless, this work could not discover a mechanism behind this observation but provided a basis of further research investigating the therapeutic potential of PDE2A, but also PDE4 and PDE8 in T cells for a better wound healing and less cardiac defects post MI.

9 References

Abrahamsen, H., G. Baillie, J. Ngai, T. Vang, K. Nika, A. Ruppelt, T. Mustelin, M. Zaccolo, M. Houslay, and K. Taskén. 2004. 'TCR- and CD28-mediated recruitment of phosphodiesterase 4 to lipid rafts potentiates TCR signaling', *J Immunol*, 173: 4847-58.

Alshoubaki, Y. K., B. Nayer, Y. Z. Lu, E. Salimova, S. N. Lau, J. L. Tan, D. Amann-Zalcenstein, P. F. Hickey, G. Del Monte-Nieto, A. Vasanthakumar, and M. M. Martino. 2024. 'Tregs delivered post-myocardial infarction adopt an injury-specific phenotype promoting cardiac repair via macrophages in mice', *Nat Commun*, 15: 6480.

Anandagoda, N., J. C. Willis, A. Hertweck, L. B. Roberts, I. Jackson, M. R. Gokmen, R. G. Jenner, J. K. Howard, and G. M. Lord. 2019. 'microRNA-142-mediated repression of phosphodiesterase 3B critically regulates peripheral immune tolerance', *J Clin Invest*, 129: 1257-71.

Arp, J., M. G. Kirchhof, M. L. Baroja, S. H. Nazarian, T. A. Chau, C. A. Strathdee, E. H. Ball, and J. Madrenas. 2003. 'Regulation of T-cell activation by phosphodiesterase 4B2 requires its dynamic redistribution during immunological synapse formation', *Mol Cell Biol*, 23: 8042-57.

Arumugham, V. B., and C. T. Baldari. 2017. 'cAMP: a multifaceted modulator of immune synapse assembly and T cell activation', *J Leukoc Biol*, 101: 1301-16.

Asseman, C., S. Mauze, M. W. Leach, R. L. Coffman, and F. Powrie. 1999. 'An essential role for interleukin 10 in the function of regulatory T cells that inhibit intestinal inflammation', *J Exp Med*, 190: 995-1004.

Baillie, G. S., G. S. Tejeda, and M. P. Kelly. 2019. 'Therapeutic targeting of 3',5'-cyclic nucleotide phosphodiesterases: inhibition and beyond', *Nat Rev Drug Discov*, 18: 770-96.

Bansal, S. S., M. A. Ismahil, M. Goel, B. Patel, T. Hamid, G. Rokosh, and S. D. Prabhu. 2017. 'Activated T Lymphocytes are Essential Drivers of Pathological Remodeling in Ischemic Heart Failure', *Circ Heart Fail*, 10: e003688.

Basole, C. P., R. K. Nguyen, K. Lamothe, P. Billis, M. Fujiwara, A. G. Vang, R. B. Clark, P. M. Epstein, and S. Brocke. 2022. 'Treatment of Experimental Autoimmune Encephalomyelitis with an Inhibitor of Phosphodiesterase-8 (PDE8)', *Cells*, 11.

Basole, C. P., R. K. Nguyen, K. Lamothe, A. Vang, R. Clark, G. S. Baillie, P. M. Epstein, and S. Brocke. 2017. 'PDE8 controls CD4(+) T cell motility through the PDE8A-Raf-1 kinase signaling complex', *Cell Signal*, 40: 62-72.

Bender, A. T., and J. A. Beavo. 2006. 'Cyclic nucleotide phosphodiesterases: molecular regulation to clinical use', *Pharmacol Rev*, 58: 488-520.

Bjørgo, E., and K. Taskén. 2006. 'Role of cAMP phosphodiesterase 4 in regulation of T-cell function', *Crit Rev Immunol*, 26: 443-51.

Boelhouwer, E., J. Davis, A. Franco-Watkins, N. Dorris, and C. Lungu. 2013. 'Comprehension of hazard communication: effects of pictograms on safety data sheets and labels', *J Safety Res*, 46: 145-55.

Bopp, T., C. Becker, M. Klein, S. Klein-Hessling, A. Palmetshofer, E. Serfling, V. Heib, M. Becker, J. Kubach, S. Schmitt, S. Stoll, H. Schild, M. S. Staege, M. Stassen, H. Jonuleit, and E. Schmitt. 2007. 'Cyclic adenosine monophosphate is a key component of regulatory T cell-mediated suppression', *J Exp Med*, 204: 1303-10.

Bosch, L., J. J. de Haan, M. Bastemeijer, J. van der Burg, E. van der Worp, M. Wesseling, M. Viola, C. Odille, H. El Azzouzi, G. Pasterkamp, J. P. G. Sluijter, K. E. Wever, and S. C. A. de Jager. 2021. 'The transverse aortic constriction heart failure animal model: a systematic review and meta-analysis', *Heart Fail Rev*, 26: 1515-24.

Bristow, M. R. 2000. 'beta-adrenergic receptor blockade in chronic heart failure', *Circulation*, 101: 558-69.

Bristow, M. R., R. Ginsburg, W. Minobe, R. S. Cubicciotti, W. S. Sageman, K. Lurie, M. E. Billingham, D. C. Harrison, and E. B. Stinson. 1982. 'Decreased catecholamine sensitivity and beta-adrenergic-receptor density in failing human hearts', *N Engl J Med*, 307: 205-11.

Bristow, M. R., R. Ginsburg, V. Umans, M. Fowler, W. Minobe, R. Rasmussen, P. Zera, R. Menlove, P. Shah, S. Jamieson, and et al. 1986. 'Beta 1- and beta 2-adrenergic-receptor subpopulations in nonfailing and failing human ventricular myocardium: coupling of both receptor subtypes to muscle contraction and selective beta 1-receptor down-regulation in heart failure', *Circ Res*, 59: 297-309.

Brooker, G., W. L. Terasaki, and M. G. Price. 1976. 'Gammaflow: a completely automated radioimmunoassay system', *Science*, 194: 270-6.

Carberry, J., G. Marquis-Gravel, E. O'Meara, and K. F. Docherty. 2024. 'Where Are We With Treatment and Prevention of Heart Failure in Patients Post-Myocardial Infarction?', *JACC Heart Fail*, 12: 1157-65.

Carlantoni, C., L. M. H. Liekfeld, S. A. Hemkemeyer, D. Schreier, C. Saygi, R. Kurelic, S. Cardarelli, J. Kalucka, C. Schulte, M. Beerens, R. K. Mailer, T. E. Schaffer, F. Naro, M. Pellegrini, V. O. Nikolaev, T. Renne, and M. Frye. 2024. 'The phosphodiesterase 2A controls lymphatic junctional maturation via cGMP-dependent notch signaling', *Dev Cell*, 59: 308-25 e11.

Carvajal Gonczi, C. M., M. Tabatabaei Shafiei, A. East, E. Martire, M. H. I. Maurice-Ventouris, and P. J. Darlington. 2017. 'Reciprocal modulation of helper Th1 and Th17 cells by the beta2-adrenergic receptor agonist drug terbutaline', *FEBS J*, 284: 3018-28.

Chen, R., J. Zou, J. Chen, X. Zhong, R. Kang, and D. Tang. 2025. 'Pattern recognition receptors: function, regulation and therapeutic potential', *Signal Transduct Target Ther*, 10: 216.

Chen, W., W. Jin, N. Hardegen, K. J. Lei, L. Li, N. Marinos, G. McGrady, and S. M. Wahl. 2003. 'Conversion of peripheral CD4+CD25- naive T cells to CD4+CD25+ regulatory T cells by TGF-beta induction of transcription factor Foxp3', *J Exp Med*, 198: 1875-86.

Chevalier, E., V. Lagente, M. Dupont, H. Fargeau, X. Palazzi, V. Richard, M. Dassaud, M. Fric, M. Coupe, C. Carre, S. Leduc, P. Bernardelli, F. Vergne, P. Berna, and C. P. Bertrand. 2012. 'Lack of involvement of type 7 phosphodiesterase in an experimental model of asthma', *Eur Respir J*, 39: 582-8.

Chi, H., M. Pepper, and P. G. Thomas. 2024. 'Principles and therapeutic applications of adaptive immunity', *Cell*, 187: 2052-78.

Conti, M., and J. Beavo. 2007. 'Biochemistry and physiology of cyclic nucleotide phosphodiesterases: essential components in cyclic nucleotide signaling', *Annu Rev Biochem*, 76: 481-511.

Cosentino, M., A. M. Fietta, M. Ferrari, E. Rasini, R. Bombelli, E. Carcano, F. Saporiti, F. Meloni, F. Marino, and S. Lecchini. 2007. 'Human CD4+CD25+ regulatory T cells selectively express tyrosine hydroxylase and contain endogenous catecholamines subserving an autocrine/paracrine inhibitory functional loop', *Blood*, 109: 632-42.

Cross, S. L., N. F. Halden, M. J. Lenardo, and W. J. Leonard. 1989. 'Functionally distinct NF-kappa B binding sites in the immunoglobulin kappa and IL-2 receptor alpha chain genes', *Science*, 244: 466-9.

Csoka, B., L. Himer, Z. Selmeczy, E. S. Vizi, P. Pacher, C. Ledent, E. A. Deitch, Z. Spolarics, Z. H. Nemeth, and G. Hasko. 2008. 'Adenosine A2A receptor activation inhibits T helper 1 and T helper 2 cell development and effector function', *FASEB J*, 22: 3491-9.

Dahdah, A., K. P. Maremanda, M. Marimuthu, K. H. Park, R. M. Jaggers, D. Chattopadhyay, W. Qiang, N. Nitin, S. Stavrakis, T. W. Dasari, V. I. Suica, R. M. Boteanu, E. Uyy, F. Antohe, D. G. Tilley, A. J. Murphy, and P. R. Nagareddy. 2026. 'beta2 adrenergic receptors orchestrate neutrophil demargination and recruitment to the ischemic heart following myocardial infarction', *Nat Commun*.

de Rooij, J., H. Rehmann, M. van Triest, R. H. Cool, A. Wittinghofer, and J. L. Bos. 2000. 'Mechanism of regulation of the Epac family of cAMP-dependent RapGEFs', *J Biol Chem*, 275: 20829-36.

Deaglio, S., K. M. Dwyer, W. Gao, D. Friedman, A. Usheva, A. Erat, J. F. Chen, K. Enjyoji, J. Linden, M. Oukka, V. K. Kuchroo, T. B. Strom, and S. C. Robson. 2007. 'Adenosine generation catalyzed by CD39 and CD73 expressed on regulatory T cells mediates immune suppression', *J Exp Med*, 204: 1257-65.

Delgobo, M., E. Weiß, D. Ashour, L. Richter, L. Popiolkowski, P. Arampatzi, V. Stangl, P. Arias-Loza, E. Mariotti-Ferrandiz, P. P. Rainer, A. E. Saliba, B. Ludewig, U. Hofmann, S. Frantz, and G. Campos Ramos. 2023. 'Myocardial Milieu Favors Local Differentiation of Regulatory T Cells', *Circ Res*, 132: 565-82.

Duan, B., R. Davis, E. L. Sadat, J. Collins, P. C. Sternweis, D. Yuan, and L. I. Jiang. 2010. 'Distinct roles of adenylyl cyclase VII in regulating the immune responses in mice', *J Immunol*, 185: 335-44.

Dutta, A., B. Zhao, and P. E. Love. 2021. 'New insights into TCR beta-selection', *Trends Immunol*, 42: 735-50.

Feng, G., S. N. Nadig, L. Bäckdahl, S. Beck, R. S. Francis, A. Schiopu, A. Whatcott, K. J. Wood, and A. Bushell. 2011. 'Functional regulatory T cells produced by inhibiting cyclic nucleotide phosphodiesterase type 3 prevent allograft rejection', *Sci Transl Med*, 3: 83ra40.

Florea, V. G., and J. N. Cohn. 2014. 'The autonomic nervous system and heart failure', *Circ Res*, 114: 1815-26.

Foissier, L., M. Lonchampt, F. Coge, and E. Canet. 1996. 'In vitro down-regulation of antigen-induced IL-5 gene expression and protein production by cAMP-specific phosphodiesterase type 4 inhibitor', *J Pharmacol Exp Ther*, 278: 1484-90.

Förster, Th. 1948. 'Zwischenmolekulare Energiewanderung und Fluoreszenz', *Annalen der Physik*, 437: 55-75.

Frangogiannis, N. G. 2017. 'The extracellular matrix in myocardial injury, repair, and remodeling', *J Clin Invest*, 127: 1600-12.

Fredholm, B. B., I. Jzerman AP, K. A. Jacobson, K. N. Klotz, and J. Linden. 2001. 'International Union of Pharmacology. XXV. Nomenclature and classification of adenosine receptors', *Pharmacol Rev*, 53: 527-52.

Gavin, Marc A., Jeffrey P. Rasmussen, Jason D. Fontenot, Valeria Vasta, Vincent C. Manganiello, Joseph A. Beavo, and Alexander Y. Rudensky. 2007. 'Foxp3-dependent programme of regulatory T-cell differentiation', *Nature*, 445: 771-75.

Gilman, A. G. 1970. 'A protein binding assay for adenosine 3':5'-cyclic monophosphate', *Proc Natl Acad Sci U S A*, 67: 305-12.

Gladow, N., C. Hollmann, J. Weirather, X. Ding, M. Burkard, S. Uehlein, R. Bharti, K. Forstner, T. Kerkau, N. Beyersdorf, S. Frantz, G. Ramos, and U. Hofmann. 2024. 'Role of CD4(+) T-cells for regulating splenic myelopoiesis and monocyte differentiation after experimental myocardial infarction', *Basic Res Cardiol*, 119: 261-75.

Glavas, N. A., C. Ostenson, J. B. Schaefer, V. Vasta, and J. A. Beavo. 2001. 'T cell activation up-regulates cyclic nucleotide phosphodiesterases 8A1 and 7A3', *Proc Natl Acad Sci U S A*, 98: 6319-24.

Global Burden of Cardiovascular, Diseases, and Collaborators Risks. 2025. 'Global, Regional, and National Burden of Cardiovascular Diseases and Risk Factors in 204 Countries and Territories, 1990-2023', *J Am Coll Cardiol*, 86: 2167-243.

Globig, A. M., S. Zhao, J. Roginsky, V. I. Maltez, J. Guiza, N. Avina-Ochoa, M. Heeg, F. Araujo Hoffmann, O. Chaudhary, J. Wang, G. Senturk, D. Chen, C. O'Connor, S. Pfaff, R. N. Germain, K. A. Schalper, B. Emu, and S. M. Kaech. 2023. 'The beta(1)-adrenergic receptor links sympathetic nerves to T cell exhaustion', *Nature*, 622: 383-92.

Godfrey, D. I., J. Kennedy, T. Suda, and A. Zlotnik. 1993. 'A developmental pathway involving four phenotypically and functionally distinct subsets of CD3-CD4-CD8-

triple-negative adult mouse thymocytes defined by CD44 and CD25 expression', *J Immunol*, 150: 4244-52.

Goedhart, Joachim, David von Stetten, Marjolaine Noirclerc-Savoye, Mickaël Lelimousin, Linda Joosen, Mark A. Hink, Laura van Weeren, Theodorus W. J. Gadella, and Antoine Royant. 2012. 'Structure-guided evolution of cyan fluorescent proteins towards a quantum yield of 93%', *Nature Communications*, 3: 751.

Goraya, T. A., and D. M. Cooper. 2005. 'Ca2+-calmodulin-dependent phosphodiesterase (PDE1): current perspectives', *Cell Signal*, 17: 789-97.

Grakoui, A., S. K. Bromley, C. Sumen, M. M. Davis, A. S. Shaw, P. M. Allen, and M. L. Dustin. 1999. 'The immunological synapse: a molecular machine controlling T cell activation', *Science*, 285: 221-7.

Guereschi, M. G., L. P. Araujo, J. T. Maricato, M. C. Takenaka, V. M. Nascimento, B. C. Vivanco, V. O. Reis, A. C. Keller, P. C. Brum, and A. S. Basso. 2013. 'Beta2-adrenergic receptor signaling in CD4+ Foxp3+ regulatory T cells enhances their suppressive function in a PKA-dependent manner', *Eur J Immunol*, 43: 1001-12.

Harding, F. A., J. G. McArthur, J. A. Gross, D. H. Raulet, and J. P. Allison. 1992. 'CD28-mediated signalling co-stimulates murine T cells and prevents induction of anergy in T-cell clones', *Nature*, 356: 607-9.

Hauser, A. S., M. M. Attwood, M. Rask-Andersen, H. B. Schioth, and D. E. Gloriam. 2017. 'Trends in GPCR drug discovery: new agents, targets and indications', *Nat Rev Drug Discov*, 16: 829-42.

Heijink, I. H., H. F. Kauffman, D. S. Postma, J. G. de Monchy, and E. Vellenga. 2003. 'Sensitivity of IL-5 production to the cAMP-dependent pathway in human T cells is reduced by exogenous IL-2 in a phosphoinositide 3-kinase-dependent way', *Eur J Immunol*, 33: 2206-15.

Hofmann, U., N. Beyersdorf, J. Weirather, A. Podolskaya, J. Bauersachs, G. Ertl, T. Kerkau, and S. Frantz. 2012. 'Activation of CD4+ T lymphocytes improves wound healing and survival after experimental myocardial infarction in mice', *Circulation*, 125: 1652-63.

Huang, B., J. Zhao, Z. Lei, S. Shen, D. Li, G. X. Shen, G. M. Zhang, and Z. H. Feng. 2009. 'miR-142-3p restricts cAMP production in CD4+CD25- T cells and CD4+CD25+ TREG cells by targeting AC9 mRNA', *EMBO Rep*, 10: 180-5.

Huang, S., S. Apasov, M. Koshiba, and M. Sitkovsky. 1997. 'Role of A2a extracellular adenosine receptor-mediated signaling in adenosine-mediated inhibition of T-cell activation and expansion', *Blood*, 90: 1600-10.

Huang, W., L. Na, P. L. Fidel, and P. Schwarzenberger. 2004. 'Requirement of interleukin-17A for systemic anti-Candida albicans host defense in mice', *J Infect Dis*, 190: 624-31.

Ikeuchi, M., H. Tsutsui, T. Shiomi, H. Matsusaka, S. Matsushima, J. Wen, T. Kubota, and A. Takeshita. 2004. 'Inhibition of TGF-beta signaling exacerbates early cardiac dysfunction but prevents late remodeling after infarction', *Cardiovasc Res*, 64: 526-35.

Ingwersen, J., B. Wingerath, J. Graf, K. Lepka, M. Hofrichter, F. Schroter, F. Wedekind, A. Bauer, J. Schrader, H. P. Hartung, T. Prozorovski, and O. Aktas. 2016. 'Dual roles of the adenosine A2a receptor in autoimmune neuroinflammation', *J Neuroinflammation*, 13: 48.

Jain, J., V. E. Valge-Archer, and A. Rao. 1992. 'Analysis of the AP-1 sites in the IL-2 promoter', *J Immunol*, 148: 1240-50.

Jelley-Gibbs, D. M., T. M. Strutt, K. K. McKinstry, and S. L. Swain. 2008. 'Influencing the fates of CD4 T cells on the path to memory: lessons from influenza', *Immunol Cell Biol*, 86: 343-52.

Jenca, D., V. Melenovsky, J. Stehlik, V. Stanek, J. Kettner, J. Kautzner, V. Adamkova, and P. Wohlfahrt. 2021. 'Heart failure after myocardial infarction: incidence and predictors', *ESC Heart Fail*, 8: 222-37.

Jimenez, J. L., C. Punzon, J. Navarro, M. A. Munoz-Fernandez, and M. Fresno. 2001. 'Phosphodiesterase 4 inhibitors prevent cytokine secretion by T lymphocytes by inhibiting nuclear factor-kappaB and nuclear factor of activated T cells activation', *J Pharmacol Exp Ther*, 299: 753-9.

Jung, M., Y. Ma, R. P. Iyer, K. Y. DeLeon-Pennell, A. Yabluchanskiy, M. R. Garrett, and M. L. Lindsey. 2017. 'IL-10 improves cardiac remodeling after myocardial infarction by stimulating M2 macrophage polarization and fibroblast activation', *Basic Res Cardiol*, 112: 33.

Kanda, N., and S. Watanabe. 2001. 'Regulatory roles of adenylate cyclase and cyclic nucleotide phosphodiesterases 1 and 4 in interleukin-13 production by activated human T cells', *Biochem Pharmacol*, 62: 495-507.

Kelly, M. P., V. O. Nikolaev, L. Gobejishvili, C. Lugnier, C. Hesslinger, P. Nickolaus, D. A. Kass, W. Pereira de Vasconcelos, R. Fischmeister, S. Brocke, P. M. Epstein, G. A. Piazza, A. B. Keeton, G. Zhou, M. Abdel-Halim, A. H. Abadi, G. S. Baillie, M. A. Giembycz, G. Bolger, G. Snyder, K. Tasken, N. E. B. Saidu, M. Schmidt, M. Zaccolo, R. T. Schermuly, H. Ke, R. H. Cote, S. Mohammadi Jouabadi, and A. J. M. Roks. 2025. 'Cyclic nucleotide phosphodiesterases as drug targets', *Pharmacol Rev*, 77: 100042.

Klein, M., and T. Bopp. 2016. 'Cyclic AMP Represents a Crucial Component of Treg Cell-Mediated Immune Regulation', *Front Immunol*, 7: 315.

Koushik, S. V., P. S. Blank, and S. S. Vogel. 2009. 'Anomalous surplus energy transfer observed with multiple FRET acceptors', *PLoS One*, 4: e8031.

Kurelic, R., P. F. Krieg, J. K. Sonner, G. Bhaiyan, G. C. Ramos, S. Frantz, M. A. Friese, and V. O. Nikolaev. 2021. 'Upregulation of Phosphodiesterase 2A Augments T Cell Activation by Changing cGMP/cAMP Cross-Talk', *Front Pharmacol*, 12: 748798.

Landells, L. J., C. M. Szilagy, N. A. Jones, K. H. Banner, J. M. Allen, A. Doherty, B. J. O'Connor, D. Spina, and C. P. Page. 2001. 'Identification and quantification of phosphodiesterase 4 subtypes in CD4 and CD8 lymphocytes from healthy and asthmatic subjects', *Br J Pharmacol*, 133: 722-9.

Lauten, Tatlock H., Safwan K. Elkhatib, Tamara Natour, Emily C. Reed, Caroline N. Jojo, and Adam J. Case. 2025. 'TH17/Treg lymphocyte balance is regulated by beta adrenergic and cAMP signaling', *Brain, Behavior, and Immunity*, 123: 1061-70.

Le Gros, G., S. Z. Ben-Sasson, R. Seder, F. D. Finkelman, and W. E. Paul. 1990. 'Generation of interleukin 4 (IL-4)-producing cells in vivo and in vitro: IL-2 and IL-4 are required for in vitro generation of IL-4-producing cells', *J Exp Med*, 172: 921-9.

Li, H., J. Zuo, and W. Tang. 2018. 'Phosphodiesterase-4 Inhibitors for the Treatment of Inflammatory Diseases', *Front Pharmacol*, 9: 1048.

Li, Linsong, Cassian Yee, and Joseph A. Beavo. 1999. 'CD3- and CD28-Dependent Induction of PDE7 Required for T Cell Activation', *Science*, 283: 848-51.

Li, Z., Y. Zhang, and B. Sun. 2011. 'Current understanding of Th2 cell differentiation and function', *Protein Cell*, 2: 604-11.

Lighvani, A. A., D. M. Frucht, D. Jankovic, H. Yamane, J. Aliberti, B. D. Hissong, B. V. Nguyen, M. Gadina, A. Sher, W. E. Paul, and J. J. O'Shea. 2001. 'T-bet is rapidly induced by interferon-gamma in lymphoid and myeloid cells', *Proc Natl Acad Sci U S A*, 98: 15137-42.

Liopeta, K., S. Boubali, L. Virgilio, G. Thyphronitis, G. Mavrothalassitis, G. Dimitracopoulos, and F. Paliogianni. 2009. 'cAMP regulates IL-10 production by normal human T lymphocytes at multiple levels: a potential role for MEF2', *Mol Immunol*, 46: 345-54.

Lorton, D., and D. L. Bellinger. 2015. 'Molecular mechanisms underlying β-adrenergic receptor-mediated cross-talk between sympathetic neurons and immune cells', *Int J Mol Sci*, 16: 5635-65.

Lorton, D., D. L. Bellinger, J. A. Schaller, E. Shewmaker, T. Osredkar, and C. Lubahn. 2013. 'Altered sympathetic-to-immune cell signaling via beta(2)-adrenergic receptors in adjuvant arthritis', *Clin Dev Immunol*, 2013: 764395.

Lyu, J., M. Wang, X. Kang, H. Xu, Z. Cao, T. Yu, K. Huang, J. Wu, X. Wei, and Q. Lei. 2020. 'Macrophage-mediated regulation of catecholamines in sympathetic neural remodeling after myocardial infarction', *Basic Res Cardiol*, 115: 56.

Ma, N., T. Wei, B. Wang, X. Jiang, L. Zhou, and R. Zhong. 2019. 'MicroRNA-142-3p inhibits IFN-γ production via targeting of RICTOR in Aspergillus fumigatus activated CD4(+) T cells', *Ann Transl Med*, 7: 649.

Martins, T. J., M. C. Mumby, and J. A. Beavo. 1982. 'Purification and characterization of a cyclic GMP-stimulated cyclic nucleotide phosphodiesterase from bovine tissues', *J Biol Chem*, 257: 1973-9.

Massengill, C. I., L. Bayless-Edwards, C. C. Ceballos, E. R. Cebul, J. Cahill, A. Bharadwaj, E. Wilson, M. Qin, M. R. Whorton, I. Baconguis, B. Ye, T. Mao, and H. Zhong. 2022. 'Sensitive genetically encoded sensors for population and subcellular imaging of cAMP in vivo', *Nat Methods*, 19: 1461-71.

Mehel, H., J. Emons, C. Vettel, K. Wittkopper, D. Seppelt, M. Dewenter, S. Lutz, S. Sossalla, L. S. Maier, P. Lechene, J. Leroy, F. Lefebvre, A. Varin, T. Eschenhagen, S. Nattel, D. Dobrev, W. H. Zimmermann, V. O. Nikolaev, G. Vandecasteele, R. Fischmeister, and A. El-Armouche. 2013. 'Phosphodiesterase-2 is up-regulated in human failing hearts and blunts beta-adrenergic responses in cardiomyocytes', *J Am Coll Cardiol*, 62: 1596-606.

Michie, A. M., M. Lobban, T. Müller, M. M. Harnett, and M. D. Houslay. 1996. 'Rapid regulation of PDE-2 and PDE-4 cyclic AMP phosphodiesterase activity following ligation of the T cell antigen receptor on thymocytes: analysis using the selective inhibitors erythro-9-(2-hydroxy-3-nonyl)-adenine (EHNA) and rolipram', *Cell Signal*, 8: 97-110.

Mullen, A. C., F. A. High, A. S. Hutchins, H. W. Lee, A. V. Villarino, D. M. Livingston, A. L. Kung, N. Cereb, T. P. Yao, S. Y. Yang, and S. L. Reiner. 2001. 'Role of T-bet in commitment of TH1 cells before IL-12-dependent selection', *Science*, 292: 1907-10.

Muthuramu, I., M. Lox, F. Jacobs, and B. De Geest. 2014. 'Permanent ligation of the left anterior descending coronary artery in mice: a model of post-myocardial infarction remodelling and heart failure', *J Vis Exp*.

Nakashima, I. F., H. Zhong, V. O. Nikolaev, C. M. Owen, S. P. Yee, L. A. Jaffe, and J. R. Egbert. 2025. 'Intercellular diffusion of cyclic nucleotides followed by gap junction closure restarts meiosis in mouse preovulatory follicles', *Proc Natl Acad Sci U S A*, 122: e2524136122.

Nueda, A., N. Garcia-Roger, T. Domenech, N. Godessart, A. Cardenas, L. F. Santamaria-Babi, and J. Beleta. 2006. 'Phosphodiesterase 7A1 is expressed in human CD4+ naive T cells at higher levels than in CD4+ memory cells and is not required during their CD3/CD28-dependent activation', *Cell Immunol*, 242: 31-8.

Peter, D., S. L. Jin, M. Conti, A. Hatzelmann, and C. Zitt. 2007. 'Differential expression and function of phosphodiesterase 4 (PDE4) subtypes in human primary CD4+ T cells: predominant role of PDE4D', *J Immunol*, 178: 4820-31.

Ponikowski, P., A. A. Voors, S. D. Anker, H. Bueno, J. G. F. Cleland, A. J. S. Coats, V. Falk, J. R. Gonzalez-Juanatey, V. P. Harjola, E. A. Jankowska, M. Jessup, C. Linde, P. Nihoyannopoulos, J. T. Parissis, B. Pieske, J. P. Riley, G. M. C. Rosano, L. M. Ruilope, F. Ruschitzka, F. H. Rutten, P. van der Meer, and E. S. C. Scientific Document Group. 2016. '2016 ESC Guidelines for the diagnosis and treatment of acute and chronic heart failure: The Task Force for the diagnosis and treatment of acute and chronic heart failure of the European Society of Cardiology (ESC)Developed with the special contribution of the Heart Failure Association (HFA) of the ESC', *Eur Heart J*, 37: 2129-200.

Prabhu, S. D., and N. G. Frangogiannis. 2016. 'The Biological Basis for Cardiac Repair After Myocardial Infarction: From Inflammation to Fibrosis', *Circ Res*, 119: 91-112.

Ramer-Quinn, D. S., R. A. Baker, and V. M. Sanders. 1997. 'Activated T helper 1 and T helper 2 cells differentially express the beta-2-adrenergic receptor: a mechanism for selective modulation of T helper 1 cell cytokine production', *J Immunol*, 159: 4857-67.

Redondo, M., J. Brea, D. I. Perez, I. Soteras, C. Val, C. Perez, J. A. Morales-Garcia, S. Alonso-Gil, N. Paul-Fernandez, R. Martin-Alvarez, M. I. Cadavid, M. I. Loza, A. Perez-Castillo, G. Mengod, N. E. Campillo, A. Martinez, and C. Gil. 2012. 'Effect of phosphodiesterase 7 (PDE7) inhibitors in experimental autoimmune encephalomyelitis mice. Discovery of a new chemically diverse family of compounds', *J Med Chem*, 55: 3274-84.

Ridker, P. M., B. M. Everett, T. Thuren, J. G. MacFadyen, W. H. Chang, C. Ballantyne, F. Fonseca, J. Nicolau, W. Koenig, S. D. Anker, J. J. P. Kastelein, J. H. Cornel, P. Pais, D. Pella, J. Genest, R. Cifkova, A. Lorenzatti, T. Forster, Z. Kobalava, L. Vida-Simiti, M. Flather, H. Shimokawa, H. Ogawa, M. Dellborg, P. R. F. Rossi, R. P. T. Troquay, P. Libby, R. J. Glynn, and Cantos Trial Group. 2017. 'Antiinflammatory Therapy with Canakinumab for Atherosclerotic Disease', *N Engl J Med*, 377: 1119-31.

Rieckmann, M., M. Delgobo, C. Gaal, L. Buchner, P. Steinau, D. Reshef, C. Gil-Cruz, E. N. T. Horst, M. Kircher, T. Reiter, K. G. Heinze, H. W. Niessen, P. A. Krijnen, A. M. van der Laan, J. J. Piek, C. Koch, H. J. Wester, C. Lapa, W. R. Bauer, B. Ludewig, N. Friedman, S. Frantz, U. Hofmann, and G. C. Ramos. 2019. 'Myocardial infarction triggers cardioprotective antigen-specific T helper cell responses', *J Clin Invest*, 129: 4922-36.

Rodriguez, G., J. A. Ross, Z. S. Nagy, and R. A. Kirken. 2013. 'Forskolin-inducible cAMP pathway negatively regulates T-cell proliferation by uncoupling the interleukin-2 receptor complex', *J Biol Chem*, 288: 7137-46.

Ruppelt, A., R. Mosenden, M. Grönholm, E. M. Aandahl, D. Tobin, C. R. Carlson, H. Abrahamsen, F. W. Herberg, O. Carpén, and K. Taskén. 2007. 'Inhibition of T cell activation by cyclic adenosine 5'-monophosphate requires lipid raft targeting of protein kinase A type I by the A-kinase anchoring protein ezrin', *J Immunol*, 179: 5159-68.

Sakaguchi, S., N. Sakaguchi, M. Asano, M. Itoh, and M. Toda. 1995. 'Immunologic self-tolerance maintained by activated T cells expressing IL-2 receptor alpha-chains (CD25). Breakdown of a single mechanism of self-tolerance causes various autoimmune diseases', *J Immunol*, 155: 1151-64.

Saxena, A., M. Dobaczewski, V. Rai, Z. Haque, W. Chen, N. Li, and N. G. Frangogiannis. 2014. 'Regulatory T cells are recruited in the infarcted mouse myocardium and may modulate fibroblast phenotype and function', *Am J Physiol Heart Circ Physiol*, 307: H1233-42.

Schwartz, R. H. 1990. 'A cell culture model for T lymphocyte clonal anergy', *Science*, 248: 1349-56.

Schwinger, R. H. G. 2021. 'Pathophysiology of heart failure', *Cardiovasc Diagn Ther*, 11: 263-76.

Sha, W. C., C. A. Nelson, R. D. Newberry, D. M. Kranz, J. H. Russell, and D. Y. Loh. 1988. 'Positive and negative selection of an antigen receptor on T cells in transgenic mice', *Nature*, 336: 73-6.

Shaw, J. P., P. J. Utz, D. B. Durand, J. J. Toole, E. A. Emmel, and G. R. Crabtree. 1988. 'Identification of a putative regulator of early T cell activation genes', *Science*, 241: 202-5.

Sutherland, E. W., and T. W. Rall. 1958. 'Fractionation and characterization of a cyclic adenine ribonucleotide formed by tissue particles', *J Biol Chem*, 232: 1077-91.

Szczypka, M. 2020. 'Role of Phosphodiesterase 7 (PDE7) in T Cell Activity. Effects of Selective PDE7 Inhibitors and Dual PDE4/7 Inhibitors on T Cell Functions', *Int J Mol Sci*, 21.

Tang, T. T., J. Yuan, Z. F. Zhu, W. C. Zhang, H. Xiao, N. Xia, X. X. Yan, S. F. Nie, J. Liu, S. F. Zhou, J. J. Li, R. Yao, M. Y. Liao, X. Tu, Y. H. Liao, and X. Cheng. 2012. 'Regulatory T cells ameliorate cardiac remodeling after myocardial infarction', *Basic Res Cardiol*, 107: 232.

Tardif, J. C., S. Kouz, D. D. Waters, O. F. Bertrand, R. Diaz, A. P. Maggioni, F. J. Pinto, R. Ibrahim, H. Gamra, G. S. Kiwan, C. Berry, J. Lopez-Sendon, P. Ostadal, W. Koenig, D. Angoulvant, J. C. Gregoire, M. A. Lavoie, M. P. Dube, D. Rhainds, M. Provencher, L. Blondeau, A. Orfanos, P. L. L'Allier, M. C. Guertin, and F. Roubille. 2019. 'Efficacy and Safety of Low-Dose Colchicine after Myocardial Infarction', *N Engl J Med*, 381: 2497-505.

Tasken, K., and A. Ruppelt. 2006. 'Negative regulation of T-cell receptor activation by the cAMP-PKA-Csk signalling pathway in T-cell lipid rafts', *Front Biosci*, 11: 2929-39.

Taylor, E. B., L. D. Mendoza, J. D. Sandifer, J. G. Morato, N. M. Aitken, K. R. O'Quinn, I. Raman, C. Zhu, R. W. Spitz, J. E. Hall, and A. J. Mouton. 2025. 'Sex differences in the chronic autoimmune response to myocardial infarction', *Clin Sci (Lond)*, 139: 627-48.

Ungerer, M., M. Bohm, J. S. Elce, E. Erdmann, and M. J. Lohse. 1993. 'Altered expression of beta-adrenergic receptor kinase and beta 1-adrenergic receptors in the failing human heart', *Circulation*, 87: 454-63.

Vang, A. G., C. Basole, H. Dong, R. K. Nguyen, W. Housley, L. Guernsey, A. J. Adami, R. S. Thrall, R. B. Clark, P. M. Epstein, and S. Brocke. 2016. 'Differential Expression and Function of PDE8 and PDE4 in Effector T cells: Implications for PDE8 as a Drug Target in Inflammation', *Front Pharmacol*, 7: 259.

Vang, A. G., S. Z. Ben-Sasson, H. Dong, B. Kream, M. P. DeNinno, M. M. Claffey, W. Housley, R. B. Clark, P. M. Epstein, and S. Brocke. 2010. 'PDE8 regulates rapid Teff cell adhesion and proliferation independent of ICER', *PLoS One*, 5: e12011.

Veldhoen, M., R. J. Hocking, C. J. Atkins, R. M. Locksley, and B. Stockinger. 2006. 'TGFbeta in the context of an inflammatory cytokine milieu supports de novo differentiation of IL-17-producing T cells', *Immunity*, 24: 179-89.

Volpe, M., M. Carnovali, and V. Mastromarino. 2016. 'The natriuretic peptides system in the pathophysiology of heart failure: from molecular basis to treatment', *Clin Sci (Lond)*, 130: 57-77.

Wang, T., J. R. Sheppard, and J. E. Foker. 1978. 'Rise and fall of cyclic AMP required for onset of lymphocyte DNA synthesis', *Science*, 201: 155-7.

Wehbi, V. L., and K. Taskén. 2016. 'Molecular Mechanisms for cAMP-Mediated Immunoregulation in T cells - Role of Anchored Protein Kinase A Signaling Units', *Front Immunol*, 7: 222.

Weirather, J., U. D. Hofmann, N. Beyersdorf, G. C. Ramos, B. Vogel, A. Frey, G. Ertl, T. Kerkau, and S. Frantz. 2014. 'Foxp3+ CD4+ T cells improve healing after myocardial infarction by modulating monocyte/macrophage differentiation', *Circ Res*, 115: 55-67.

Weiss, E., G. C. Ramos, and M. Delgobo. 2022. 'Myocardial-Treg Crosstalk: How to Tame a Wolf', *Front Immunol*, 13: 914033.

Wildin, R. S., F. Ramsdell, J. Peake, F. Faravelli, J. L. Casanova, N. Buist, E. Levy-Lahad, M. Mazzella, O. Goulet, L. Perroni, F. D. Bricarelli, G. Byrne, M. McEuen, S. Proll, M. Appleby, and M. E. Brunkow. 2001. 'X-linked neonatal diabetes mellitus, enteropathy and endocrinopathy syndrome is the human equivalent of mouse scurfy', *Nat Genet*, 27: 18-20.

Xia, N., Y. Lu, M. Gu, N. Li, M. Liu, J. Jiao, Z. Zhu, J. Li, D. Li, T. Tang, B. Lv, S. Nie, M. Zhang, M. Liao, Y. Liao, X. Yang, and X. Cheng. 2020. 'A Unique Population of Regulatory T Cells in Heart Potentiates Cardiac Protection From Myocardial Infarction', *Circulation*, 142: 1956-73.

Yan, X., A. Anzai, Y. Katsumata, T. Matsuhashi, K. Ito, J. Endo, T. Yamamoto, A. Takeshima, K. Shinmura, W. Shen, K. Fukuda, and M. Sano. 2013. 'Temporal dynamics of cardiac immune cell accumulation following acute myocardial infarction', *J Mol Cell Cardiol*, 62: 24-35.

Yang, G., K. W. McIntyre, R. M. Townsend, H. H. Shen, W. J. Pitts, J. H. Dodd, S. G. Nadler, M. McKinnon, and A. J. Watson. 2003. 'Phosphodiesterase 7A-deficient mice have functional T cells', *J Immunol*, 171: 6414-20.

Yang, Q., J. Jeremiah Bell, and A. Bhandoola. 2010. 'T-cell lineage determination', *Immunol Rev*, 238: 12-22.

Ye, P., F. H. Rodriguez, S. Kanaly, K. L. Stocking, J. Schurr, P. Schwarzenberger, P. Oliver, W. Huang, P. Zhang, J. Zhang, J. E. Shellito, G. J. Bagby, S. Nelson, K. Charrier, J. J. Peschon, and J. K. Kolls. 2001. 'Requirement of interleukin 17 receptor signaling for lung CXC chemokine and granulocyte colony-stimulating factor expression, neutrophil recruitment, and host defense', *J Exp Med*, 194: 519-27.

Zhu, J., H. Yamane, and W. E. Paul. 2010. 'Differentiation of effector CD4 T cell populations (*)', *Annu Rev Immunol*, 28: 445-89.

Zhuang, R., Q. Meng, X. Ma, S. Shi, S. Gong, J. Liu, M. Li, W. Gu, D. Li, X. Zhang, Z. Wang, X. Ge, J. Tang, F. Lin, X. Liang, L. Zheng, Z. Liu, and X. Zhou. 2022. 'CD4(+)FoxP3(+)CD73(+) regulatory T cell promotes cardiac healing post-myocardial infarction', *Theranostics*, 12: 2707-21.

10 Appendix

Table 25: Chemicals categorized to GHS.

Chemical	H	P	GHS
(-)-Isoproterenol hydrochloride	H315, H319, H335	P261, P264, P271, P280, P302+P352, P305+P351+P338	07
3-Isobutyl-1-Methylxanthine (IBMX)	H302	P313, P301+P330+P331	07
Acrylamide (Rotiphorese Gel 30)	H302+H332, H315, H317, H319, H340, H350, H361f, H372	P280, P301+P312, P302+P352, P304+P340+P312, P305+P351+P338, P308+P313	07,08
Ammonium persulfate	H272, H302, H315, H317, H319, H334, H335	P210, P280, P301 + P012 + P030, P302+P352, P305 + P351 + P338	03, 07, 08
BAY 60-7550			
Bromophenol blue sodium salt			
Calcium chloride ($CaCl_2$)	H319	P280, P305 + P351 + P338, P337+P313	07
Cilostamide			
DAPI Fluoromount G	H300, H310, H400, H410		
Ethanol	H225, H319	P210, P233, P305 + P351 + P338	02, 07
Ethylenediamine tetra acetic acid (EDTA)	H319	P280, P305+P351+P338, P337+P313	07
Forskolin	H312	P302+P352, P280, P312, P501, P363	07

Gel Loading Dye Purple (6x)			
Halt protease inhibitor cocktail, 100x	H315, H319	P280, P264, P305+P351+P338	07
HEPES			
Hydrochloric acid (HCl)	H290, H314, H335	P280, P303+P361+P353, P304+P340, P305+P351+P338, P310	05, 07
iScript cDNA synthesis Kit	H319	P280, P264, P305 + P351 + P338, P337 + P313	07
Isoflurane	H336	P261, P271, P303 + P340, P312, P403 + P233, P405, P501	07, 08
Laemmli Sample buffer	H318	P305+P351+P338, P310, P280	
Methanol	H225, H301+H311+H331, H370	P210, P233, P280, P301+P310, P303+P361+P353, P304+P340+P311	02, 06, 08
Midori Green Advance		P261, P280	
N,N,N',N'-Tetramethyl ethylenediamine (TEMED)	H225, H302, H331, H314, H318	P210, P280, P301+P312, P303+P361+P353, P304+P340+P310, P305+P351+P338	02, 05, 07
ROTI Histofix	H317, H331, H341, H350	P202, P261, P280, P302+P352, P304+P340, P308+P313	06, 08

PF-04957325	H242	P210, P234, P235, P240, P280, P370+P378, P403, P420, P501	02
Ponceau S	H315, H319, H335	P261, P305+351+338	07
Potassium hydrogen carbonate ($KHCO_3$)	H319, H335	P261, P264+P265, P271, P280, P304 + P340, P305 + P351 + P338, P319, P337+P317, P403 + P233, P405, P501	07
Recombinant IL-2	H225, H319	P280, P210, P305+P351+P338, P337+P313, P501	
RIPA lysis buffer	H319	P280, P264, P305+P351+P338	
RNeasy Plus Micro Kit	H226, H302, H314, H318, H412	P210, P264, P280, P305+P351+P338+P310	02, 05, 07
Rolipram	H302, H315, H319, H335	P261, P264, P264+P265, P270, P271, P280, P301+P317, P302+P352, P304+P340, P305+P351+P338, P319, P321, P330, P332+P317, P337+P317, P362+P364, P403+P233, P405, P501	07
Rotiporese Gel 30	H302, H315,	P201, P280,	07, 08

	H317, H319, H340, H350, H361f, H372	P301+P312, P302+P352, P305+P351+P338, P308+P313	
Sodium dodecyl sulfate (SDS)	H315, H318, H335	P261, P280, P302 +P352, P304+P340+P312, P305+P351+P338+P3 10	05, 07
Sodium hydroxide (NaOH)		P233, P280, P303+P361+P353, P305+P351+P338, P310	
SYBR Green	H315, H219, H411		
Tris-Acetate-EDTA (TAE)	H316, H319	P264, P280, P305+P351+P338	07
Triton X-100 Solution, 10 %	H318	P280, P305+P351+P338, P313	05
Trypan blue	H350, H361	P201, P280, P202	08
Trypsin/EDTA in PBS	H334	P261, P284, P304 +P340, P342+P311	08
Type F immersion liquid	H315, H412	P273, P280, P302+P352	07
β-Mercaptoethanol	H301+H331, H310, H315, H317, H318, H361fd, H373, H410	P280, P261, P272, P273, P320+P352, P333+P313	05, 06, 08, 09
Proteinase K	H334	P261, P284, P304+P340, P342+P311, P501	08
Rolipram	H302, H315, H319, H335	P261, P264+P265, P270, P271, P280, P301+P317,	07

		P302+P352, P304+P340, P305+P351+P338, P319, P321, P330, P332+P317, P337+P317, P362+P364, P403+P233, P405, P501	
Sudan Black	H341	P202, P280, P308+P313, P405, P501	08

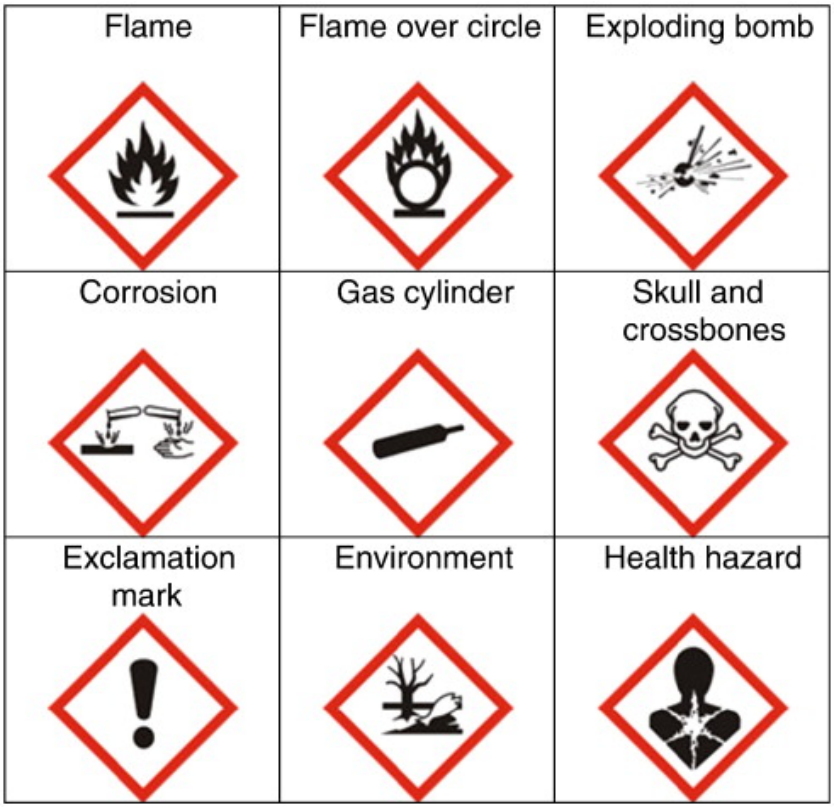


Figure 29: Hazard Pictograms according to GHS. Flame (GHS02), Flame over circle (GHS03), Exploding bomb (GHS01), Corrosion (GHS05), Gas cylinder (GHS04), Skull and crossbones (GHS06), Exclamation mark (GHS07), Environment (GHS09), Health hazard (GHS08). Image from (Boelhouwer et al. 2013).

11 Acknowledgments

I am especially grateful to Prof. Dr. Viacheslav Nikolaev for his excellent supervision, great support and helpful scientific discussion. His trust and the freedom he afforded me to develop my own ideas were invaluable in shaping this work and my growth as a researcher. I am also thankful for the opportunity to present this work at scientific conferences which broadened my perspective.

I am grateful to Prof. Dr. Stefan Frantz for the financial support received during this project.

I wish to thank the members of my thesis committee Prof. Dr. Elke Oetjen, Prof. Dr. Chris Meier and Prof. Dr. Christian Lohr for their time, expertise and careful evaluation of this work.

I would also like to express my sincere gratitude to Prof. Dr. Manuel Friese and Dr. Christine Gee for their vivid discussions and valuable input during the annual progress meetings within the IRTG1328. Their thoughtful questions contributed greatly to the development of this work.

I am grateful for the CRC1525 and consortium and the IRTG 1328 for the opportunity to expand my research network and deepen my scientific knowledge during my PhD.

I would like to thank my colleagues from the AG Nikolaev. To the lunch group, thank you for your help, advice and laughter, which made my days in the lab memorable and enjoyable.

Special thanks to Ms. Victoria Hänel for their technical assistance. I am also grateful for the scientific help from Svenja Kupsch who guided me patiently through the mouse work. Her technical expertise and reliability were the backbone of the animal work underlying this thesis. She never hesitated to step in wherever she was needed and her dedication and generosity were truly indispensable.

My gratitude is extended to Kristin Hartmann from the UKE mouse pathology core facility and Ms. Greta Boer who were of great help for the histological staining.

To Dr. Nadja Beck, Dr. Alexander Froese and Dr. Hariharan Subramanian thank you for your helping hand in the lab, your scientific input and feedback.

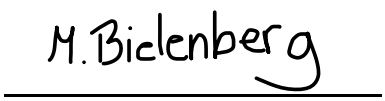
My heartfelt appreciation goes to Dr. Roberta Kurelic whose patient guidance in the early days of my PhD grew into a friendship that long outlasted our time as colleagues. The long hours at the FRET microscope with good music and well-earned pizza afterwards shaped some of my happiest memories of this PhD. Thank you for your endless support.

To my friends, near and far, thank you for reminding me that there is a world beyond the PhD and for filling it with laughter, adventures and much-needed distractions, for always looking after me and sharing all the challenging and joyful moments with me during this time.

To my family: Ohne eure unendliche Unterstützung in meiner Ausbildung und eure Geduld wäre dieser Weg unmöglich gewesen. Danke, dass ihr immer an mich geglaubt habt.

12 Affidavit

Hiermit versichere ich an Eides statt, die vorliegende Dissertationsschrift selbst verfasst und keine anderen als die angegebenen Quellen und Hilfsmittel benutzt zu haben. Sofern im Zuge der Erstellung der vorliegenden Dissertationsschrift generative Künstliche Intelligenz (gKI) basierte elektronische Hilfsmittel verwendet wurden, versichere ich, dass meine eigene Leistung im Vordergrund stand und dass eine vollständige Dokumentation aller verwendeten Hilfsmittel gemäß der Guten wissenschaftlichen Praxis vorliegt. Ich trage die Verantwortung für eventuell durch die gKI generierte fehlerhafte oder verzerrte Inhalte, fehlerhafte Referenzen, Verstöße gegen das Datenschutz- und Urheberrecht oder Plagiate.



Hamburg, den 29.06.2026